Electrical Characterization of Majority Carrier Traps in Electron Irradiated Epitaxial N-type Si

Lars Sundnes Løvlie

THESIS SUBMITTED FOR THE DEGREE OF MASTER OF SCIENCE

DEPARTMENT OF PHYSICS
UNIVERSITY OF OSLO

JULY 2007

Contents

1 Introduction **3**

2 Abstract **5**

3 Background **7**

3.1 General semiconductor theory 7
3.1.1 Crystal structure and band gap 7
3.1.2 Point defects in general 11
3.1.3 Pn-junctions 12
3.1.3.1 The principle of pn–junctions 12
3.1.3.2 The capacitance of the depletion region 13
3.1.3.3 Forward and reverse bias 15
3.1.4 Capture and emission of charge carriers 15
3.1.4.1 Charge states and deep levels 15
3.1.4.2 The rate equation 15
3.1.4.3 Capture rate 19
3.1.4.4 Emission rate 20
3.1.4.5 Activation enthalpy and apparent capture cross section . 21
3.1.4.6 Separation of capture and emission by a pn–junction . . 21
3.1.5 Reaction kinetics 22
3.1.5.1 Diffusion–limited reactions 22
3.1.5.2 1st order reactions 23
3.1.5.3 2nd order reactions and special cases 24
3.2 Radiation damage in Si 26
3.2.1 Stopping and damage production 26
3.2.2 Impurities and radiation induced point defects in silicon 28
3.3 Previous work 29
3.3.1 Type inversion of silicon radiation detectors 29
3.3.2 The importance of dose and [O_i] 30
3.3.2.1 Low dose or large [O_i] 32
3.3.2.2 High dose or small [O_i] 32
3.3.3 The influence of hydrogen on the generation and annealing of VO, V_2 and V_2O 32
3.3.3.1 Low concentration of hydrogen 33
3.3.3.2 High concentration of hydrogen 33
3.3.3.3 Interpretation 33

3.3.4 The identification of V_2O . . . 34
3.3.5 Comparison of MCz- and DOFZ-Si . . . 35

4 Experimental techniques and instrumentation 41
4.1 Sample properties, structure and irradiation . . . 41
4.2 Experimental techniques . . . 43
4.2.1 Current-voltage (IV) . . . 44
4.2.2 Capacitance-voltage (CV) . . . 44
4.2.2.1 Doping concentration and built-in voltage . . . 44
4.2.2.2 Depletion voltage and maximum junction width . . . 44
4.2.3 Deep Level Transient Spectroscopy (DLTS) . . . 46
4.2.3.1 The principle of DLTS . . . 46
4.2.3.2 Equilibrium . . . 46
4.2.3.3 Charging . . . 46
4.2.3.4 Emission . . . 48
4.2.3.5 Rectangular transient charge model . . . 49
4.2.3.6 The λ–length and the Debye tail . . . 49
4.2.3.7 Capacitance transients . . . 51
4.2.3.8 Weighting functions and rate windows . . . 53
4.2.3.9 Extraction of trap properties . . . 55
4.2.3.10 Synthesizing DLTS spectra . . . 56
4.2.4 Profiling with DLTS . . . 57
4.3 Annealing experiments . . . 57
4.3.1 Isochronal annealing . . . 58
4.3.2 Isothermal annealing experiments . . . 58
4.4 Instrumentation . . . 58
4.4.1 The Asterix setup . . . 58
4.4.2 Annealing equipment and procedures . . . 60

5 Results and discussion 61
5.1 Goals . . . 61
5.2 Impurity concentrations and distributions . . . 61
5.2.1 Expected distributions of oxygen, carbon and hydrogen . . . 61
5.2.2 SIMS measurements . . . 62
5.3 Isochronal annealing: Thermal stability . . . 63
5.3.1 Separation of overlapping peaks . . . 64
5.3.1.1 Determination of the number of overlapping levels . . . 64
5.3.1.2 Determination of the level properties . . . 66
5.3.2 Comparison to previous work on DOFZ– and MCz–Si . . . 69
5.4 Isothermal annealing: Reaction kinetics . . . 71
5.4.1 Pre–annealing: Conversion of V_2 into V_2O . . . 71
5.4.2 Isothermal annealing at 325, 338, 350 and 360 °C . . . 74
5.4.3 Known defects . . . 77
5.4.3.1 VO . . . 77
5.4.3.2 V_2 and V_2O . . . 81
5.4.3.3 VOH . . . 84
5.4.4 Modeling of reactions . . . 88

5.4.5 Unidentified levels 89
5.4.5.1 E(170 K) 89
5.4.5.2 E(198 K) 96

6 Summary **103**
6.1 Conclusions 103
6.2 Suggestions for future work 104

Appendices **105**

A Documentation of Matlab-scripts **105**
A.1 Analysis of DLTS-spectra 105
A.2 Fitting/synthesis of DLTS-spectra 107
A.3 Simulation of defect reactions 109

B Integration of the Poisson equation **112**

C Properties of some electrically active defects in electron irradiated Si **115**

References **i**

Acknowledgements

> "If that's the world's smartest man, God help us."
>
> — *The mother of Richard Feynman*

I would like to thank my advisors, Dr. Edouard Monakhov and professor Bengt Svensson, for sharing their apparently unlimited knowledge about semiconductors, impurities and defects. I also appreciate the informal way in which they supervise students. Even with their busy schedules at times, it was hardly ever necessary to make appointments. I am also very grateful for the valuable guidance from Mads Mikelsen through the first year. He provided very valuable insight on DLTS theory and measurements, and introduced me to everything in the lab.

There are many others at Minalab who deserve thanks. First and foremost, Jan Bleka showed me many "tips and tricks" of the lab–work, and also suffered through long discussions about point defects. In addition, he introduced me to a whole range of food which can be prepared in that most valued piece of equipment, the microwave oven. Also, his printer–motor lift is legendary. Lasse Vines and Dr. Jens Christensen measured the SIMS results in this thesis. Both Jan and Lasse provided much appreciated Matlab know–how, and also made me aware of the value of depth profiling. Finally, all the master students, phd students and post–docs at Minalab made the lunches very ... interesting.

Thanks to the people in Hamburg, in particular professors Ioana Pintilie and Gunnar Lindström, Dr. Eckhart Fretwurst, Frank Hönniger, Kathrin Koch and Alexandra Junkes, who made me feel very welcome and were great company. Ioana is a true inspiration, with a highly energetic way of teaching semiconductor physics resulting in countless revelations during only a months stay in Hamburg.

My family deserve thanks for many things. Most recently, my parents provided financial support with no hesitation. Anders gave me a place to stay when I needed it, for which I'm very grateful. I am also very lucky to have the worlds best girlfriend, Hanne–Torill Mevik. She showed that she has a high tolerance for my whining and feeling sorry for myself when I had problems with the thesis, and also for long monologues whenever I accomplished something. She also voluntarily (!) proof–read most of this thesis for errors both in language and mathematics.

Lars Løvlie
July 2007

Chapter 1

Introduction

There are at least two reasons for studying radation induced point defects in semiconductors. On the one hand, radiation can be used as a tool to create defects, and the defects can then be studied as fundamental research. On the other hand, radiation inevitably produces defects in devices which are in radation exposed environments. If these defects are studied and understood, then radiation resistant semiconductor materials or devices can be engineered where the effect of those specific defects are suppressed.

Ion implantation is a much used processing technique in the semiconductor industry, but the ion bombardment gives rise to crystal damage which needs to be removed in order to obtain operating semiconductor devices. Unintentional irradiation is a serious problem in space applications. Microelectronics and solar cells in satellites in the Van Allen radiation belt can be critically damaged from oxide charge or electrically active defects in silicon. A prime example, literally, is the Starfish Prime exo–atmospheric nuclear test in 1962 which created MeV electron radiation that stayed in the atmosphere for another 5 years. It eventually destroyed a third of all the low orbit satellites at the time. Some other applications in radiation–exposed environments are sensors in the vicinity of nuclear reactors, and some medical equipment.

Different variants of Si have been considered for use as radiation sensors in high energy physics experiments. The main difference between these materials is the concentration of impurities. Extensive research in the CERN RD48 collaboration revealed that the concentrations of carbon and oxygen have a large influence on the resistance to type inversion of the sensor material. The radiation hardness increases with increasing oxygen concentration, and decreases with increasing carbon concentration [9]. Diffusion oxygenated float zone (DOFZ) silicon was engineered with a large oxygen concentration and a low carbon concentration as a result of these findings. Recently, magnetic Czochralski (MCz) substrates have also been produced with very low carbon concentrations and intermediate oxygen concentrations. DOFZ and MCz materials for radiation detector applications have been studied by using electron irradiation in the last years [24,25]. Epitaxial (EPI) silicon layers with low concentrations of both oxygen and carbon grown on top of Czochralski substrates have also attracted attention because of reports indicating a large resistance to type inversion [19].

The goal of this work is to investigate wether the defect reaction mechanisms that were found to explain the defect behavior in DOFZ–Si and MCz–Si, can also explain the defect behavior in EPI–Si. An additional goal is to characterize and establish possible relationships between previously unknown defects, or between defects and impurities with a particular interest in the role of hydrogen in the annealing mechanisms.

Chapter 2

Abstract

Epitaxial p^+–n^-–n^+ silicon diodes have been irradiated with 6 MeV electrons to a dose of 10^{14} cm^{-2}, and isochronal and isothermal annealings at the temperatures 325 – 360 °C has been performed. The reaction kinetics of VO, V_2O and VOH is studied and compared to the corresponding defect behavior in diffusion oxygenated float zone (DOFZ) and magnetic Czochralski (MCz). VO and V_2O is found to mainly dissociate, in correspondance with studies in DOFZ and MCz, but a fraction of VO also anneals by production of VOH as found by depth profiling. Depth profiling also suggests that VOH subsequently disappears through the generation of VOH_2. Modeling is performed which confirms these conclusions.

The growth rate of VOH, with $c_0 = 3 \times 10^{13}$ s^{-1}, is further argued to be close to the dissociation rate of a near–surface hydrogen complex HZ because of the high diffusivity of H. Furthermore, the loss of an unidentified defect labeled E(170 K) is proportional to the growth of VOH, and the ratio approaches unity at 360 °C. E_a and c_0 is also identical for the decay of E(170 K) and the growth of VOH. Thus, the decay of E(170 K) is believed to be because of the reaction E(170 K) + Z $\rightarrow$ inactive complex, where the diffusivity of Z is large. The growth of a second unidentified defect labeled E(198 K) is proportional to the loss of V_2O, with a ratio of 0.14 ± 0.03.

Chapter 3

Background

> "The full detail of the total complexity may well be indecipherable experimentally and intractable theoretically. We will be content to consider a few general features."
>
> — *J. W. Corbett*

This chapter will provide an overview of the theory required to interpret the measurements presented in the following chapters. In short, the topics presented are some general semiconductor theory, Shockley–Read–Hall theory, specific details about radiation induced point defects in silicon and finally a summary of recent previous work on which the work in this thesis is based.

3.1 General semiconductor theory

3.1.1 Crystal structure and band gap

Silicon (Si) is a crystalline material with a diamond structure. The diamond lattice is not really a basic lattice, or a so–called Bravais lattice as described in e.g. Kittel [18, p. 16]. Instead it can be regarded as composed of two partially overlapping face centered cubic (FCC) lattices with a single Si atom at each lattice point of the two lattices. More conveniently, it can be described as a single FCC lattice with the usual FCC primitive cell, but with a basis consisting of two Si atoms at $(0, 0, 0)$ and $(\frac{1}{4}, \frac{1}{4}, \frac{1}{4})$, respectively, as shown in figure 3.1.

In a crystalline material the lattice atoms are arranged in a fixed, orderly way in 3 dimensions. Between conduction electrons and lattice atoms there will be a superposition of periodic Coloumb potentials from each lattice atom, so the superpositioned potential will have the same periodicity as the crystal structure. This periodic potential will force the conduction electrons in the crystal to assume only certain energies. More specifically

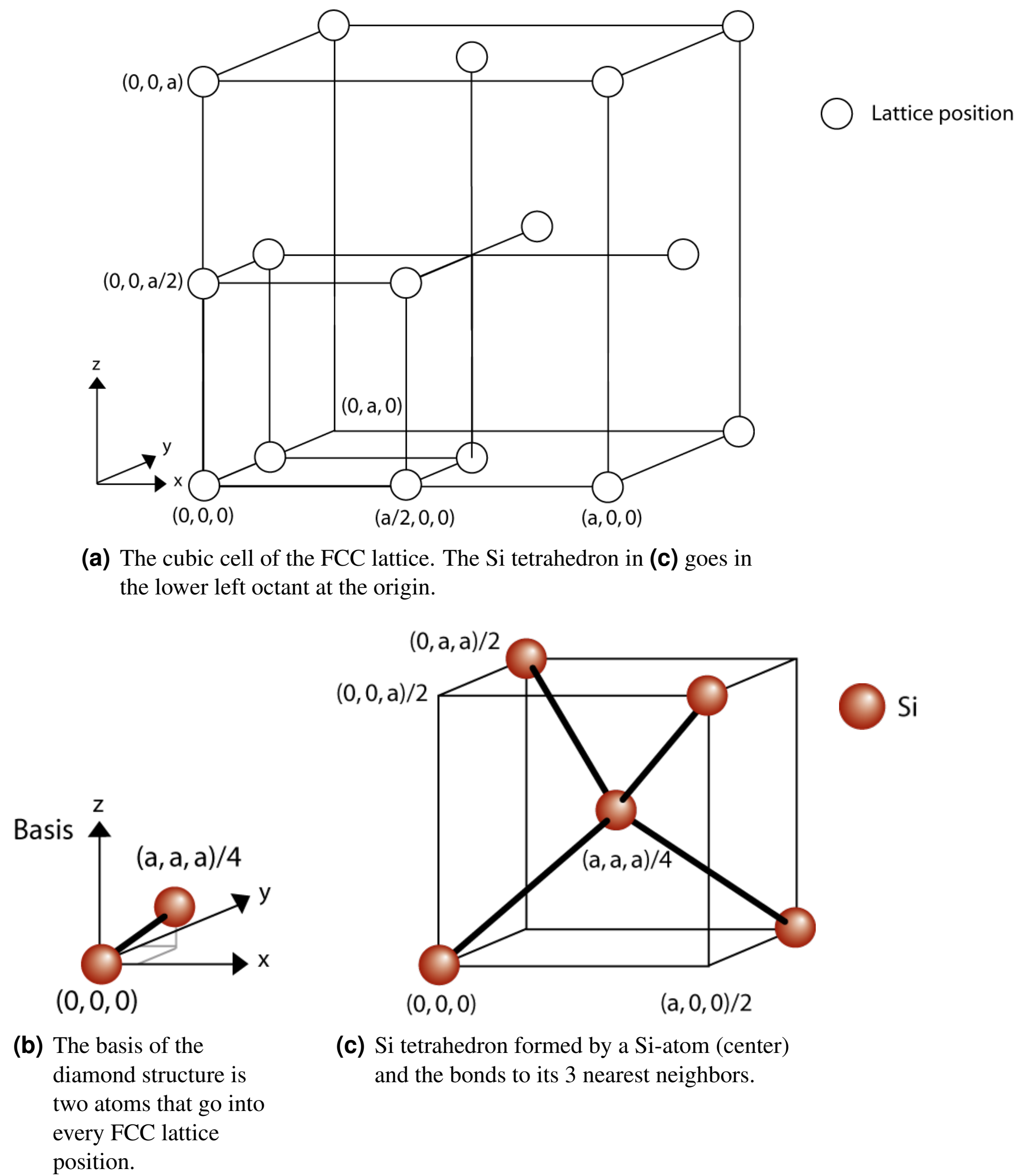

(a) The cubic cell of the FCC lattice. The Si tetrahedron in **(c)** goes in the lower left octant at the origin.

(b) The basis of the diamond structure is two atoms that go into every FCC lattice position.

(c) Si tetrahedron formed by a Si-atom (center) and the bonds to its 3 nearest neighbors.

Figure 3.1: The FCC lattice type **(a)**, the basis of Si **(b)** and the bonds between a Si atom and its 4 nearest neighbors **(c)**.

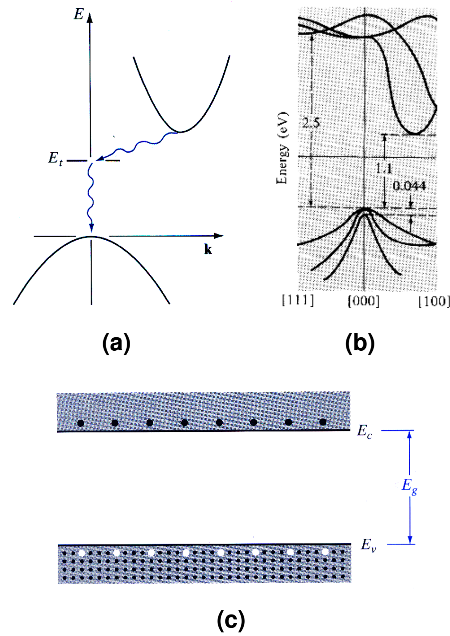

Figure 3.2: Indirect band gap, figure from Streetman [38] **(a)**. The energy bands of Si which shows that Si has an indirect band gap, from Ascroft and Mermin [3] **(b)**. Simplified visualization of the band gap and EHP's, from Streetman [38] **(c)**.

it will create an interval (or a band in a plot of energy as a function of wavenumber) of forbidden energies which is called the energy *band gap*. The so–called Kronig–Penney model is a simple and instructive approximation to this problem.

Electrons with a larger energy than the upper edge of the band gap are conduction electrons, they are free to move around in the crystal in response to an electric field. Therefore the semi-infinite interval of energies with a lower limit at the upper edge of the band gap and no upper limit is called the *conduction band*. Correspondingly, the electrons that are below the band gap in energy are called valence electrons and they are bound to electronic orbitals around the nucleus in the *valence band*. Missing valence electrons in lattice atoms are referred to as holes with an elementary charge +e. Holes act as charge carriers in the valence band in the same way as electrons are the charge carriers in the conduction band.

A valence electron can get excited from the valence band to the conduction band and leave behind a hole. These two charge carriers are then called an electron-hole-pair (EHP). The band structure of Si has been visualized in figure 3.2(b). This figure shows that Si has an indirect band gap since the conduction band minimum does not occur at the same wavenumber, $\vec{k}$, as the valence band maximum.

The charge carrier densities in the conduction and valence band are

$$
\begin{aligned}
n &= N_c f(E_c) \approx N_c e^{-(E_c - E_F)/kT} \\
p &= N_v \left(1 - f(E_v)\right) \approx N_v e^{-(E_F - E_v)/kT}
\end{aligned}
\tag{3.1}
$$

respectively, where

$$f(E) = \frac{1}{1 - e^{(E-E_F)/kT}} \approx e^{-(E-E_F)/kT} \text{ when } \exp((E-E_F)/kT) \gg 1 \quad (3.2)$$

$$N_{c,v} = 2\left(\frac{2\pi m^*_{n,p} kT}{h^2}\right)^{3/2} \quad (3.3)$$

$N_{c,v}$ is the effective density of states in the conduction and valence band. $f(E)$ is the Fermi distribution which represents the probability for having a charge carrier in the state with energy E. $E_{c,v,F}$ is the energy at the conduction band edge, valence band edge and Fermi level. The Fermi level is stricly defined as the energy of the filled state with the highest energy at $T = 0$ K in thermal physics, but the term is used also at higher temperatures in semiconductor physics. $m^*_{n,p}$ is the effective mass of electrons and holes.

For an intrinsic semiconductor $E_F = E_{F,i}$ and

$$n_i = N_c e^{-\left(E_c - E_{F,i}\right)/kT} = \sqrt{N_v N_c} e^{-E_g/kT} \quad (3.4)$$

so if $N_v = N_c$, then $E_c - E_{F,i} = E_g/2$ since $E_g = E_c - E_v$. This means that $E_{F,i}$ is in the middle of the band gap. However, as can be seen from equation (3.3), that is not entirely true since $m^*_p \neq m^*_n$. In general $E_{F,i}$ can be calculated from $n_i = p_i$ from equation (3.1) which gives

$$E_{F,i} = \frac{E_C + E_V}{2} + \frac{kT}{2} \ln\left(\frac{N_V}{N_C}\right) \quad (3.5)$$

3.1.2 Point defects in general

As mentioned above, in pure Si the electrons can not have energies within the band gap. However, any real semiconductor will have defects, such as dopants and other atoms, that have been unintentionally introduced. *Electrically active* defects introduce allowed electron energies within the band gap, where electrons or holes can get trapped, be emitted after being trapped or actually recombine. *Electrically inactive* defects have states that are outside the band gap and therefore they do not influence the transport of carriers between the bands. However, they can decrease the mobility of electrons and holes by scattering.

Defects in a crystalline material can have 0, 1, 2, or 3 dimensions depending on whether the defect upsets the short range order of the crystal structure in a point, along a line, in a plane or in a volume. This thesis deals with radiation induced point defects in Si, and these are of a size on the order of the Si atoms themselves. A point defect in a crystalline material falls into one of three categories, as explained in table 3.1. Creation and annihilation of Frenkel pairs (an interstitial and its vacancy) is visualized in a 2-dimensional crystal lattice in figure 3.3. A foreign atom in a semiconductor is also referred to as an impurity, and it can be electrically active.

Doping of a semiconductor is the creation of very shallow levels that easily donate their electrons to the conduction band or their holes to the valence band. Phosphorus and boron

Point defect type	Description
Substitutional	- An atom, silicon or foreign, which is in an actual lattice position.
Interstitial	- An atom, silicon or foreign, in some non-lattice position.
Vacancy	- An empty lattice position which is produced when a substitutional atom becomes an interstitial.
Cluster (also called extended point defect)	- A mixture of several point defects of any of the above categories.

Table 3.1: The different categories of point defects.

are two kinds of impurity species which are intentionally introduced into substitutional positions since they are used for doping the silicon n–type or p–type, respectively. In lattice positions, the P_S– and B_S–substitutionals create very shallow band gap levels that are very close to the conduction and valence band edge, respectively. The consequence of an effective concentration of dopants, $|N_{eff}| = |N_a - N_d|$, is that E_F moves towards E_c or E_v for n–type and p–type, respectively. $N_{a,d}$ is the concentration of acceptor and donor dopants.

Oxygen, carbon and hydrogen are the kind of species that are usually unintentionally introduced and they can be either in a substitutional or in an interstitial position. Whether an impurity is substitutional or interstitial can be important for the electrical activity, like mentioned above for doping atoms. As an example, C_i is electrically active with one donor and one acceptor level, whereas C_s is electrically inactive.

Point defects which are not electrically active are irrelevant from the point of view of electrical characterization, except for the fact that they can later transform into an electrically active defect through reaction with some other defect. If the concentration of electrically active defects, N_t, is much lower than that of dopants, i.e. $N_t \ll N_{eff}$, the material is said to be in the dilute limit where E_F is entirely controlled by N_d. Otherwise, if $N_t \gtrsim N_{eff}$ then the concentration of free carriers can drop to zero if all the N_t traps capture carriers and E_F can get pinned at the trap level.

3.1.3 Pn-junctions

3.1.3.1 The principle of pn–junctions

Pn–junctions are made up of neighboring p– and n–regions. If one imagines the sudden appearance of two such neighboring p– and n–regions, then the system will no longer be in equilibrium since e.g. the p–region will have a large majority of holes that are weakly bound to the acceptor ions in contrast to a small minority of electrons from the Si atoms. The converse applies to the n–region. These weakly bound charge carriers diffuse into the opposite region leaving behind an ionized dopant atom, N_a^- and N_d^+ in the p– and n–region, respectively. Now, holes diffuse from the p-region to the n–region. This creates an internal electric field, ε_i, from the n–region to the p–region because the diffusing carriers leave behind ionized dopant atoms. This continues until ε_i reaches a sufficient field

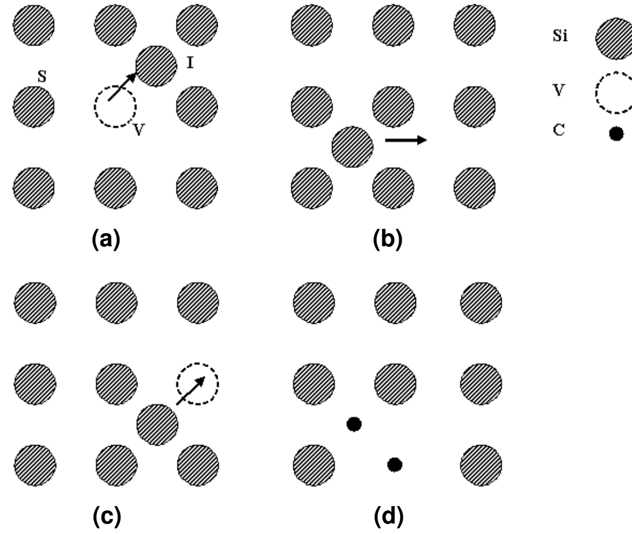

Figure 3.3: Creation of a Frenkel pair, consisting of a vacancy (V) and a self-interstitial (I), from a substitutional (S) **(a)**. Diffusing self–interstitial, by first releasing the bonding energy and then migrating in the crystal **(b)**. Annihilation of a Frenkel pair **(c)**. A carbon interstitial, C_i, together with a carbon substitutional, C_s. This particular cluster defect is known as C_iC_s**(d)**.

strength to create a drift current which exactly balances the diffusion of carriers from one side to the other. When this happens, the region with ionized dopant atoms has become the equilibrium depletion region with a total thickness of W as shown in figure 3.4(a).

The system must obey the principle of detailed balance, meaning that on average the same number of holes must be swept from the n–region to the p–region by ε_i as the number of holes that are diffusing from the p–region to the n–region. Otherwise charge could build up on either side of the junction and the system would not be in equilibrium. Hence, the charge in the ionized p–region must be equal to the charge in the ionized n–region. The length of the regions, $x_{n,p}$, must however *not* be equal, since this depends on $N_{d,a}$.

The depletion approximation states that

- There are no free charge carriers, i.e. carrier depletion, within W. So $p = n = 0$ within W.
- The material is neutral outside of W.

Because of the carrier depletion within W the charge in the p– and n–region can be considered to be from the ionized dopant atoms only, see figure 3.4(b). Charge equality then gives

$$|Q_{n,p}| = qAN_ax_{p,0} = qAN_dx_{n,0} \tag{3.6}$$

where $x_n = x_{n,0}$ at zero bias and correspondingly for x_p.

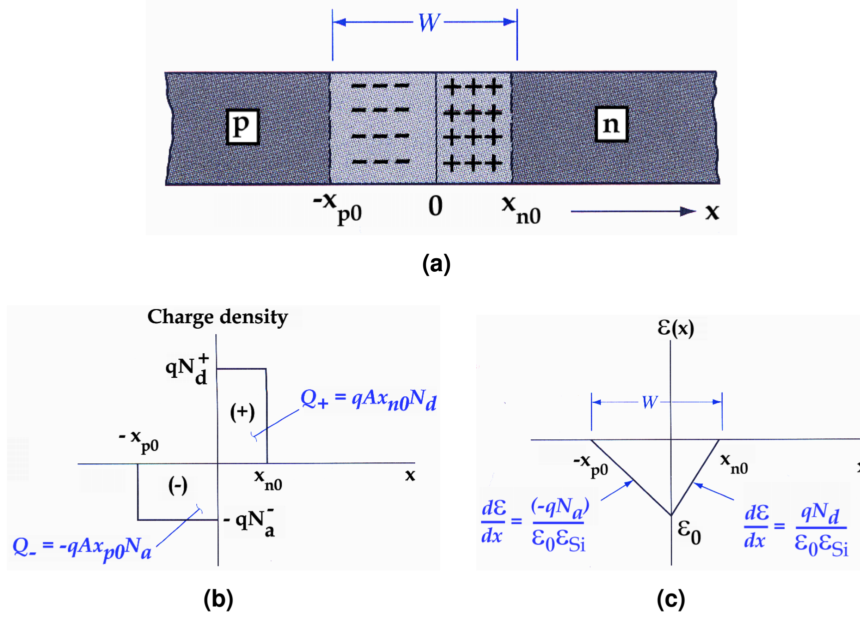

Figure 3.4: **(a)** The basic layout of a pn–junction showing the ionized N_a^- and N_d^+ in the p– and n–regions, respectively. **(b)** The charge density in the p– and n–regions as a function of distance from the junction. **(c)** E–field as a function of distance from the junction. Uniform $N_{a,d}$, an abrupt junction and the depletion approximation are assumed in these figures. All figures adapted from [38].

3.1.3.2 The capacitance of the depletion region

The following is a short resume of the derivation of the capacitance of a pn–junction as written in Streetman [38].

The electric field, ε_i, in the depletion region is given by the Poisson equation,

$$\Delta^2\Phi = -\Delta\vec{E}_i = -\frac{\rho}{\epsilon_{Si}\epsilon_0}$$

Inserting ρ

$$\frac{dE_i}{dx} = \frac{\rho}{\epsilon_{Si}\epsilon_0} = \frac{q}{\epsilon_{Si}\epsilon_0}\left[p + N_d^+ - n - N_a^-\right], \quad \text{for } -x_{p,0} < x < x_{n,0} \tag{3.7}$$

Using the depletion approximation, $p = n = 0$, and the fact that $N_a = 0$ on the n–side and $N_d = 0$ on the p–side this gives a separate equation for ε_i at each side with the condition that they must give the same result at the junction (continuity of ε_i).

$$\frac{dE_i}{dx} = \begin{cases} -\frac{q}{\epsilon_{Si}\epsilon_0}N_a^- & \text{for } -x_{p,0} < x < 0 \\ \frac{q}{\epsilon_{Si}\epsilon_0}N_d^+ & \text{for } 0 < x < x_{n,0} \end{cases}$$

Notice that in the depletion approximation and for constant dopant concentration then ε_i is a linear function of position in the depletion region. The fact that dE_i/dx has different

sign on the two sides, while ε_i must be continuous in $x = 0$, means that ε_i must have an absolute maximum, $\varepsilon_{i,max}$, somewhere in the interval $-x_{p,0} < x < x_{n,0}$. It would be physically reasonable to expect this maximum value to occur at $x = 0$ since this is the position where all of N_a is on the one side and all of N_d on the other as illustrated in figure 3.4(c). Integration over the p–region gives $E_{i,max}$ as

$$E_{i,max} = \int_0^{E_{i,max}} dE_i = -\frac{qN_a^-}{\epsilon_{Si}\epsilon_0} x_{p,0} \tag{3.8}$$

and correspondingly for the n–region. The voltage that is set up over the depletion region by ε_i is

$$V = V_{bi} + V_{rb} = -\int_{-x_{p,0}}^{x_{n,0}} E_i dx = \text{Area under E}_i\text{(x)} \tag{3.9}$$

$$= \frac{1}{2}(-E_{max})(x_{p,0} + x_{n,0}) = \frac{1}{2}\left(\frac{qN_d}{\epsilon_{Si}\epsilon_0} x_{n,0}\right) W \tag{3.10}$$

$$= \frac{1}{2}\frac{q}{\epsilon_{Si}\epsilon_0}\left(\frac{N_a N_d}{N_a + N_d}\right) W^2 \tag{3.11}$$

Upon arranging for the depletion width, W, this becomes

$$W = \left[\frac{2\epsilon_{Si}\epsilon_0}{q}\left(\frac{1}{N_a} + \frac{1}{N_d}\right)(V_{bi} + V_{rb})\right]^{\frac{1}{2}} \tag{3.12}$$

$$\approx \left[\frac{2\epsilon_{Si}\epsilon_0 (V_{bi} + V_{rb})}{qN_d}\right]^{\frac{1}{2}} \tag{3.13}$$

where the last approximation is valid for a p^+–n^-–junction where $N_a \gg N_d$. The capacitance of the depletion region is calculated using $C = \left|\frac{dQ}{dV}\right| = \left|\frac{dQ}{d(V_{bi}+V_{rb})}\right|$ since C is not a linear function of V, so

$$C = \epsilon_{Si}\epsilon_0 A \left[\frac{q}{2\epsilon_{Si}\epsilon_0(V_{bi} + V_{rb})}\left(\frac{1}{N_a} + \frac{1}{N_d}\right)\right]^{\frac{1}{2}} = \frac{\epsilon_{Si}\epsilon_0 A}{W} \tag{3.14}$$

3.1.3.3 Forward and reverse bias

The electron energy bands shift according to the bias that is applied to the diode, as shown for the p^+–n^-–diode in figure 3.5. In correspondance with 3.5(a), with zero bias the diffusion current of majority carriers will be exactly balanced by the drift current of minority carriers. E.g. electrons with sufficient energy can diffuse across W from the n– to the p–region, but at the same time electrons on the p–side that are within one diffusion length from W can diffuse to W and drift against ε_i from the p– to the n–region. The energy barrier that the diffusing majority carriers must overcome is qV_{bi}. In the case of forward bias, as in 3.5(b), the barrier is reduced to $q(V_{bi} - V_{fb})$,the depletion width is $W_{fb} < W_0$ and diffusion of majority carriers dominates. For the reverse biased junction, 3.5(c), the barrier is increased to $q(V_{bi} + V_{rb})$, the depletion width is $W_{rb} > W_0$ and drift of minority carriers dominates.

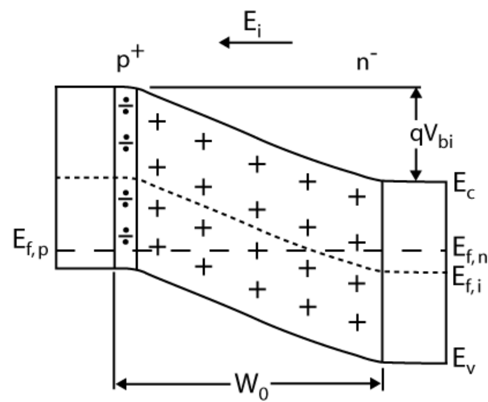

(a) No bias.

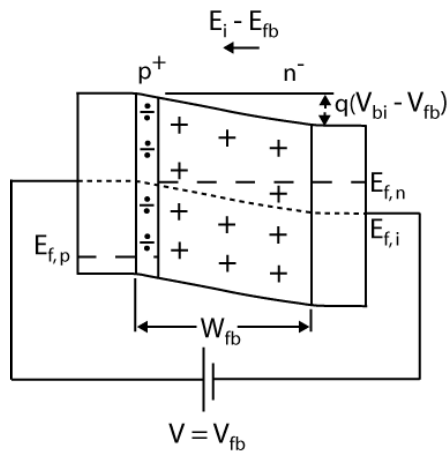

(b) Forward bias.

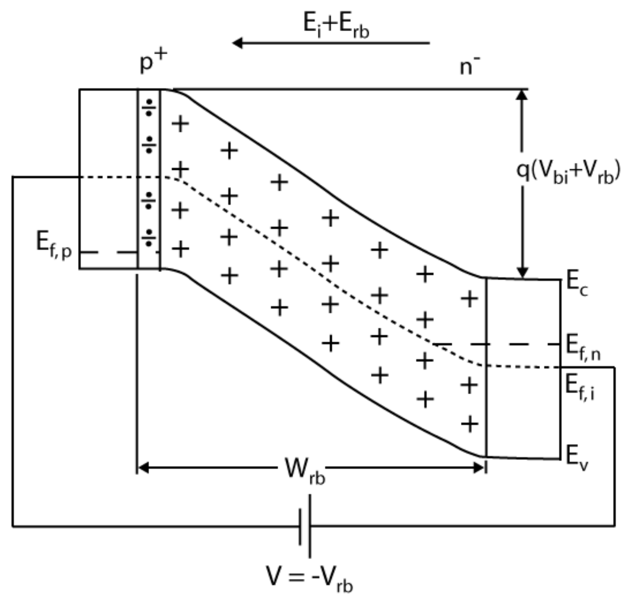

(c) Reverse bias.

Figure 3.5: The pn–junction with no applied bias **(a)**, forward bias **(b)** and reverse bias **(c)**.

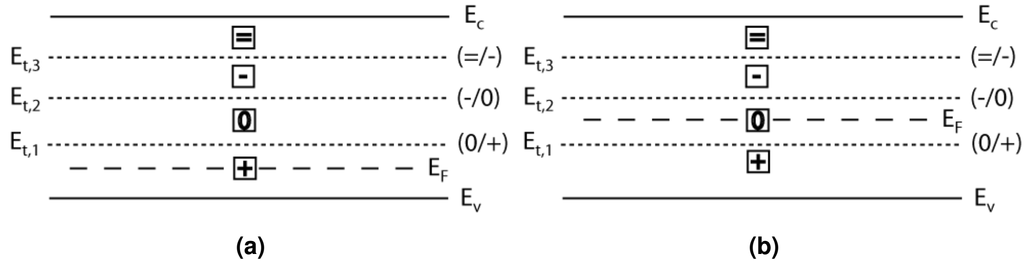

Figure 3.6: Four charge states that give rise to three deep levels of a defect. **(a)** The defect is in the $+$ charge state because no electrons are captured since $E_F < E_{t,1}$. **(b)** The defect has captured one electron and is in the 0 charge state because $E_{t,1} < E_F < E_{t,2}$. The transition from **(a)** to **(b)** is $(0/+)$.

3.1.4 Capture and emission of charge carriers

3.1.4.1 Charge states and deep levels

Some defects can be occupied by more than one electron. The number of occupied electrons on a defect determine the charge state of the defect. Let us assume that a certain defect can have four charge states, i.e. it can capture up to four electrons, and that it is singly positively charged when it is essentially unoccupied by electrons. If it captures one electron then it becomes neutral, the transition would be written $(0/+)$ and it could be measured as an energy level in the band gap of Si. The conventional notation for a charge state transistion is

(charge state after capture of electron / charge state before capture)

Similarly, the defect has two more levels for the transitions $(-/0)$ and $(=/-)$ when it is occupied by two and three electrons, respectively. The transition energies are then $E_{t,1}$, $E_{t,2}$ and $E_{t,3}$ as shown in figure 3.6. When $E_F < E_{t,1}$ then $E_{t,1}$ is essentially unoccupied by electrons as shown by equation (3.19) in the following section. Consequently the defect would be in charge state $+$. When $E_{t,1} < E_F < E_{t,2}$ then $E_{t,1}$ is essentially filled by electrons whereas $E_{t,2}$ is empty, so the defect is in charge state 0 (neutral) and correspondingly for the $-$ and $=$ charge states.

The distinction between shallow and deep levels seems to be relatively loosely defined. A transition between two charge states which give rise to a level 0.05 eV or further away from the nearest band is commonly considered to be a deep level [5]. These levels are not ionized at room temperature, such as e.g. dopants should be. Whether a trap will behave acceptor– or donor–like is determined by the charge state of the trap when it is unoccupied by electrons as described in table 3.2.

3.1.4.2 The rate equation

The total number of traps at a given level E_t is N_t, the number of those traps that are occupied by an electron is n_t and the probabilities for any trap to emit or capture a charge

Type	Charge when	
	unoccupied	occupied
Acceptor-like	0	-
Donor-like	+	0

Table 3.2: Acceptor- and donor-like behavior of electron traps.

carrier per time is $e_{n,p}$ and $c_{n,p}$ for electrons and holes respectively. Then the change in n_t is the sum of captured electrons and emitted holes subtracted by the sum of emitted electrons and captured holes, or in other words

$$\begin{aligned}\frac{dn_t}{dt} &= (c_n + e_p)\,(N_t - n_t) - (c_p + e_n)n_t \\ &= c_n\,(N_t - n_t) + e_p\,(N_t - n_t) - e_n n_t - c_p n_t \end{aligned} \tag{3.15}$$

as visualized in figure 3.7. The physical interpretation of the four terms is as follows:

	Term	Process	Interacting band
$+$	$c_n\,(N_t - n_t)$	Capture of e$^-$ from E_c to unoccupied trap	E_c
$+$	$e_p\,(N_t - n_t)$	Emission of h$^+$ from unoccupied trap to E_v	E_v
$-$	$e_n n_t$	Emission of e$^-$ from occupied trap to E_c	E_c
$-$	$c_p n_t$	Capture of h$^+$ from E_v to occupied trap	E_v

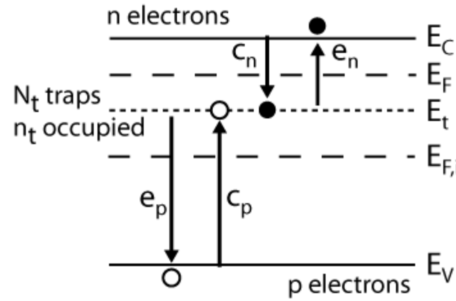

Figure 3.7: A visualization of the four different emission and capture processes. Figure adapted from Blood & Orton [5].

When there is no production of excess carriers, such as from an applied forward bias, then n_t must be in equilibrium, so that overall

$$\frac{dn_t}{dt} = 0$$

In addition, the principle of detailed balance must be followed. The principle of detailed balance applies when the rates of a process and its reverse process must be equal. In this case the capture rate of electrons at E_t must be equal to the emission rate of electrons from E_t and correspondingly for holes. In other words

$$\frac{dn_{t,n}}{dt} = \frac{dn_{t,p}}{dt} = 0$$

If the principle of detailed balance did not apply, then one could have a situation where $dn_t/dt = 0$ was fulfilled, but in such a way that there was a net transfer of electrons from the valence to the conduction band. For instance, the replacement electrons for every electron emitted from E_t to E_c could come as emission of holes to E_c, which is the same as capture of electrons from E_v. Eventually this would lead to the unphysical situation that all the electrons in the material accumulate in the conduction band.

Therefore a steady state condition and the principle of detailed balance requires that

$$e_n n_t = c_n (N_t - n_t) \tag{3.16}$$

$$e_p (N_t - n_t) = c_p n_t \tag{3.17}$$

and solved for the electron occupancy of the trap, $\frac{n_t}{N_t}$, this gives

$$\frac{n_t}{N_t} = \frac{c_n}{e_n + c_n} = \frac{e_p}{c_p + e_p} \tag{3.18}$$

However, the occupancy can also be described through the Fermi-Dirac distribution in equation (3.3) as

$$n_t = N_t f(E_t) \quad \Rightarrow \quad \frac{n_t}{N_t} = f(E_t) = \frac{1}{1 + e^{(E_t - E_F)/kT}} \tag{3.19}$$

Inserted into equation (3.18) this gives the ratio between emission and capture rate as

$$\frac{e_n}{c_n} = e^{(E_t - E_F)/kT} \tag{3.20}$$

$$\frac{e_p}{c_p} = e^{(E_F - E_t)/kT} = \frac{c_n}{e_n} \tag{3.21}$$

3.1.4.3 Capture rate

An expression for the capture rate can be found by fairly straightforward geometrical considerations. Consider figure 3.8. The defect is represented as a sphere with a radius which is equal to the maximum length of the attractive coloumb forces from the defect. That means that the defect in the figure does not have the actual, physical size of the defect as it is in the lattice of Si, but the size of the sphere with the radius of the attractive coloumb forces. The cross section of this sphere in the plane which is perpendicular to the thermal velocity of the electrons is the capture cross section. The electrons that pass through the capture cross section will thus come within range of the attractive coloumb forces and will be captured, whereas all other electrons will not. The volume of electrons that will pass through the cross section is $\sigma_n L = \sigma_n v_{th,n} \Delta t$ and therefore the number of captured electrons from a single trap in the time Δt is

$$\Delta n_1 = \underbrace{\sigma_n v_{th,n} \Delta t}_{\text{Volume}}\, n = \sigma_n \underbrace{v_{th,n} n}_{\text{Flux}}\, \Delta t$$

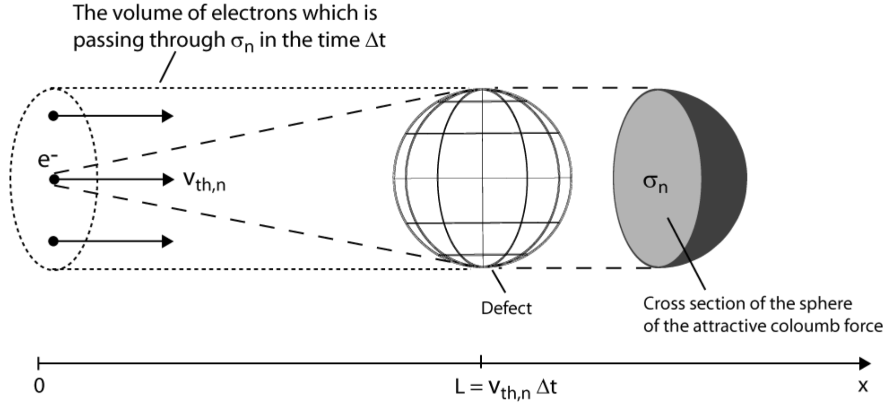

Figure 3.8: Geometrical interpretation of the capture cross section for electrons, σ_n.

and for all the $(N_t - n_t)$ unoccupied traps the number of captured electrons in Δt will be $\Delta n_t = \Delta n_1 (N_t - n_t)$. Now, the capture rate per unoccupied trap can be written as

$$c_n = \frac{\Delta n_t / \Delta t}{N_t - n_t} = \sigma_n v_{th,n} n \tag{3.22}$$

and correspondingly for hole capture. Notice that the capture rate is proportional to the relevant carrier concentration. σ_n for a defect in a neutral charge state is commonly measured to be somewhere around 10^{-14} cm^2. If σ_n is measured to be very small, e.g. something like 10^{-17} cm^2, then the defect can often be assumed to already have been occupied with an electron before capturing a second electron. That is, the defect was in a $(-)$ charge state and after capturing another electron it is in the $(=)$ charge state. The converse applies to hole capture.

3.1.4.4 Emission rate

Inserted for c_n from (3.22) and n from (3.1) in (3.21) the emission rate for electrons in a non–degenerate semiconductor $(n < N_c)$ can be written as

$$e_n = c_n e^{(E_t - E_F)/kT} = \sigma_n v_{th,n} N_c e^{-\frac{E_c - E_t}{kT}} \tag{3.23}$$

Notice that the emission rate is independent of the position of E_F, i.e. independent of n, unlike the capture rate. Therefore the emission rate is a characteristic property of the trap itself, and only a function of the temperature. One can now calculate the ratio between the emission rates for electrons and holes, which is

$$\frac{e_n}{e_p} = \frac{\sigma_n v_{th,n} N_c}{\sigma_p v_{th,p} N_v} \exp\left(\frac{E_g - 2(E_c - E_t)}{kT}\right) \tag{3.24}$$

where the exponential is

$$e^{\frac{E_g - 2(E_c - E_t)}{kT}} \begin{cases} > 1 & \text{if } E_c - E_t < E_g/2 \text{ so } E_t \text{ is in the upper half of } E_g \\ = 1 & \text{if } E_c - E_t = E_g/2 \text{ so } E_t \text{ is somewhere around } E_g/2 \\ < 1 & \text{if } E_c - E_t > E_g/2 \text{ so } E_t \text{ is in the lower half of } E_g \end{cases}$$

Type of trap	
Electron	$E_t > E_{equal}$
Both	$E_t \sim E_{equal}$
Hole	$E_t < E_{equal}$

Table 3.3: Electron and hole traps.

The factors themselves in the pre–exponential part of the emission rate are all functions of temperature, but their ratios are not. In fact

$$\frac{\sigma_n v_{th,n} N_c}{\sigma_p v_{th,p} N_v} \sim \frac{\sigma_n}{\sigma_p}$$

since the thermal velocities of electrons and holes and the density of states in the conduction and valence band are of the same order of magnitude. The capture cross section is temperature independent in the ideal case.

The energy level, E_{equal}, where $e_n = e_p$ is equally much an electron and a hole trap. By setting $e_n = e_p$ in equation (3.24) E_{equal} is found to be

$$E_{equal} = \frac{E_g}{2} + \frac{kT}{2} ln \left(\frac{\sigma_p v_{th,p} N_v}{\sigma_n v_{th,n} N_c} \right) \tag{3.25}$$

A definition of electron and hole traps can be based on equation (3.25), as in table 3.3.

3.1.4.5 Activation enthalpy and apparent capture cross section

The energy that is required to remove an electron from E_t to E_c is the chemical potential, which is equivalent to the increase in Gibbs free energy, $\Delta G(T) = E_c - E_t$. This is the energy that the electron needs to get excited into the conduction band [6]. However, $\Delta G(T)$ is a function of temperature and from a thermodynamic identity

$$\Delta G(T) = E_c(T) - E_t(T) = \Delta H - T\Delta S \tag{3.26}$$

Inserted into equation (3.23) this means that

$$\begin{aligned} e_n &= \sigma_n v_{th,n}(T) N_c(T) e^{-\frac{\Delta G(T)}{kT}} \\ &= e^{\frac{\Delta S}{k}} \sigma_n v_{th,n}(T) N_c(T) e^{-\frac{\Delta H}{kT}} \\ &= \sigma_{na} v_{th,n}(T) N_c(T) e^{-\frac{\Delta H}{kT}} \end{aligned} \tag{3.27}$$

where the last expression shows that the extracted values from an Arrhenius plot of $\ln(e_n(T)/T^2)$ is actually $\sigma_{na} \equiv e^{\frac{\Delta S}{k}} \sigma_n$ and ΔH. σ_{na} is called the apparent capture cross section and ΔH is called the activation enthalpy.

3.1.4.6 Separation of capture and emission by a pn–junction

The reason for doing measurements on a pn–junction is that in a depletion region it is possible to separate the capture and emission processes which otherwise would be competing against each other. This is because in a depletion region the conduction and valence bands will be depleted of their respective charge carriers, which have been swept away by the built–in electric field. The traps can then be sequentially filled and emptied by applying the appropriate bias, see section 4.2.3 about DLTS.

It is common to use an asymmetrical junction, e.g. p^+–n^-. Then the depletion region can be assumed to be only in the n–region. By pulsing the voltage over the pn–junction from a reverse voltage to 0, the emission from only electron traps is measured. Correspondingly, by using a n^+–p^- junction emission from only hole traps is measured.

There are many experimental techniques where the principle is to apply a bias pulse to a reverse biased pn–junction to measure the filling and emptying of the traps within the depletion region. Examples of such techniques are deep level transient spectroscopy (DLTS) and thermally stimulated current (TSC).

For an electron trap in the depletion region of a pn–junction all interaction with the valence band can be ignored, and in addition $c_n = 0$ since $n = 0$. Then the rate equation (3.15) becomes simply

$$\frac{dn_t}{dt} = -e_n n_t \tag{3.28}$$

which can be integrated easily. When assuming that the trap was completely occupied at $t = 0$, i.e. $n_t(t = 0) = N_t$, then the result is a simple exponential decay with the rate constant $\tau = e_n(T)^{-1}$.

$$n_t(t) = N_t e^{-e_n(T)t} \tag{3.29}$$

3.1.5 Reaction kinetics

The rate of reaction between two defects depends on [43]

1. The probability that the defects will come close enough to each other to react.
2. The probability that their energies are such that they actually can react when they do encounter each other.

If the energy required for diffusion is larger than the energy required for reaction of two nearby defects, then the reaction rate is said to be diffusion-limited since the defects will probably react with each other if they meet. This means that the probability that the defects will encounter one another is the important factor.

The defect reactions that are considered in this thesis are diffusion–limited where the reaction rate is limited by the activation energy for diffusion of the defects.

The probability of migration for a defect or an impurity from one position to another in the crystal potential, can be described by the diffusion coefficient, $D(T)$, which is

$$D(T) = D^0 e^{-\frac{E_a}{kT}}. \tag{3.30}$$

D^0 can be interpreted as a trial frequency of the defect or impurity to jump over the potential barrier which separates one stable position from another, and $\exp(-E_a/kT)$ is a Boltzmann factor which gives the probability that the defect or impurity has the required activation energy[1], E_a, to migrate to another position.

3.1.5.1 Diffusion–limited reactions

A reaction which involves only one defect, e.g. a dissociation of A into its less complex parts, such as

$$A \rightarrow A_1 + A_2 \tag{3.31}$$

is described simply by [13,41]

$$\frac{\partial[A]}{\partial t} = -\frac{\partial[A_1]}{\partial t} = -\frac{\partial[A_2]}{\partial t} = -c(T)[A] \tag{3.32}$$

which can be derived from the law of mass action in chemical thermodynamics.

A general diffusion–limited reaction between two defects, A and B, such as

$$A + B \rightarrow AB \tag{3.33}$$

is quantitatively described by the differential equation

$$\frac{\partial[A]}{\partial t} = \frac{\partial[B]}{\partial t} = -c(T)[A][B] \tag{3.34}$$

where $c(T)$ is the reaction rate. The reaction rate does not vary with $[A]$ or $[B]$, but it is a function of temperature.

$$c(T) = c_0 e^{-\frac{E_a}{kT}} \tag{3.35}$$

where c_0 is the reaction rate constant which is independent of temperature. E_a is a characteristic energy that determines the temperature at which the dissociation or migration can start to happen. Since these reactions are diffusion–limited the measured reaction energy is expected to equal the activation energy for migration of the mobile species, as in equation (3.30). In fact, the temperature dependence of $c(T)$ is assumed to originate from $D(T)$. The pre–exponential factor, c_0, incorporates the diffusion pre–exponential factor,

[1]Not to be confused with the activation enthalpy of carrier emission from defects as in equation (3.27)

and it can be interpreted as the probability for the encounter of two reacting defects. It can also indicate whether the reaction is a dissociation or a migration by

$$c_0 \begin{cases} \approx \frac{kT}{h} & \text{likely a dissociation} \\ \ll \frac{kT}{h} & \text{likely a migration} \end{cases}$$

where $\frac{kT}{h}$ is approximately the frequency of the most numerous phonons in the lattice [13, 29]. This quantitiy is on the order of $10^{12} - 10^{13}$ s^{-1} for temperatures 77 – 300 K. k is the Boltzmann constant and h is the Planck constant.

The reactions in equations (3.31) and (3.33) are termed first and second order reactions respectively as will be explained below.

3.1.5.2 1st order reactions

Equation (3.32) is an example of a first order reaction, because it is on the general form

$$\frac{\partial[A]}{\partial t} = -c(T)[A]^n \tag{3.36}$$

with order $n = 1$. When $n = 1$ this equation is readily integrated to

$$[A] = ae^{-c(T)t} + b \tag{3.37}$$

where a, b are constants to be determined from the initial conditions.

For first order growth the initial conditions are

$$[A](t = 0) = [A]_{0,min}$$
$$[A](t = \infty) = [A]_{\infty,max}$$

and the solution becomes

$$[A] = [A]_{\infty,max} - \Big\{[A]_{\infty,max} - [A]_{0,min}\Big\}e^{-c(T)t}$$

where it is often assumed that $[A]_{0,min} = 0$. A plot of $\ln\Big([A]_{\infty,max} - [A]\Big)$ will be linear and $c(T)$ is the slope.

For first order decay the initial conditions are the other way around, i.e.

$$[A](t = 0) = [A]_{0,max}$$
$$[A](t = \infty) = [A]_{\infty,min}$$

so the solution is

$$[A] = \Big\{[A]_{0,max} - [A]_{\infty,min}\Big\}e^{-c(T)t} - [A]_{\infty,min}$$

and it can often be assumed that $[A]_{\infty,min} = 0$. A plot of $\ln\Big([A] - [A]_{\infty,min}\Big)$ will be linear and $c(T)$ is the slope.

Notice that the fractional concentration is independent of the initial concentration for both growth and decay. First order reactions are also termed monomolecular, indicating that only one species is reacting.

3.1.5.3 2nd order reactions and special cases

A second order reaction obeys one of the following rate equations

$$\frac{\partial[A]}{\partial t} = -c(T)[A]^2 \tag{3.38}$$

$$\frac{\partial[A]}{\partial t} = -c(T)[A][B] \tag{3.39}$$

and equation (3.34) corresponds to a general second order reaction of the latter kind.

According to [43], for a uniform initial distribution of defects as is expected to be produced by electron irradiation, equation (3.34) can further be written as

$$\begin{aligned} \frac{\partial[A]}{\partial t} &= -4\pi R(D_A + D_B)\left(1 + \frac{R}{\sqrt{\pi D t}}\right)[A][B] \\ &\approx -4\pi R(D_A + D_B)[A][B] \qquad \text{when } t \gg \frac{R^2}{D} \end{aligned} \tag{3.40}$$

where the last expression is valid after an initial transition time which will not be taken into account in this thesis. R is the capture radius of the reaction. It is simply the maximum distance that the two defects can have to each other for the reaction to take place, and it is a specific to each reaction.

Several assumptions can often be made to simplify equation (3.40). Firstly, it is often true that only one of the two reacting species are mobile at the temperature of the reaction. This implies that the diffusion coefficient of the mobile species is much larger than that of the other species, say $D_A^0 \gg D_B^0$ so that $D = D_A + D_B \approx D_A$, and consequently that

$$\frac{\partial[A]}{\partial t} \approx -4\pi R D[A][B] = -4\pi R D_A^0 e^{-\frac{E_a}{kT}}[A][B]$$

Furthermore, if one of the species has a much larger initial concentration than the other, say $[A]_{t=0} \ll [B]_{t=0}$, such that $[B] \approx [B]_{t=0}$, then

$$\frac{\partial[A]}{\partial t} = -4\pi R D_A^0 e^{-\frac{E_a}{kT}}[B]_{t=0}[A] = -c_0 e^{-\frac{E_a}{kT}}[A] \tag{3.41}$$

where $c_0 = -4\pi R D_A^0[B]_{t=0}$ is recognized as the rate constant. The temperature dependence in $c(T)$, $e^{-\frac{E_a}{kT}}$, is interpreted as coming from the diffusion coefficient, $D_A(T)$.

Equation (3.41) is now clearly reduced to the form of a first order reaction, which is to be expected since only one defect from the mobile species is assumed to be lost in each reaction between an A and a B. The mobile species of low concentration, A, is said to be depleted by the immobile species of high concentration, B.

One can now imagine a defect which is involved in two first order processes simultaneously, e.g. it disappears both through dissociation and reaction with a species B as

$$A \rightarrow A_1 + A_2 \tag{3.42}$$

$$A + B \rightarrow AB \tag{3.43}$$

where $[A]_{t=0} \ll [B]_{t=0}$. Now A disappears as

$$\begin{aligned}\frac{\partial [A]}{\partial t} &= -4\pi RD[B]_{t=0}[A] - c_{diss}[A] \\ &= -\left\{c_A + c_{diss}\right\}[A]\end{aligned} \quad (3.44)$$

with solution

$$\frac{[A]}{[A]_{t=0}} = -e^{\{c_A(T)+c_{diss}(T)\}t} \quad (3.45)$$

In the context of a dissociation, c_{diss} is called the dissociation rate of A. On the other hand, the reaction product AB is created when A is destroyed, although some A dissociate instead of producing AB, so the equation and solution for AB is

$$\begin{aligned}\frac{\partial [AB]}{\partial t} &= -c_A[A] \\ [AB] &= \frac{[A]_{t=0}}{1 + c_{diss}/c_A}\left(1 - e^{-(c_{diss}+c_A)t}\right)\end{aligned} \quad (3.46)$$

The above suggests that when there is a very large difference in the concentrations, a bimolecular reaction actually follows first order kinetics. However, if this is not the case, then the reaction will be second order. A general second order reaction, as given by the rate equation (3.39), can not as easily be characterised as first order reactions can. This is because a first order reaction can only be either a dissociation or a reaction between two defects with very different concentrations.

An exception is if the bimolecular reaction follows the rate law in equation (3.38), i.e. if the two reacting defects are in fact the same so that A = B. The reaction of two vacancies, V, into the divacancy, V_2, is an example of such a reaction. The integrated rate equation is

$$[A] = \frac{[A]_{t=0}}{1 + [A]_{t=0}c_A t} \quad (3.47)$$

and it is not linear in a $\ln[A]$ vs. t plot as the linear reaction in equation (3.37) is. This is used to distinguish between first and higher order reactions.

The fractional decay, $[A]/[A]_{t=0}$, depends on the initial concentration for a second order reaction. At short times when $[A]_{t=0}c_A t \ll 1$, the fractional decay will be linear, $[A]/[A]_{t=0} = 1 - [A]_{t=0}c_A t$. At long times when $[A]_{t=0}c_A t \gg 1$, the fractional decay will be inversely proportional to $[A]_{t=0}c_A t$.

3.2 Radiation damage in Si

3.2.1 Stopping and damage production

Different kinds of radiation generate different kinds of damage in silicon, because the mechanism for causing the damage depends on the mass, energy and charge, i.e. the overall nature of the radiation. The incident particle will lose energy through a combination

of electronic and nuclear stopping, where the former is a viscous drag from coulombic interaction with the huge number of electrons around the lattice atoms and the latter is elastic scattering at the more moderate number of lattice nuclei in the path of the incident particle. The total energy loss is then described by [8, Ch. 5]

$$\frac{dE}{dx} = \left.\frac{dE}{dx}\right|_e + \left.\frac{dE}{dx}\right|_n \tag{3.48}$$

Electronic stopping will result in the ionization of some lattice atoms when an electron is excited by the energy it picks up from the incident particle, but this causes no permanent damage in a conductive or semiconducting material[2]. Nuclear stopping, on the other hand, transfers energy from the incident particle to the lattice atoms which then recoils. If the transferred energy is large enough, then the lattice atom will escape from its original lattice site and into some interstitial location leaving behind a vacancy which together are a Frenkel pair. Nuclear stopping causes a non–ionizing energy loss (NIEL) whereas electronic stopping causes ionizing energy loss. Radiation which is stopped largely by NIEL creates more Frenkel pairs, and thus more permanent damage, in semiconductors than mostly ionizing radiation does.

The transfered energy between the radiation particle and a Si atom must be larger than a certain threshold energy, E_d. E_d is the energy required to displace the Si atom, because of the binding energy between the neighboring Si atoms in the crystal. If the transfered energy is much larger than E_d, then the displaced target atom can displace other target atoms and thus create a disordered region with clusters of vacancies and displaced Si interstitials.

As derived in [7], the maximum transferable energy in elastic scattering for a head–on collision, i.e. the impact parameter $b = 0$, at non–relativistic energies is

$$T_{max} = \frac{4Mm}{(m+M)^2}E \tag{3.49}$$

where m is the mass and E is the initial energy of the incident particle. M is the mass of the target atom which is assumed to be at rest initially. At relativistic energies for the incident particle this becomes

$$T_{max} = 2\frac{m_0}{M}\left(2 + \frac{E}{m_0c^2}\right)E \tag{3.50}$$

where m_0 is the rest mass of the incident particle.

The energy threshold for displacing a silicon atom and producing a Frenkel pair where the vacancy is left at the lattice site and the Si atom becomes an interstitial is roughly 25 eV[3] [20,29]. This is about four times the energy which is required to break an Si-Si bond, 4×5.9 eV $= 23.6$ eV, as might be expected. However, the energy required to produce a recoil with sufficient energy to create a clustered region is much larger, about 5 keV [29].

[2]But it could cause permanent damage in dielectrics, e.g. positive charge in oxides.

[3]At least it seems to be somewhere between 11 – 40 eV. It is difficult to determine exactly since a lot of Frenkel pairs annihilate within a few picoseconds before they can be measured [20].

Because of its small mass, electrons need an initial energy above 250 keV in order to transfer an amount of energy equal to E_d in a head–on collision with an Si atom at maximum energy transfer. The incident electrons need a larger energy if the energy transfer is less than maximal. In order for the now displaced so–called primary knock–on atom (PKA) to create secondary displacements, the electron needs to have an energy of several MeV. Because of this rather high required energy for secondary damage production, electron radiation is assumed to create mainly monovacancies and the divacancy cluster defect. Divacancies are created by the direct production of two vacancies in immidiate proximity, and from pairing of two independently created monovacancies. A primary collision and a cascade of secondary collisions are illustrated in figure 3.9. The amount of directly produced vacancy clusters of higher order is expected to be small.

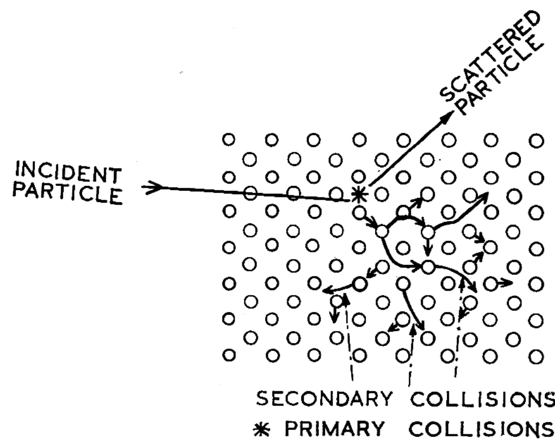

Figure 3.9: Radiation damage by a primary collision with the PKA and a range of possible secondary collisions. From [16].

Gamma radiation actually damages semiconductors in much the same way as electron radiation, although with a lower amount of displacements per incident particle. This is because gamma radiation is absorbed by the valence electrons of the crystal atoms, in a process called Compton scattering. The electrons can then become so energetic that they displace a PKA, and also produce divacancies to a more limited extent. Gamma radiation is often produced by the radioactive decay of ^{60}Co, which produces $\sim$1 MeV γ-radiation and also sub–MeV electron radiation.

Neutrons have a large mass and no electric charge. Therefore they are not affected by electronic stopping nor Coloumb interaction with the crystal nuclei, but they produce damage only through head–on collisions with a PKA. Then the energy transfer will often be near maximum and the PKA will often have enough energy to start a cascade of secondary displacements and create a volume with a large number of clustered defects. Neutrons also have a large projected range due to the lack of charge to cause energy loss through Coloumb interaction. The amount of clustering produced by neutron radiation could be the reason that oxygenation does not reduce the type inversion effect in the way it does for other types of radiation, as briefly described in section 3.3.1.

Protons and heavier ions, on the other hand, have a positive electric charge in addition to a large mass. They therefore lose some energy to the crystal atoms through Coloumb

interaction with nuclei, conduction and valence electrons even if there is no head–on collision. This means that more single Frenkel pairs will be created and the amount of clustering will be reduced as compared to neutron radiation with the same energy.

3.2.2 Impurities and radiation induced point defects in silicon

As mentioned in the previous section, the point defects which are primarily created during electron irradiation of silicon are self–interstitials (S_{Si}), vacancies (V) and directly produced divacancies (V_2) [10, 11]. These are so–called intrinsic defects since they do not involve impurities. At room temperature these defects will then migrate and form more complex point defects with impurity atoms in the silicon, mainly oxygen, carbon and hydrogen, with the exception of V_2 which is stable to much above room temperature. The physical configurations of interstitial oxygen (O_i), the vacancy–oxygen complex (VO) and V_2 in the Si crystal are shown in figure 3.10.

Monovacancies and self–interstitials are highly mobile at room temperature, so the majority will immidiately annihilate with each other. Often the annihilating pair was actually created together as a Frenkel pair, and this is called correlated annihilation. The surviving monovacancies can easily find, say, interstitial oxygen atoms which are immobile at room temperature. Together they can form the vacancy–oxygen defect VO in the reaction $V + O_i \rightarrow VO$. This happens during and immidiately after room temperature irradiation.

Oxygen escapes from the fused silica (SiO_2) crucible that contains the silicon melt during Czochralski growth at $\sim$1500 °C (chapter 2.4 in [8]) and is thus incorporated in the Si when a boule is pulled out of the melt, whereas carbon comes from components such as graphite heat shields around the crucible. Oxygen and carbon are usually the impurities in silicon with the largest concentrations, apart from dopants such as boron or phosphorous in strongly doped regions.

3.3 Previous work

Some of the previous work which this thesis is based on will be presented in this section.

3.3.1 Type inversion of silicon radiation detectors

After $p^+ - n^- - n^+$ silicon detectors became widely used for the innermost detectors in high energy physics experiments it was observed that the n^- layer gradualy transformed into a p^- layer as the effective doping, $N_{eff} = N_a - N_d$, changed sign. This was assumed to be due to the formation of one or more acceptor defects with a concentration which increased as the dose increased.

The work of the Cern RD48 (ROSE) collaboration [9] showed that the type inversion was largely suppressed for proton radiation in oxygen rich materials, whereas it was promoted

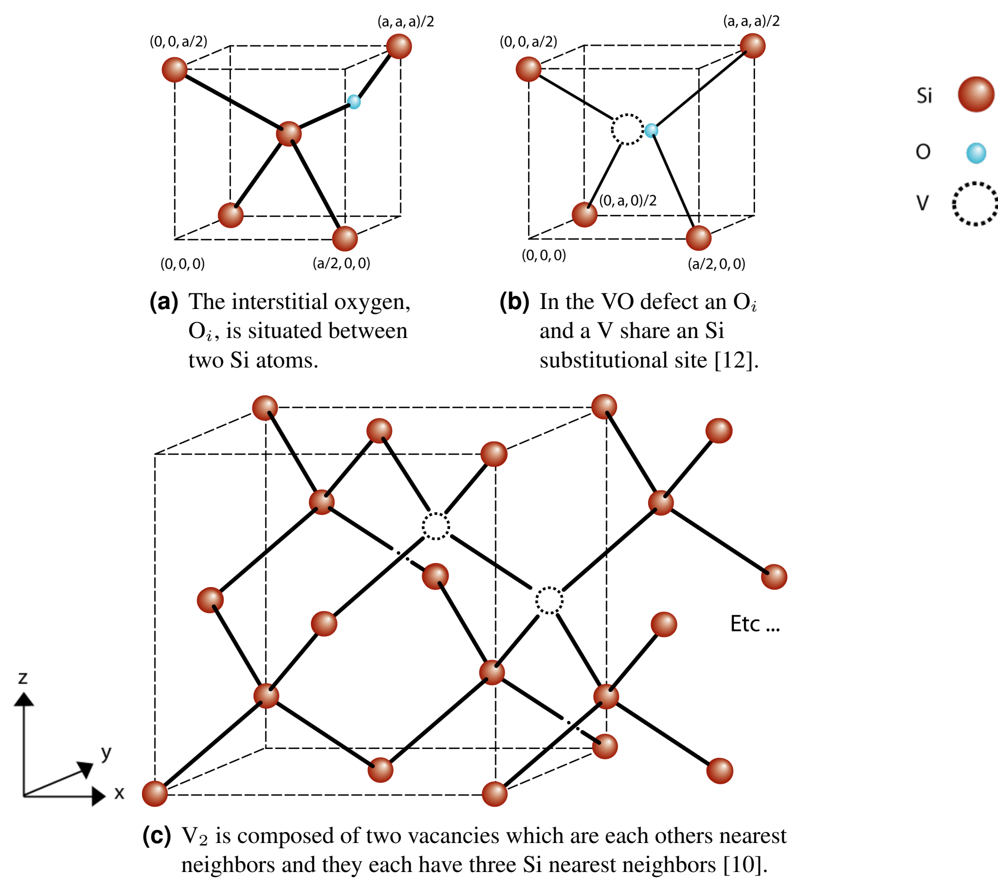

(a) The interstitial oxygen, O_i, is situated between two Si atoms.

(b) In the VO defect an O_i and a V share an Si substitutional site [12].

(c) V_2 is composed of two vacancies which are each others nearest neighbors and they each have three Si nearest neighbors [10].

Figure 3.10: A visualization of the structure of O_i **(a)**, VO **(b)** and V_2 **(c)**.

in carbon rich silicon. However, there was no change in the radiation hardness for neutron radiation and this might be connected to the amount of cluster defects which are created in neutron irradiated silicon. An example of type inversion for increasing dose in 1 MeV neutron equivalents is shown in figure 3.11. The so–called I defect is believed to be responsible for type inversion [36], however the indentity of I has not yet been found as described in section 3.3.4.

Part of the motivation for studying radiation induced defects in epitaxial silicon is that this material has been reported to display a very large resistance to type inversion [19].

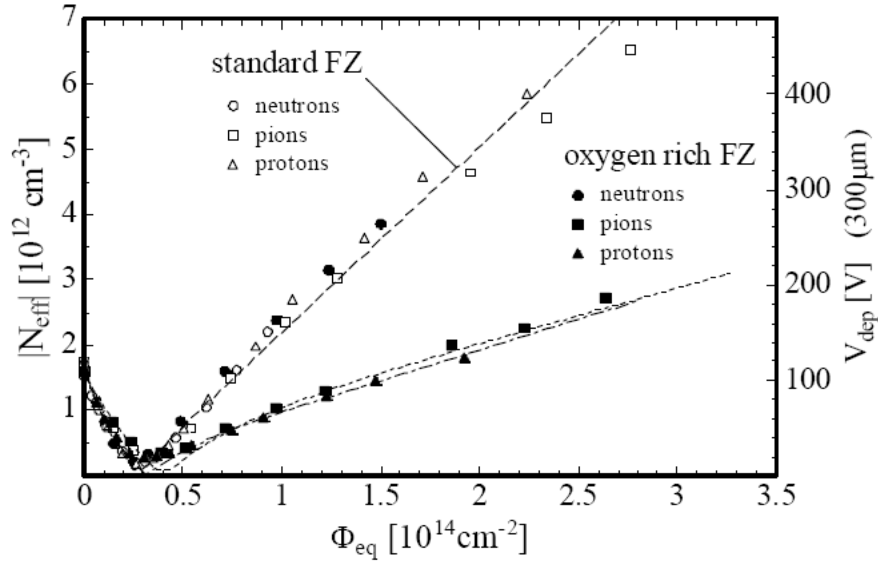

Figure 3.11: Type inversion in neutron and proton irradiated silicon. The graph is from the 3rd RD48 status report [9].

3.3.2 Importance of dose and oxygen concentration (O_i) on the generation and annealing of the vacancy–oxygen (VO), divacancy (V_2) and divacancy–oxygen (V_2O) complexes

The following is a summary of the results of works such as reference [24, 25] and references therein.

During room temperature irradiation of silicon, VO is created through the reaction

$$V + O_i \rightarrow VO \tag{3.51}$$

Whether this reaction follows first or second order kinetics depends on whether $[O_i]$ is much higher than or comparable to [V] respectively. V_2O can then be formed by

$$V + VO \rightarrow V_2O \tag{3.52}$$

which will be a second order process due to the comparable concentrations of V and VO. Alternatively V_2 is created first and V_2O is subsequently formed through reaction with

O_i.

$$V + V \rightarrow V_2 \tag{3.53}$$

$$V_2 + O_i \rightarrow V_2O \tag{3.54}$$

The production of higher-order multivacancies than V_2 is of course also taking place, but the reactions become less probable with increasing number of vacancies in the complex and so it will be ignored for simplicity in this context.

However, neither VO, V_2 nor O_i are mobile at room temperature so the latter reaction can only happen at elevated temperatures, that is during subsequent annealing experiments. In contrast, the monovacancy is highly mobile at room temperature, so the production of V_2O during irradiation must go through the reaction $V + VO \rightarrow V_2O$ if it happens at all. The second order reaction $V + V \rightarrow V_2$ will in principle compete for the monovacancies, but most divacancies are expected to be created directly by electron radiation so this reaction can be neglected during irradiation [10]. The rate of change in the concentration of V during irradiation is then

$$\frac{d[V]}{dt} = g_V^{eff} - 4\pi R D_V [V]\{[O_i] + [VO]\}$$

where g_V^{eff} is the effective generation rate of V by the radiation where annihilation of Frenkel pairs is included. g_V^{eff} is determined by the dose rate, that is the number of incident electrons per time (current). With a constant dose rate the concentration of V stabilizes at some steady state value after a transient time. At the steady state value the rate of change is zero, so $d[V]/dt = 0$ and

$$[V] = \frac{g_V^{eff}}{4\pi R D_V \{[O_i] + [VO]\}}$$

Now the generation rate of V_2O is

$$[V_2O] = 4\pi R D_V [V][VO] = g_V^{eff} \frac{[VO]}{[O_i] + [VO]}$$

It seems clear that the production of V_2O through $V + VO \rightarrow V_2O$ depends on the ratio of the concentration of [VO], which increases with increasing radiation dose, and $[O_i]$.

$$\frac{[VO]}{[VO] + [O_i]} \quad \begin{array}{l} \leftarrow \text{[VO] is radiation induced, depends on dose} \\ \leftarrow [O_i] \text{ depends on the growth and processing of Si} \end{array}$$

This divides the situation into two limiting cases for a given dose rate.

3.3.2.1 Low dose or large $[O_i]$

In this case the concentration of radiation induced VO will be small compared to the concentration of interstitial oxygen, $[O_i] \gg [VO]$. Then the production of VO depletes

the monovacancy concentration and leaves few V left to produce V_2O through $V + VO \rightarrow V_2O$.

However, V_2O can be created through equation $V_2 + O_i \rightarrow V_2O$ during subsequent annealing experiments at high enough temperatures to make V_2 mobile. This is an important annealing mechanism of V_2 as explained in the following section.

The doses that are relevant to deep level transient spectroscopy (DLTS) studies are all within this low dose regime. DLTS is discussed in section 4.2.3.

3.3.2.2 High dose or small [O_i]

In this case [VO] is comparable to or exceeds [O_i], so it is O_i that becomes depleted by the production of VO. Hence, the production of V_2O through $V + VO \rightarrow V_2O$ can proceed in competition with the production of V_2 according to $V + V \rightarrow V_2$.

3.3.3 The influence of hydrogen on the generation and annealing of VO, V_2 and V_2O

Monakhov et al. published an article [31] on the influence of hydrogen, monatomic and diatomic, on the generation and annealing of VO, V_2 and V_2O which is summarized in this section. Two float zone (FZ) samples received the same oxygenation treatment and were thus made into so–called diffusion oxygenated float zone (DOFZ). One of the samples were then also hydrogenated after which both samples were electron irradiated.

After irradiation there will be a certain concentration of VO and V_2 and here it will be assumed that only a negligible amount of V_2O is created during the irradiation itself, as would be the case for large [O_i] when the formation of VO is favored. At temperatures much above room temperature, VO and V_2 become mobile and can migrate in the silicon crystal. Then V_2O can be created through the reactions (3.52) and (3.54), but VO could also react with O_i or mono- and diatomic hydrogen as

$$VO + O_i \rightarrow VO_2 \tag{3.55}$$

$$VO + H \rightarrow VOH \tag{3.56}$$

$$VO + H_2 \rightarrow VOH_2 \tag{3.57}$$

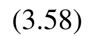

(3.58)

where VO_2 and VOH_2 are expected to not be electrically active, whereas VOH gives rise to two levels $VOH^{0/+}$ and $VOH^{-/0}$ with energies $E_t - E_v = 0.28$ eV and $E_c - E_t = 0.32$ eV, respectively, according to references [15, 39]. V_2 can react with hydrogen as

$$V_2 + H \rightarrow V_2H \tag{3.59}$$

$$V_2H + H \rightarrow V_2H_2 \tag{3.60}$$

$$V_2 + H_2 \rightarrow V_2H_2 \tag{3.61}$$

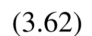

(3.62)

where V_2H has a deep acceptor level at 0.43 eV and theory predicts a shallower 0.2 eV acceptor level to V_2H_2 which has not yet been observed experimentally **??**.

3.3.3.1 Low concentration of hydrogen

As can be seen in the isothermal annealing from 200 – 300 °C in figure 3.12(a), there is no discernible change in [VO] whereas the transformation from V_2 to V_2O exhibits a near one–to–one relationship at about 300 °C in the non–hydrogenated material. A minor level also appears at the position ∼160 K.

3.3.3.2 High concentration of hydrogen

In the hydrogenated sample almost all of the V_2 anneal out at about 275 °C while essentially no V_2O is formed. At the same temperature VOH grows rapidly to approximately the initial amplitude of V_2, as can be seen from the DLTS spectra in figure 3.12(b).

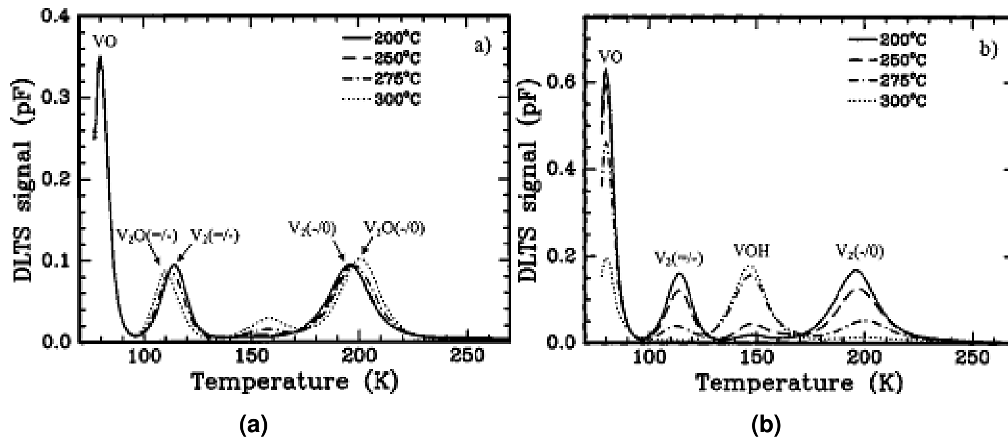

Figure 3.12: Low concentration of hydrogen **(a)**. High concentration of hydrogen **(b)**. DLTS spectra from reference [31].

3.3.3.3 Interpretation

The normalized amplitudes of the major peaks have been plotted as functions of annealing temperature in figure 3.13. VO, V_2 and V_2O have noticably lower thermal stabilities in the hydrogenated compared to the non-hydrogenated material, and VOH appears only in the hydrogenated sample. This is interpreted as hydrogen-assisted annealing where the reactions between VO, V_2 and H or H_2 are preferred over the creation of V_2O.

However, V_2H is expected to have a deep acceptor level at 0.43 eV and to completely overlap with the DLTS peak for $V_2^{-/0}$. This would lead to an asymmetric decrease of the amplitudes of $V_2^{-/0}$ and $V_2^{=/-}$. No such asymmetry was observed. In fact, a very close to one-to-one relationship between the two acceptor levels of V_2 has been observed, so the reaction $V_2 + H \rightarrow V_2H$ is not a dominant process in this hydrogenated material. It is

suggested that V_2 disappears through the reaction with hydrogen dimers [4] as $V_2 + H_2^{(*)} \rightarrow V_2H_2^{(*)}$.

On the other hand, VO must at least partly anneal through $VO + H \rightarrow VOH$ due to the measured level attributed to VOH. VOH is expected to anneal through the creation of VOH_2. However, some of VO might also anneal out by $VO + H_2^{(*)} \rightarrow VOH_2$, which is not electrically active, since [VOH] only reaches about 30% of the initial [VO]. In addition, some VOH will dissociate as $VOH \rightarrow VO + H$, and some of the released VO can be lost to VO_2. Then H can reform VOH by reaction with VO, effectively reducing [VO], increasing [VO_2] and leaving [VOH] unchanged. This is a possibility for hydrogen–assisted annealing of VO through VOH to VO_2.

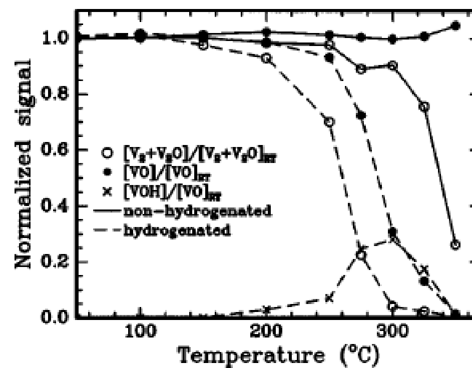

Figure 3.13: Normalized DLTS amplitudes versus annealing temperature. From reference [31].

3.3.4 The identification of V_2O

Most of the results presented later in this thesis are heavily dependent on a correct identification of all the defect species which are involved in the overall reactions. Because of this, a summary of the discussion regarding the identification of the electrical properties of V_2O is necessary.

Over the past 4 decades many of the defects in irradiated silicon have been identified and assigned their correct properties and structure. Important defects such as VO, VP and V_2 have had their structure identified and the activation energy and capture cross section has been measured in references [11, 12, 44] and the corresponding peaks in DLTS spectra have therefore been possible to assign to the correct defects.

However, vacancy-oxygen complexes of higher order in V than VO, such as V_2O, have proved difficult to assign to any particular DLTS peak. In particular the assignment of the correct DLTS peak to V_2O generated some controversy when both Pintilie et al. in references [35,36] and almost simultaneously Monakhov et al. in references [2,30] claimed to have identified V_2O as two different DLTS peaks, labeled the I and X defect, respectively.

[4]Hydrogen dimers have been suggested to exist in two forms, regular molecular hydrogen and a so–called H_2^* complex [17]. $H_2^{(*)}$ is meant to be interpreted as either H_2or H_2^*.

As explained in section 3.3.2 the generation of V_2O through $V + VO \rightarrow V_2O$ is expected to be suppressed in materials with large $[O_i]$ and it should follow second order generation kinetics. I displays these properties. Theoretical calculations further predict that V_2O can be in four different charge states, which are positive, neutral, singly and doubly negative [34]. This would give rise to three peaks in a spectrum from a space-charge spectroscopy measurement, like DLTS or TSC, namely $V_2O^{0/+}$, $V_2O^{-/0}$ and $V_2O^{=/-}$.

At the time of the publication of reference [2] all the required four charge states had been observed for X whereas the doubly-negative acceptor charge state had not been observed for I. In addition, Alfieri and Monakhov et al. measured the annealing rate of V_2 into X to be proportional to $[O_i]$ and that the transformation of V_2 into X was close to one-to-one. This, and the realization that V_2O has similar electrical properties as V_2, lead these authors to conclude that X is V_2O. It has also been very tentatively suggested that a possible candidate for the I defect is V_3.

In this work **X is assumed to be correctly identified as V_2O** based on the above discussion. It should be pointed out that despite the controversy over the electrical properties of V_2O it seems likely that the I defect is a main factor involved in the type inversion of silicon radiation detectors.

3.3.5 Comparison of MCz- and DOFZ-Si

Mads Mikelsen et al. studied the annealing of defects in magnetic Czochralski (MCz) and diffusion oxygenated float zone (DOFZ) silicon in [24, 25]. The samples that were studied in both cases had properties as described in table 3.4. Neither materials had been subjected to hydrogenation, so the concentration of hydrogen is expected to be similar. Figure 3.14 showns a survey made by the CERN RD48 collaboration of different substrate and epitaxial materials [9]. It can be observed that the concentration for oxygen in table 3.4 is in good agreement with the RD48 survey, but a lower concentration by a factor of 10 is reported in the survey for [C] in DOFZ. MCz was not covered in the survey, since this material has only become available recently.

	Concentration (cm^{-3})		
Material	Doping	Carbon	Oxygen
MCz-Si	5.5×10^{12}	$\leq 10^{16}$	$(5 - 10) \times 10^{17}$
DOFZ-Si	5.0×10^{12}	$(2 - 4) \times 10^{16}$	$(2 - 3) \times 10^{17}$

Table 3.4: Properties of the samples used in references [24, 25].

In the isochronal annealing studies from 50 – 400 °C in [25] it was found that the defects in the two materials had similar stabilities up to about 250 °C, the only differences being a minor level at 162 K (position in the 640 ms lock–in rate window) in as–irradiated MCz–Si.

For the annealing at 250 – 400 °C some interesting differences between the materials appear, as can be seen in figure 3.15 adapted from reference [25]. $V_2O^{-/0}$ is referred to as E1, $V_2O^{=/-}$ is E2, VO is E3 and VOH is E4 in reference [25]. The differences are listed in table 3.5, and the major differences can be summarised as follows:

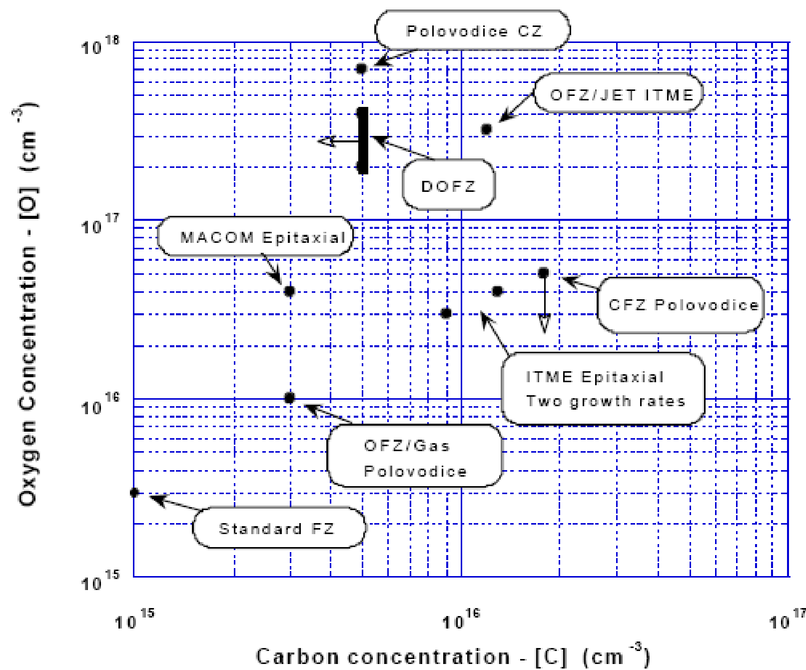

Figure 3.14: A survey made by the RD48 collaboration [9] of the concentrations of oxygen and carbon in different types of substrates and epitaxial layers. DOFZ is said to have [O] of about $(2-4) \times 10^{17}$ cm^{-3} and [C] of 5×10^{15} cm^{-3}. MCz–Si substrates are not included in the survey.

1. VO and V_2O anneal out at a faster rate in DOFZ than in MCz, perhaps through interaction with atomic hydrogen as indicated by the formation of VOH.
2. VOH appears in DOFZ, but not in MCz. This indicates a larger concentration of H in DOFZ than in MCz, likely due to differences in detector processing.

However, there are some apparent contradictions between the investigations of the annealing of VO and V_2 in DOFZ versus MCz in reference [25] and in the later and more thorough study in reference [24]. These contradictions consist mainly in that

1. VOH appears only in DOFZ in both cases. Reportedly, it plays only a small role in the annealing of VO and V_2O in the DOFZ samples used in reference [24], while it is regarded as significant in the DOFZ material used in reference [25] even though the material properties were both as given in table 3.4.
   - In reference [28, p. 59] it is argued that this is likely due to a higher concentration of hydrogen in the samples which were used in [25] because of differences in the processing conditions, such as HF etching time.
2. In MCz a slight decrease in [VO] is observed in reference [25], whereas a slight increase is observed in reference [24] for the early stages of the isothermal annealing, even though the properties of the MCz materials that were used in both studies were reported to have the properties given in table 3.4.

Temp. [°C]	**DOFZ**	**MCz**
250-300	– V_2 transforms into V_2O.	– — ॥ —
	– The peak at 160 K becomes detectable.	– — ॥ —
325	– The peak at 170 K becomes detectable.	– No peak at 170 K.
	– $[V_2O^{=/-}]$ and $[V_2O^{-/0}]$ decrease slightly.	– $[V_2O^{=/-}]$ and $[V_2O^{-/0}]$ decrease slightly.
350	– $V_2O^{=/-}$ completely gone.	– Both $[V_2O^{=/-}]$ and $[V_2O^{-/0}]$ reduced by about 50%.
	– VOH grows very quickly with roughly $[\mathrm{VOH}]_{350°C} \approx [V_2O^{=/-}]_{325°C}$.	– E(170 K) becomes detectable, but no VOH.
	– A fraction of another peak at the position of $V_2O^{-/0}$ remains.	– The peak at the position of $V_2O^{-/0}$ is somewhat larger than that at $V_2O^{=/-}$.
	– [VO] decreases slightly.	– [VO] increases slightly.
375	– [VO] decreases about twice as much as in MCz relatively speaking.	– [VO] decreases.
	– VOH is stable.	– $V_2O^{=/-}$ completely gone.
400	– All defects virtually gone.	– Similar to DOFZ.

Table 3.5: Summary of defect evolution in DOFZ–Si and MCz–Si. All peak temperature positions are given in the 640 ms lock-in rate window.

- In reference [28, p. 59] this is attributed to a difference in [O_i] in the MCz samples used in the two articles. This could be because even though they came from the same wafer, they were cut from different locations on that wafer. Thus, [O_i] was expected to have been non–uniform across the wafer, which reportedly is a problem that has been frequently discussed in the CERN RD50 collaboration.

  In fact, simulations for [VO] in reference [24] showed that a change in [O_i] from 7×10^{17} cm^{-3} to about 4×10^{17} cm^{-3} is sufficient to make an initial decrease of [VO] become an increase.

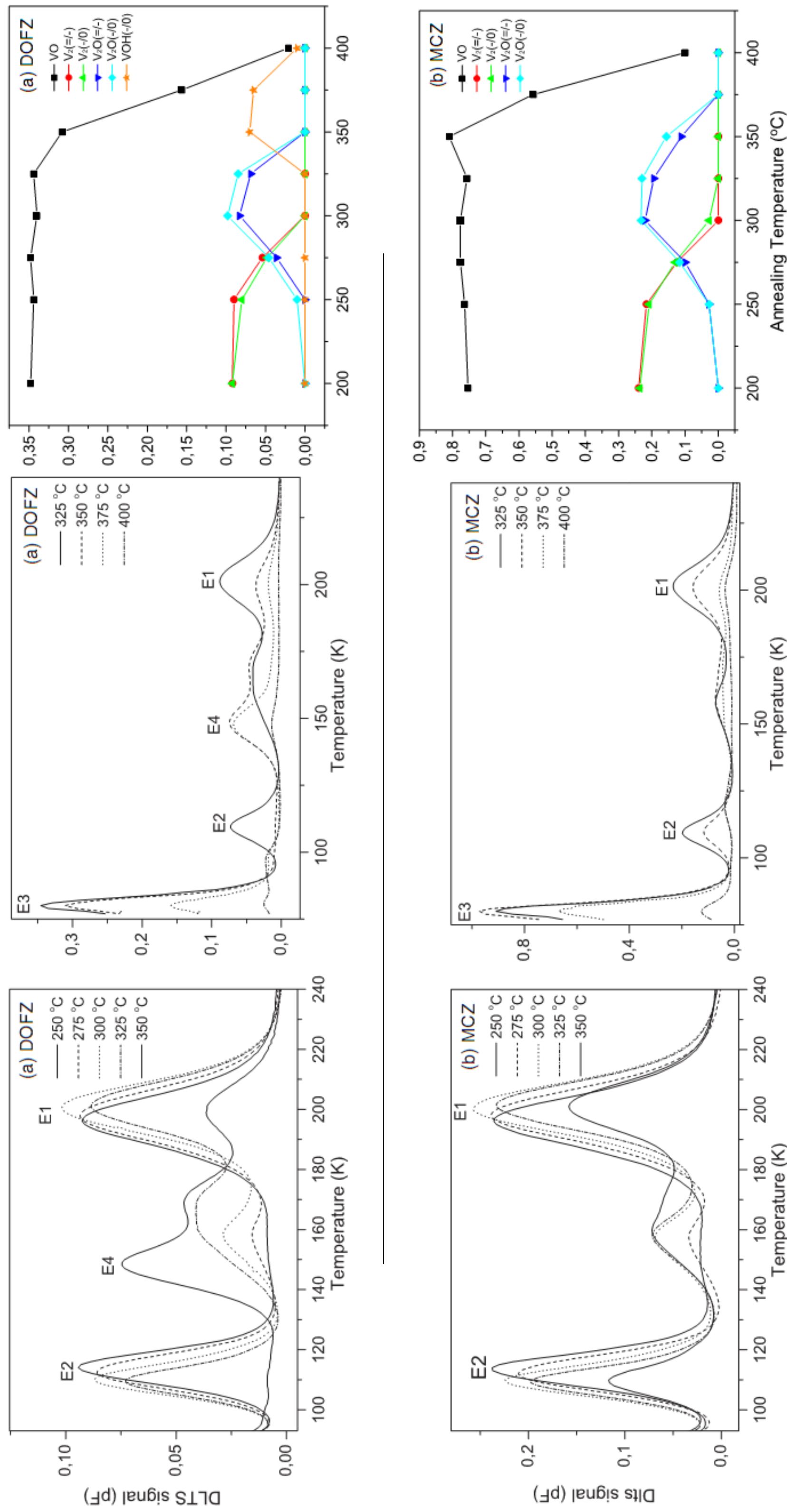

Figure 3.15: Isochronal annealing between 250 - 400 °C of **(a)** DOFZ-Si and **(b)** MCz-Si.

Chapter 4

Experimental techniques and instrumentation

> "Don't touch that please, your primitive intellect wouldn't understand things with alloys and compositions and things with... molecular structures."
>
> — *Ash (Bruce Campbell)*

4.1 Sample properties, structure and irradiation

All the samples used in this thesis were cut from a wafer with a n^+ Cz substrate with an epitaxial n^-–layer grown by ITME[1] and later processed by Sintef Minalab into pads of $p^+ - n^- - n^+$–diodes. The p^+–layer was made by ion impantation of boron. The thickness of the epitaxial layer is 59μm $\pm$ 8% and the resistivity is $\rho = 46$ Ωcm $\pm$ 15%. This resistivity translates into an effective doping concentration of $N_{eff} = (1 \pm 0.18) \times 10^{14}$ cm^{-3} by applying

$$\rho = \frac{1}{q\mu n} \approx \frac{1}{q\mu N_{eff}}$$

μ is assumed to be approximately the mobility of electrons in intrinsic silicon, $\mu = 1350$ cm^2/Vs, due to the low doping [38, p. 99]. By assuming a uniform effective doping concentration in the epitaxial layer this was measured by CV to be

$$N_{eff} \approx 7.7 \times 10^{13} \text{ cm}^{-3}$$

which is ~25% below the nominal value. The measured value was used in all the analysis in this thesis.

The wafers were cut into rectangular sections of about 1.5×1.5 mm^2 in size. The processing included no intentional oxygenation, hydrogenation or the intentional introduction of any other impurity, but oxidation necessarily introduces oxygen from the surface. A picture of the processed and diced wafer is given in figure 4.1.

The use of silver paste[2] was only rarely necessary since the samples have bottom and top

[1] Institute of Electronic Materials Technology, Warszaw, Poland.

[2] A liquid solution of silver and acetone. Commonly used for making or improving ohmic contacts.

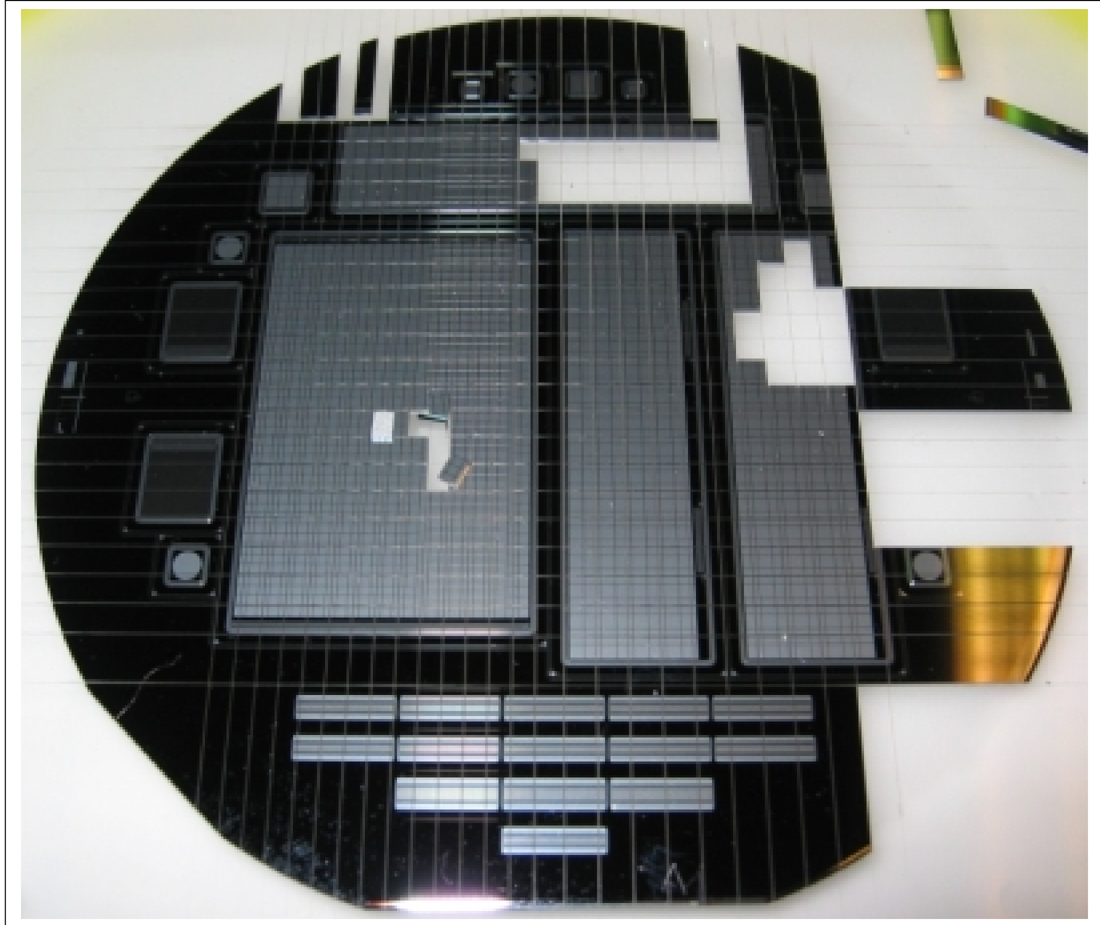

Figure 4.1: A picture of the processed and diced wafer. The n^-–layer has been phosphorous doped to a nominal concentration of 1×10^{14} cm^{-3}. The diode samples can be seen as small $(1.5 \text{ mm})^2$ squares located in the areas that are covered with aluminium (grey). The rest of the structures in the wafer are irrelevant to this thesis. The primary and secondary flat indicate that the substrate is (111) n–type, see figure 4.2.

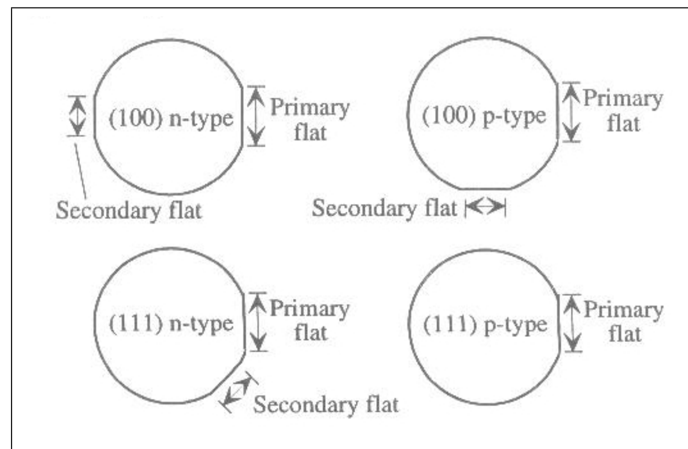

Figure 4.2: An illustration of the wafer flats used to identify the properties of the substrate material, whether it's n– or p–type and the crystal direction. Figure from Senturia [37].

aluminium contacts. A list of the samples and the measurements performed on them is given in table 4.1 below and a schematic of a sample is shown in figure 4.3.

The samples have been irradiated with 6 MeV electrons at room temperature (RT) to a dose of 10^{14} cm^{-2}. The irradiation time was on the order of 10^3 s, and the irradiation was performed at the Alfvén laboratory at KTH, Stockholm.

Sample name	Dose (cm^{-2})	Storage time and temp. before meas.	Experiment, parameters
W1_12	1E14	3 months, -18°C	Isochronal, 0 – 450°C
W1_15	1E14	3 months, -18°C	Isothermal, 325°C
W1_18	1E14	3 months, -18°C	Isothermal, 338°C, and depth profiling
W1_16	1E14	3 months, -18°C	Isothermal, 350°C
W1_17	1E14	3 months, -18°C	Isothermal, 360°C

Table 4.1: A list of the samples and the measurements that were performed on them for this work.

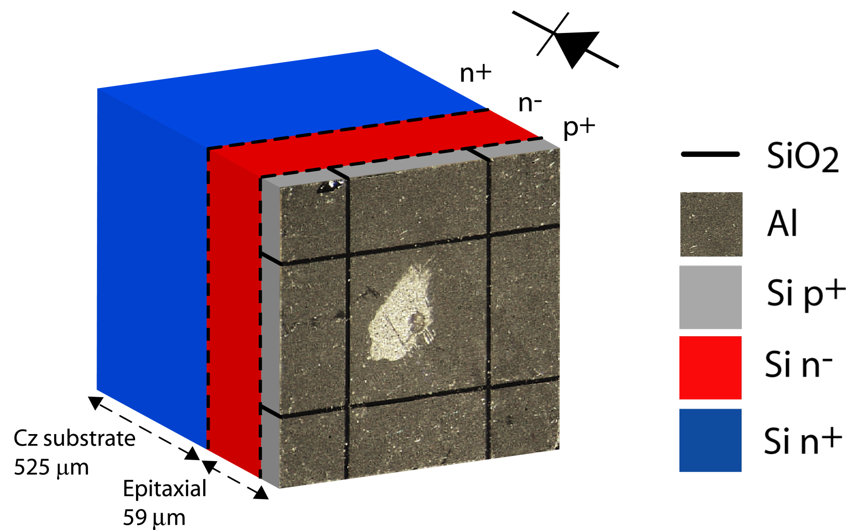

Figure 4.3: A visualization of the samples used in this work where the front side is a microscope photograph. The front contact is the middle square, with a patch of silver paste in this case, which is electrically isolated by dark ditches of SiO_2. The thickness of the epitaxial layer is 59μm $\pm$ 8% and the resistivity is $\rho = 46$ Ωcm $\pm$ 15% according to the producer ITME, roughly corresponding to the measured effective doping of 7.7×10^{13} cm^{-3}. The dimensions are not to scale.

4.2 Experimental techniques

The theory behind the experimental techniques and the extraction of important parameters will be addressed in this section. DLTS is the most thoroughly presented method, since most of the results presented in the following chapter was obtained by this method.

The current–voltage (IV) and capacitance–voltage (CV) techniques will also be briefly explained.

4.2.1 Current-voltage (IV)

IV was used in the experimental work only to make sure that the contact and the general performance of a sample was good. In other words the leakage current, I_s, was measured to see if it increases significantly after annealing from the "as irradiated"–condition. Whenever I_s changed significantly, the reason was assumed to be a bad contact or contamination by an impurity during annealing. In either case several measurements were then made, also using Ag paste, until good contact was established if possible. Otherwise, the sample was simply discarded and the annealing experiment was repeated from the beginning on a similar, as–irradiated sample.

4.2.2 Capacitance-voltage (CV)

As described in equation (3.14), the capacitance of a pn–junction is given by

$$C = \frac{\epsilon A}{W} = \epsilon A \Big[\frac{q}{2\epsilon(V_{bi} - V)} \big(\frac{1}{N_a} - \frac{1}{N_d}\big)\Big] \tag{4.1}$$

This means that a measurement of the capacitance as a function of the reverse bias voltage can be used to extract several properties of the junction.

4.2.2.1 Doping concentration and built-in voltage

After squaring (3.14) and rearranging, the above equation becomes

$$\frac{1}{C^2} = \frac{2(V_{bi} - V)}{q\epsilon A^2} \frac{N_d + N_a}{N_d N_a} \approx \frac{2(V_{bi} - V)}{q\epsilon A^2 N_d} \tag{4.2}$$

where the last approximation is valid when $N_d \gg N_a$, that is for a p^+–n^-–diode. This means that for a uniformly doped junction, when N_d is constant over the junction width, $1/C^2$ should be linear as a function of $V = V_{rb}$. A linear least–squares fit would give

$$\frac{1}{C^2} = aV_{rb} + b = -\frac{2}{q\epsilon A^2 N_d} V_{rb} + \frac{2V_{bi}}{q\epsilon A^2 N_d} \tag{4.3}$$

Thus, N_d is found from the slope and V_{bi} is found by extrapolating to $1/C^2 = 0$ where the straight line intersects the V_{rb}–axis in $V_{rb} = V_{bi}$.

4.2.2.2 Depletion voltage and maximum junction width

In the case of a p^+–n^-–n^+–diode, where the active n^-–layer is sandwiched between two more highly doped layers, a large enough reverse bias can result in a situation where

the entire low–doped side of the diode becomes depleted. This reverse bias is called the depletion, or punch–through, voltage and the diode is said to be fully depleted. There is an electric field going straight from the p^+–side to the n^+–side with no free carriers within the entire n^-–region. When the diode is fully depleted it will conduct very little current. See figure 4.3 for a layout of the p^+–n^-–n^+–diodes which were investigated in this work.

If the reverse bias is increased further when the n^-–region is fully depleted, then the depletion region extends into the n^+–region which is much heavier doped than the n^-–region. Thus, the change in capacitance per voltage, or in other words the slope of capacitance vs. voltage, will be much smaller here. This can readily be seen from equation (4.2) when $N_{d,n^-} \ll N_{d,n^+}$. The change in the slope of C vs. V_{rb} can therefore be used to determine the depletion voltage, as shown in figure 4.4.

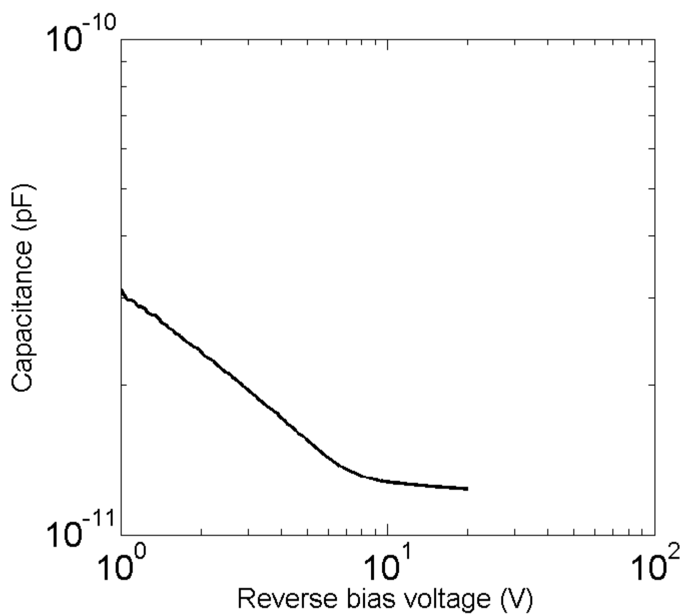

Figure 4.4: Capacitance as a function of reverse bias in a loglog plot. The depletion voltage is at the bend in the capacitance, which is at $V_{rb} \approx 8$ V in this example.

Full depletion is the normal operating mode for a radiation detector. This is because the depletion layer must be as large as possible to enhance the sensitivity (largest possible production of EHP's), and as large charge collection efficiency, or as low recombination rate in the depletion region, as possible. Care must be taken to keep the voltage between the depletion and the breakdown voltage. A smaller voltage will give lower sensitivity and a larger voltage will lead to breakdown.

However, irradiation induced acceptor defects with an energy close to mid band gap can decrease the effective doping concentration and thus decrease the depletion voltage. For very large radiation doses the donor concentration, N_d, in the n^-–region can become smaller than the acceptor concentration, N_a. This is called *type inversion* since the n^-–layer has become a p^-–layer and the effective doping concentration, $N_{eff} = |N_d - N_a|$, changes to acceptor–like. After type inversion the depletion voltage starts increasing with

the radiation dose, and eventually it can become difficult to deplete the detector volume in the p^-–region (n^- before inversion).

4.2.3 Deep Level Transient Spectroscopy (DLTS)

4.2.3.1 The principle of DLTS

The principle behind constant–voltage deep level transient spectroscopy (DLTS) is to charge the traps by pulsing the reverse bias between a large and a smaller value. Starting from the large reverse bias, the junction is in equilibrium. Then the traps are charged by applying a pulse voltage, or rather by decreasing the reverse bias, for a short amount of time. When the voltage is returned to the large reverse bias, the change in the capacitance as the traps emit their trapped carriers is measured.

The starting equilibrium situation is depicted in figure 4.5(a). The charging of the traps by applying a short, close to zero pulse voltage is shown in figure 4.5(b), and the emission of trapped charge carriers after the return to a reverse bias is shown in figure 4.5(c).

This procedure is repeated several times at each temperature in a temperature scan. The capacitance transient in response to the voltage pulsing sequence are measured at each temperature as shown in figure 4.6. The temperature interval used in this thesis is from 77 – 300 K, which is from liquid nitrogen (LN_2) to room temperature.

4.2.3.2 Equilibrium

Figure 4.5(a) shows that in the region $0 < x < W_r - \lambda$ the trap level is closer to the conduction band than E_F, $E_t(x) > E_{F,n}$. Therefore $e_n > c_n$, according to equation (3.24). Also, in the depletion region $n \approx p \approx 0$ because the charge carriers are swept out of the depletion region by ε_i. Then $c_n \propto n \approx 0$. Thus, in this region the level will be unoccupied by electrons at reverse bias in equilibrium.

However, at the far edge of the n–region there will be a transition length, $W_r - \lambda < x < W_r$, where $E_{F,n} > E_t$. This is still inside the region which is defined to be the depletion region because of the band bending. The traps at this level are in the so–called λ-region, and they will not emit their trapped carriers during the emission phase. Therefore, the concentration in the depletion region deduced from the measurement becomes too small if this effect is not considered, since these traps do not respond to the voltage pulse.

4.2.3.3 Charging

A pulse voltage which is close to zero is applied over the junction in figure 4.5(b). The traps in the region $0 < x < W_p - \lambda$ will never be filled since $E_t(x) > E_{F,n}$. The duration of the pulse voltage has to be long enough for all the traps to capture electrons, so the required pulse width depends on the capture cross section of the level. The larger σ_{na} for a level, the shorter the pulse width is required to fill all the traps. In this thesis a filling pulse duration of 50 ms is assumed to be sufficient to saturate the occupation of all traps.

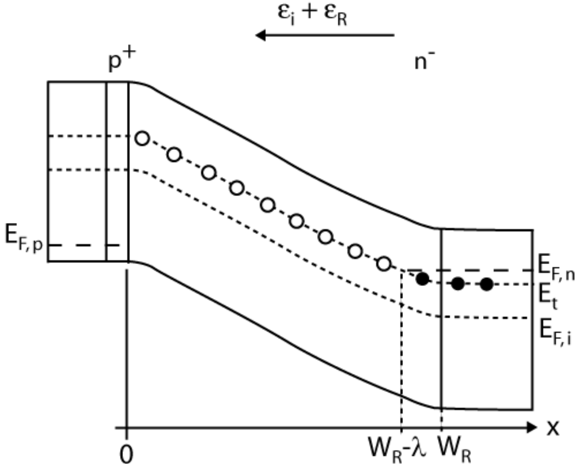

(a) Equilibrium at reverse bias $-V_r$.

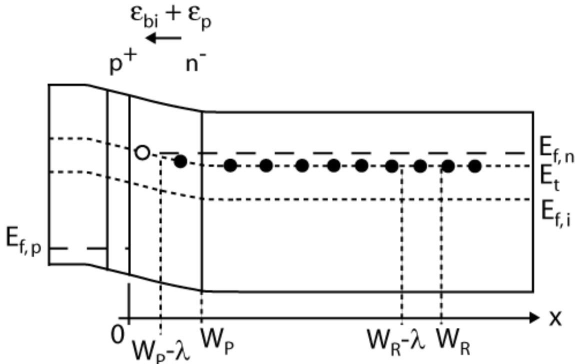

(b) Charging pulse with bias $-V_p = -V_r + \Delta V_p$.

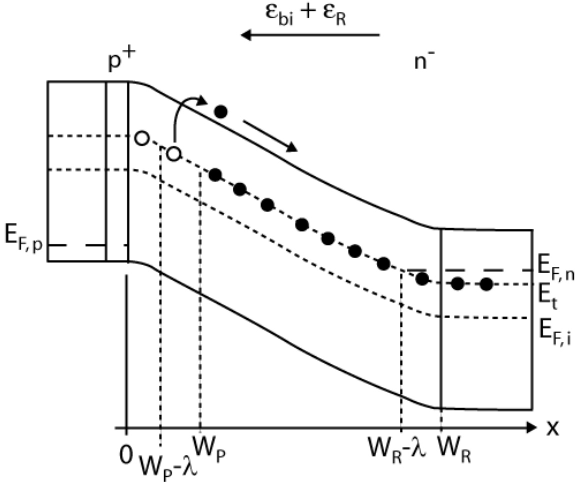

(c) Emission from traps at bias $-V_r$.

Figure 4.5: **(a)** Equilibrium at reverse bias $-V_r$. **(b)** Charging pulse with bias $-V_p = -V_r + \Delta V_p$. **(c)** Emission from traps at bias $-V_r$.

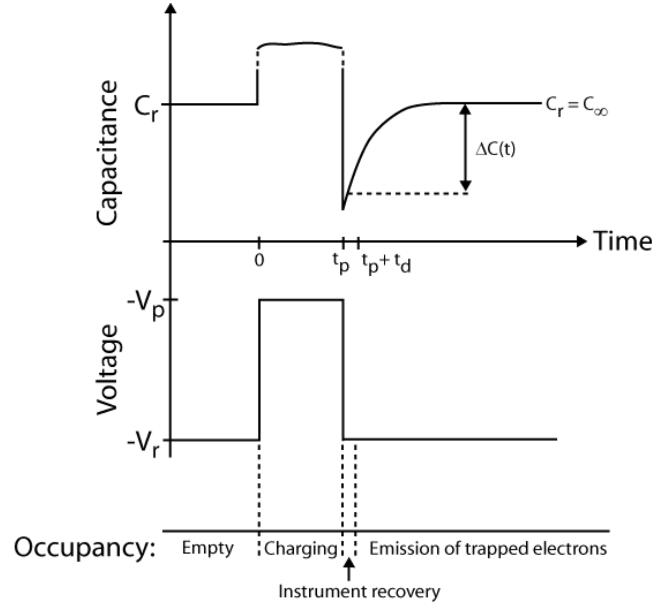

Figure 4.6: The capacitance as a function of time when a voltage pulse is applied to fill the traps in the depletion region.

4.2.3.4 Emission

At $t = 0$ immediately after changing from $-V_p$ to $-V_r$, all the traps are occupied by electrons, as shown in figure 4.5(c). However, now $E_t(x) > E_{F,n}$, except in the λ–region where the traps will always be occupied. Therefore the traps will emit their trapped electrons. Possible recapture of electrons is neglected.

There is a surplus of positively ionized donor atoms when the traps emit their trapped electrons. The depletion region contracts to eliminate the surplus positive space charge by moving the right hand side of the n–region towards the p–region and leaving behind neutral donor atoms which are now outside of the depletion region. The depletion region contracts until equilibrium and charge neutrality is re–established. In a p^+–n^-–junction it is a good approximation to assume $W_d \approx x_n$ since $x_n \gg x_p$ according to equation (3.13). Then W_d has a time dependence like

$$W_d(t) = W_{d,\infty} - \Delta W_d(t)$$

When the depletion width decreases, the capacitance increases since they are inverseley proportional to each other according to equation (3.14). The increase in capacitance is measured as a capacitance transient,

$$C(t) = C_\infty + \Delta C(t)$$

as displayed in figure 4.6.

4.2.3.5 Rectangular transient charge model

As can be seen in figure 4.5(a) – 4.5(c) there are three regions of the junction in which the space charge density behaves differently during charging and emission. These differences are summarized in table 4.2. The assumption that the transitions between each of these three regions is abrupt is called the rectangular transient charge model in Blood & Orton [5].

Region	Space charge density	Description
$0 < x < W_p - \lambda$	N_d^+	The traps in this region are always unoccupied, so $n_t(t) = 0$.
$W_p - \lambda < x < W_r - \lambda$	$N_d^+(t) - n(t)$	The traps here are filled during charging pulse and emptied by electron emission when the voltage is changed to reverse bias, so $n_t(t)$ varies with t.
$W_r - \lambda < x < W_r$	$N_d^+ - N_t$	In this region the traps are always occupied, so $n_t(t) = N_t$.

Table 4.2: The three regions with different behaviour define the basis for the so–called rectangular transient charge model [6].

4.2.3.6 The λ–length and the Debye tail

The total band bending V due to an applied reverse bias, $V = V_{bi} + V_r$, is defined to be the positive quantity

$$qV = E_c(-\infty) - E_c(+\infty) \approx E_c(0) - E_c(x_d)$$

in n–type materials. The depletion approximation of no electric field outside the depletion region is assumed. The potential, $\psi(x)$, across the depletion region is defined as in figure 4.7(b), or in other words

$$-q\psi(x) = E_c(x) - E_c(x_d) \qquad \begin{array}{l} \psi(0) = -V \\ \psi(x_d) = 0 \end{array} \tag{4.4}$$

where the negative sign for $\psi(x)$ is because the electron potential decreases for increasing x. The concentration of electrons in the conduction band outside the depletion region is

$$n_0 = n(x_d) = N_c \exp\left(\frac{E_c(x_d) - E_F(x_d)}{kT}\right)$$

For $x < x_d$ this becomes

$$n(x) = N_c \exp\left(-\frac{E_c(x) - E_F(x_d)}{kT}\right) = n_0 \exp\left(\frac{q\psi(x)}{kT}\right)$$

when inserting for $E_c(x)$ from equation (4.4). This is called **the Debye tail of free electrons** in the depletion region and it is shown in figure 4.7(a). Ignoring any defects in the depletion region except ionized donor atoms, the space charge density is

$\rho(x) = N_d - n(x)$. When inserted into the Poisson equation this gives for $\psi(x)$

$$\frac{d^2\psi(x)}{dx^2} = -\frac{\rho(x)}{\epsilon_{Si}\epsilon_0} = -\frac{q}{\epsilon_{Si}\epsilon_0}\left[N_d - n_0 \exp\left(\frac{q\psi(x)}{kT}\right)\right]$$
$$\approx -\frac{qN_d}{\epsilon_{Si}\epsilon_0} \tag{4.5}$$

where the last approximation is valid when $-\psi(x) \gg kT/q$. This means that the free charge carriers in the Debye tail can be neglected when this approximation is valid.

Integrated once from x_d to x this gives the electric field $\varepsilon(x) = -d\psi(x)/dx$. When integrated twice with the same limits the potential is

$$-\psi(x) = \frac{qN_d}{2\epsilon_{Si}\epsilon_0}\left(x_d - x\right)^2$$

Further, $x_\lambda = x_d - \lambda$ is defined to be where the band bending is exactly $E_F(x_d) - E_t(x_d)$, so

$$-q\psi(x_\lambda) = E_F(x_\lambda) - E_t(x_d)$$

λ can now be calculated by inserting $\psi(x_\lambda)$ into equation (4.4) at $x = x_\lambda$.

$$\lambda = x_d - x_\lambda = \left[\frac{2\epsilon_{Si}\epsilon_0}{e^2N_d}\left(E_F - E_t(x_d)\right)\right]^{1/2}$$

By using equation (3.1) this can be expressed through the measured quantity $E_c(x_d) - E_t(x_d)$ as

$$\lambda = \left[\frac{2\epsilon_{Si}\epsilon_0}{e^2N_d}\left\{E_c - E_t - kT\ln\left(\frac{N_c}{n}\right)\right\}\right]^{1/2} \tag{4.6}$$

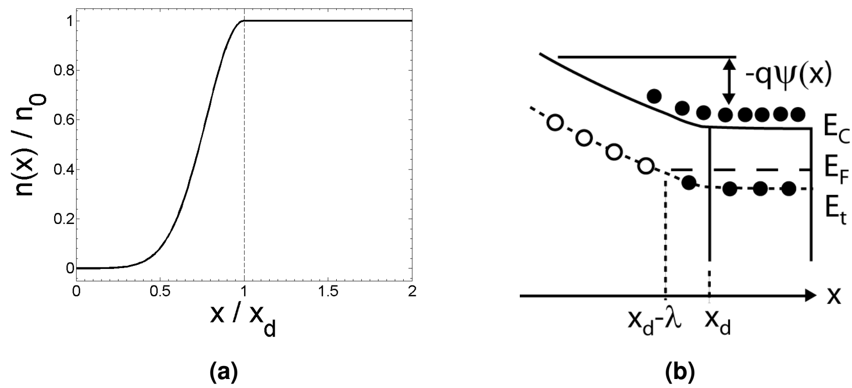

Figure 4.7: A visualization of the electron density **(a)** and the Debye tail in a band diagram with free electrons in the conduction band from the depletion edge and into the depletion region **(b)**. Electron capture happens here because the concentration of free electrons in the conduction band is not zero within the Debye tail.

4.2.3.7 Capacitance transients

The space charge density when there is only one donor–like level participating in capture and emission processes is

$$\rho(x,t) = q\left[N^+_{eff} + (N_t - n_t(t))\right] \qquad \begin{array}{l} n_t(t=0) = N_t \\ n_t(t=\infty) = 0 \end{array}$$

N^+_{eff} takes into account the effective doping $N_d - N_a$ and any other levels that are not emitting electrons, but which could be in a non–neutral charge state.

A time–dependent space charge density, $\rho(x,t)$, will result in a time–dependency of the electric field, $\varepsilon(x,t)$, and of the total potential over the junction, $V = V(t)$. In solving the Poisson equation for the potential as a function of position one must then assume a time–dependency also, $\psi = \psi(x,t)$, so

$$\frac{\partial^2\psi}{\partial x^2} = -\frac{\rho(x,t)}{\epsilon_{Si}\epsilon_0}$$

This can be integrated twice to find the voltage across the junction, as shown in detail in appendix B. The total voltage across the junction is

$$V(t) = \psi(\infty,t) - \psi(-\infty,t) = \frac{1}{\epsilon_{Si}\epsilon_0}\int_{-x_p}^{x_n} x\rho(x,t)dx \tag{4.7}$$

The integration limits can be chosen as $\int_0^{x_d}$ for a p^+-n^-junction since $x_n \gg x_p$.

Uniform distributions of N^+_{eff}, N_t and n_t are now assumed within each of the three different regions defined in table 4.2. This means that the contributions from these to the space charge density in each region will be

$$N^+(x) = \begin{cases} N^+ & \text{for} \quad 0 < x < x_d(t) \\ 0 & \text{else} \end{cases}$$

$$N_t(x) = \begin{cases} N_t & \text{for} \quad 0 < x < x_d(t) - \lambda \\ 0 & \text{else} \end{cases}$$

$$n_t(t,x) = \begin{cases} n_t(t) & \text{for} \quad x_p - \lambda < x < x_d(t) - \lambda \\ 0 & \text{else} \end{cases}$$

After dividing into these three regions and evaluating the integral over each region, the voltage is

$$V(t) = \frac{q}{2\epsilon_{Si}\epsilon_0}\left\{N^+x_d^2(t) + N_t(x_d(t)-\lambda)^2 - n_t(t)\left[(x_d(t)-\lambda)^2 - (x_p-\lambda)^2\right]\right\} \tag{4.8}$$

As the traps emit their electrons under reverse bias the voltage over the junction will try to change to accomodate the increase in space charge density. However, in a constant–voltage DLTS system the instrumentation will keep the reverse bias constant during the emission. Differentiating the above expression for $V(t)$ and equating to zero yields

$$\left[N^+ x_d + (N_t - n_t)(x_d - \lambda)\right] \frac{dx_d}{dt} = \frac{1}{2}\left[(x_d(t) - \lambda)^2 - (x_p(t) - \lambda)^2\right] \frac{dn_t}{dt} \tag{4.9}$$

In these calculations the assumption has been made that λ is only a function of temperature, it does not vary with voltage. In the so–called dilute limit the following is valid

$$N^+ \approx N_d \gg Na, N_t, n_t$$

Then the left hand side in the above equation greatly simplifies to

$$\begin{aligned} N_d x_d \frac{dx_d}{dt} &= \frac{1}{2}\left[(x_d(t) - \lambda)^2 - (x_p - \lambda)^2\right] \frac{dn_t}{dt} \\ \frac{dx_d/dt}{x_d} &= -\frac{dC_{rb}/dt}{C_{rb}} = \frac{1}{2} \frac{\left[(x_d(t) - \lambda)^2 - (x_p - \lambda)^2\right]}{x_d^2} \frac{1}{N_d} \frac{dn_t}{dt} \end{aligned} \tag{4.10}$$

$C_{rb}(t) = \epsilon_{Si}\epsilon_0 A / x_d(t)$ is used and the change in reverse bias capacitance during the emission process is assumed to be small so C_{rb} is approximately constant. Integrating from t to $t = \infty$, using equation (3.29) and that $n_t(\infty) = 0$ yields

$$\Delta C(T, t) = -\Delta C_0 e^{-e_n(T)t} \tag{4.11}$$

The maximum amplitude of the transient is

$$\Delta C_0 = \frac{1}{2} \frac{(x_d(t) - \lambda)^2 - (x_p - \lambda)^2}{x_d^2} \frac{N_t}{N_d} C_{rb} \tag{4.12}$$

Equation (4.11) is a good approximation when the depletion approximation can be assumed, when the trap concentration is within the dilute limit and for uniform N_d and N_t. If $x_d \gg \lambda, x_p$ then equation (4.12) further simplifies to

$$\Delta C_0 = \frac{N_t}{2N_d} C_{rb}$$

Otherwise the factor

$$\alpha \equiv \frac{(x_d - \lambda)^2 - (x_p - \lambda)^2}{x_d^2}$$

can be expressed in terms of the reverse and pulse bias capacitances as

$$\alpha(T) = \frac{(x_d - \lambda(T))^2 - (x_p - \lambda(T))^2}{x_d^2} = 1 - \left(\frac{C_{rb}}{C_p}\right)^2 - \frac{2C_{rb}}{\epsilon_{Si}\epsilon_0 A}\left(1 - \frac{C_{rb}}{C_p}\right)\lambda(T) \tag{4.13}$$

4.2.3.8 Weighting functions and rate windows

To make a spectrum from a collection of capacitance transients from a temperature scan they can be made into a DLTS signal, $S(T)$. The DLTS signal is defined as

$$S_i(T) = \frac{1}{n_i} \sum_{t_j=t_d}^{t_d+t_i} \Delta C(T, t_j) w(t_j) \tag{4.14}$$

where $w(t)$ is some specific weighting function, n_i is the number of measured capacitance values in the i'th so–called rate window, t_i is the time length of the rate window. If the sampling interval between each measured capacitance value in the transients is τ, then $t_i = n_i \tau$. $t_d = \tau/2$ is the time at the start of the summation, and also a delay time to allow the instrumentation to recover from a likely overload during the pulse bias, as shown in figure 4.8.

The length of the time window determines at which value of the emission rate, $e_n(T)$, the spectrum has a maximum value. This can be understood by noting that for peaks in the DLTS spectrum one must have

$$\frac{dS}{dT} = \left(\frac{dS}{d(e_n t_i)}\right)\left(\frac{d(e_n t_i)}{dT}\right) = 0$$

where the last factor is zero only for $T = 0$, which is irrelevant. Thus, DLTS peaks appear only at a certain value of $e_n t_i = e_n^{max} t_i$ for each rate window and for a certain weighting function. The peak temperature is a characteristic of the defect and the rate window. This is the motivation for the term "rate window", since only when the emission rate $e_n(T)$ approaches $e_n^{max}(T_{peak})$ is a peak created in the spectrum. The above equation for $e_n^{max} t_i$ must be solved by some numerical method, such as Newton–Raphson, since it is impossible to write the solution in closed form.

The lock–in and GS4 type weighting functions are used in this thesis. The lock–in weighting function for a discreet signal looks like

$$w(t) = \begin{cases} 1 & t_d + 2^{i-1}\tau < t_j \leq t_d + 2^i \tau \\ -1 & t_d < t_j \leq t_d + 2^{i-1}\tau \end{cases}$$

The GS4 weighting function is

$$w(t) = \begin{cases} 24 & t_d + 2^i \tau < t_j \leq t_d + 2^{i+1}\tau \\ -48 & t_d + 2^{i-1}\tau < t_j \leq t_d + 2^i \tau \\ 25 & t_d + 2^{i-2}\tau < t_j \leq t_d + 2^{i-1}\tau \\ -1 & t_d < t_j \leq t_d + 2^{i-2}\tau \end{cases}$$

The number of required measurements of $C(t)$ is $n_i = 2^i$ for lock–in and $n_i = 2^{i+1}$ for GS4. The rate windows used in this thesis of both lock–in and GS4 type are listed in table 4.3. Lock–in offers better signal–to–noise ratio (SNR) than GS4 by about a factor 10, but it is less selective than GS4, so lock–in peaks are broader. An important property of a

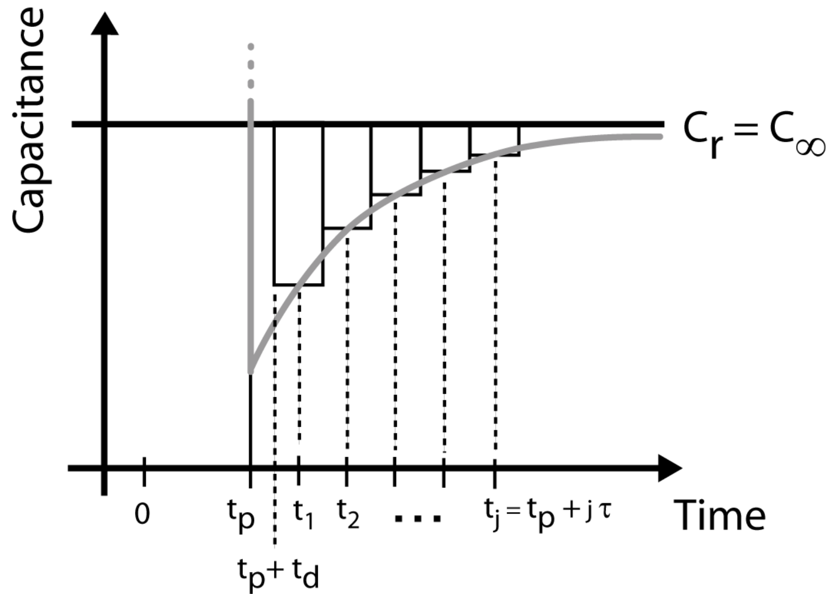

Figure 4.8: An illustration of the discrete capacitance transient, with sample interval τ and time delay $t_d = \tau/2$.

	Lock–in		GS4	
Window no. i	No. points	Length (ms)	No. points	Length (ms)
1	2	20	4	40
2	4	40	8	80
3	8	80	16	160
4	16	160	32	320
5	32	320	64	640
6	64	640	–	–

Table 4.3: The length and number of points in each lock–in and GS4 rate window. The 6th GS4 rate window was not used since each capacitance transient was recorded with 64 time points.

weighting function is that $\sum w = 0$, since this cancels out any constant contributions in the function on which it is applied.

$$\sum_j C(t_j)w(t_j) = \underbrace{\sum_j C_{rb}w(t_j)}_{=0} + \sum_j \Delta C(t_j)w(t_j)$$

A defect will create a peak at a certain temperature in a certain rate window in a DLTS spectrum, or in other words at a certain value of $e_n(T)t_i$. When e_n is known at the peak temperature for several different rate windows, then σ_{na} and ΔH can be deduced from an Arrhenius plot. An illustration of a DLTS spectrum in different rate windows is in figure 4.9.

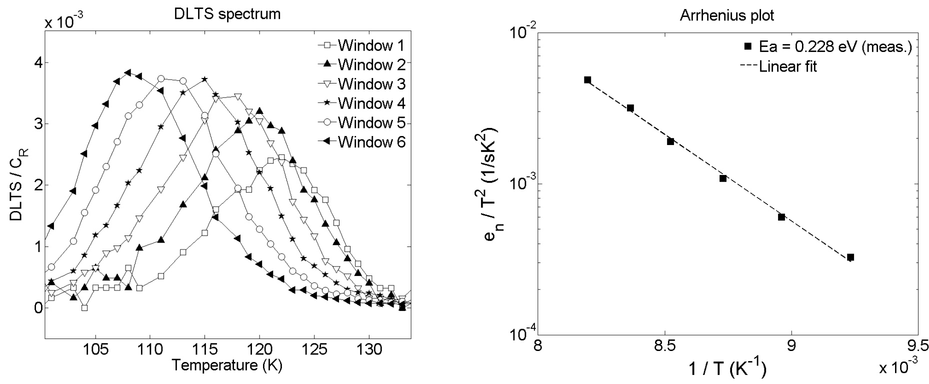

Figure 4.9: An illustration of a DLTS spectrum in different rate windows of the lock–in type. The rate windows **(a)** and the Arrhenius plot of this peak **(b)**. The y–axis in the plot of the DLTS spectrum is in units of S_i/C_{rb} since this is proportional to N_t. The peak in this example is due to the divacancy cluster, V_2.

4.2.3.9 Extraction of trap properties

If a temperature scan is done and a DLTS signal for several rate windows is built from the measured transients, then a set of values for $S_i(T_{peak})$ is produced for each measured DLTS peak. In this thesis the rate windows 1–6 have been used, so $i \in \{1, ..., 6\}$. The measured peak temperatures, $T_{peak} \in \{T_1, ..., T_i\}$, each correspond to a value of $e_n^{max}(T_{peak})$. According to equation (3.27), an Arrhenius plot of $\ln(e_n/T^2)$ vs. $1/T$ yields the straight line

$$\ln(e_n/T^2) = -\frac{\Delta H}{k}\frac{1}{T} + \ln(Q\sigma_{na}) \tag{4.15}$$

since

$$e_n = \sigma_{na} v_{th,n}(T) N_c(T) \exp(-\frac{\Delta H}{kT}) = \sigma_{na} Q T^2 \exp(-\frac{-\Delta H}{kT})$$

The factor Q contains all the factors in the emission rate that do not depend on T, so

$$QT^2 = v_{th,n}(T)N_c(T) = \sqrt{\frac{3kT}{m_n^*}} 2\left(\frac{2\pi m_n^* kT}{h^2}\right)^{3/2} = \underbrace{\sqrt{\frac{3k}{m_n^*}} 2\left(\frac{2\pi m_n^* k}{h^2}\right)^{3/2}}_{\equiv Q} T^2$$

ΔH is found from the slope of the Arrhenius plot of equation (4.15) and σ_{na} is found from the extrapolated intersection with the e_n/T^2-axis as $1/T \to 0$.

The concentration is found by rewriting equation (4.14) as

$$S_i(T) = \Delta C_0 \underbrace{\frac{1}{n_i} \sum_{t_d}^{t_d+t_i} e^{-e_n(T)t_j} w(t_j)}_{\equiv F_i = F_i(t_d, t_i, e_n(T))} \tag{4.16}$$

The term labeled as F_i has the same value for all peaks in a certain rate window since $e_n(T) = e_n^{max}(T_{peak})$ at a peak, and T_{peak} depends only on which rate window is used. This is just a numeric factor which is characteristic for each rate window of a certain weighting function. Therefore, at a DLTS peak the amplitude of the peak is simply proportional to the concentration of the defect. In other words

$$N_{t,i} = \frac{2N_d}{C_{rb}(T_{peak})\alpha(T_{peak})} \times \frac{S_{i,peak}(T_{peak})}{F_i} = \frac{N_{t,i}(\alpha = 1)}{\alpha} \tag{4.17}$$

To improve the statistical accuracy, the concentration is calculated from all the measured rate windows and taking the average.

$$N_t = \sum_i N_{t,i}$$

Since $0 < \alpha(T_{peak}) < 1$ it is clear that $N_t > N_t(\alpha = 1)$. The approximation

$$x_d \gg x_p, \lambda \quad \Rightarrow \quad \alpha = 1$$

thus yields a lower concentration than the actual concentration.

4.2.3.10 Synthesizing DLTS spectra

When a measured DLTS spectrum is very noisy or contains overlapping peaks, then it can be useful to create a synthetic DLTS spectrum from a set of N_t, σ_{na} and ΔH , and then try to make the best possible fit of the synthetic to the measured spectrum.

Equation (4.11) for the capacitance transient and (4.14) for the DLTS signal was derived for a situation where only one level is emitting electrons at a certain temperature. However, it can be shown that the same equations apply when several independent levels are emitting electrons at the same temperature. The total capacitance transient at that temperature is the sum of the individual capacitance transients from each emitting level.

With several emitting levels the space charge density becomes, assuming that N_d is much larger than any other concentration and that all species have uniform concentrations,

$$\rho(t) = q \left[N_d + \sum_i^{\text{all levels}} (N_{t,i} - n_{t,i}(t)) \right]$$

This can be used to calculate the capacitance transient by the same method as outlined before. The result is

$$\Delta C(T,t) = \frac{1}{2}\frac{(x_d(t)-\lambda)^2-(x_p(t)-\lambda)^2}{x_d^2}\frac{C_{rb}}{N_d}\sum_{\ell}^{\text{all levels}} N_{t,\ell}\, e^{-e_{n,\ell}(T)t} \tag{4.18}$$

which is simply the sum of the transient from each emitting level. Since summation is a linear operation, the total DLTS spectrum due to emission from all the levels is

$$S_i(T) = \frac{1}{n_i}\sum_{t_j=t_d}^{t_d+t_i}\Delta C(T,t_j)w(t_j) = \sum_{\ell}^{\text{all levels}} S_{i,\ell}(T) \tag{4.19}$$

In short, a synthetic DLTS spectrum for several peaks is simply a superposition of the DLTS spectra for each individual peak.

4.2.4 Profiling with DLTS

The theory for using DLTS for depth profiling of defects is outlined in for example Blood & Orton [6, ch. 12.4]. The starting point of the derivation is equations (4.12) for the capacitance transient amplitude and (3.13) for the depletion depth as a function of reverse bias voltage. Upon taking the differential and using the approximation that N_t is constant in a small depth interval δx_p, which corresponds to a small change in pulse voltage δV_p, then the approximate defect concentration at depth $x_p - \lambda$ is

$$N_t(x_p-\lambda) = -\left(\frac{x_p}{x_p-\lambda}\right)\frac{qN_d^2x_d^2}{C_{rb}\varepsilon}\frac{\delta(\Delta C_0)}{\delta V_p} \tag{4.20}$$

This assumes that N_d is constant throughout the investigated region. V_r is held constant while V_p is varied from $V_p = V_r$ to $V_p = V_{p,min}$. This means that the depletion region edge moves from the bulk and towards the surface.

At a peak in the DLTS spectrum S_i is proportional to ΔC_0, as can be seen in equation (4.16). Then the concentration can be written in terms of the differentiated DLTS signal as

$$N_t(x_p-\lambda) = -\left(\frac{x_p}{x_p-\lambda}\right)\frac{qN_d^2x_d^2}{C_{rb}\varepsilon F_i}\frac{\delta S_i}{\delta V_p} \tag{4.21}$$

This can further be written in terms of the measured capacitances, C_r and C_p, as

$$Nt(x_p-\lambda) = -\left(\frac{1}{1-\lambda C_p/\varepsilon A}\right)\frac{qA^2N_d^2}{C_r^3F_i}\frac{\delta S_i}{\delta V_p} \tag{4.22}$$

4.3 Annealing experiments

The concentration of defects is in general a function of position, time and temperature. For uniformly distributed defects the dependence on position disappears. Thus, the concentration of the defects can be measured while keeping the annealing time constant and increasing the temperature, or while keeping the temperature constant and increasing the annealing time. The former is isochronal and the latter isothermal annealing.

4.3.1 Isochronal annealing

Isochronal annealing gives an overview of the population of defects in the material which is investigated. "Iso" and "chronos" means equal time in latin, so as the name suggests the samples are annealed for a constant amount of time at different temperatures. Common choices of the annealing time is 15 – 20 min. In this work the annealing time was 20 min.

4.3.2 Isothermal annealing experiments

First order reactions, say a reaction between A and B where $[B] \gg [A]$ as in (3.41), follow

$$[A] = [A]_0 \exp(-c(T)t) = [A]_0 \exp\big\{ -c_0 \exp\left(-\frac{E_a}{kT}\right) t\big\} \tag{4.23}$$

c_0 is independent of temperature and E_a is the activation energy, which is the minimum energy required for the reaction.

If [A] is measured as a function of time for two or more isothermal measurement series, then the reaction rate $c(T)$ is the slope of the straight line

$$\ln[A] = \ln[A]_0 - c(T)t \tag{4.24}$$

This produces a set of reaction rates, $c(T)$, one for each measurement temperature. Since $c(T) = c_0 e^{-\frac{E_a}{kT}}$, then E_a/k is the slope and the pre–exponential factor, c_0, is the y–intersection of the straight line

$$\ln c(T) = -\frac{E_a}{kT} + \ln c_0 \tag{4.25}$$

in an Arrhenius plot of $\ln c(T)$ vs. $1/T$.

4.4 Instrumentation

In this section some of the experimental equipment that was used and the basic proceedures that were followed during the experimental work are presented.

4.4.1 The Asterix setup

Asterix is a setup for electrical measurements in the temperature range from LN_2 to above room temperature, 77–400 K. It was used for DLTS, CV and IV in this thesis. Figure 4.10 is a basic block diagram of the components in the setup and their interconnections. A central part of the setup is the capacitance meter HP4280A which measures CV profiles in "C-V" mode and capacitance transients with a sampling rate of 1 MHz in "C" mode.

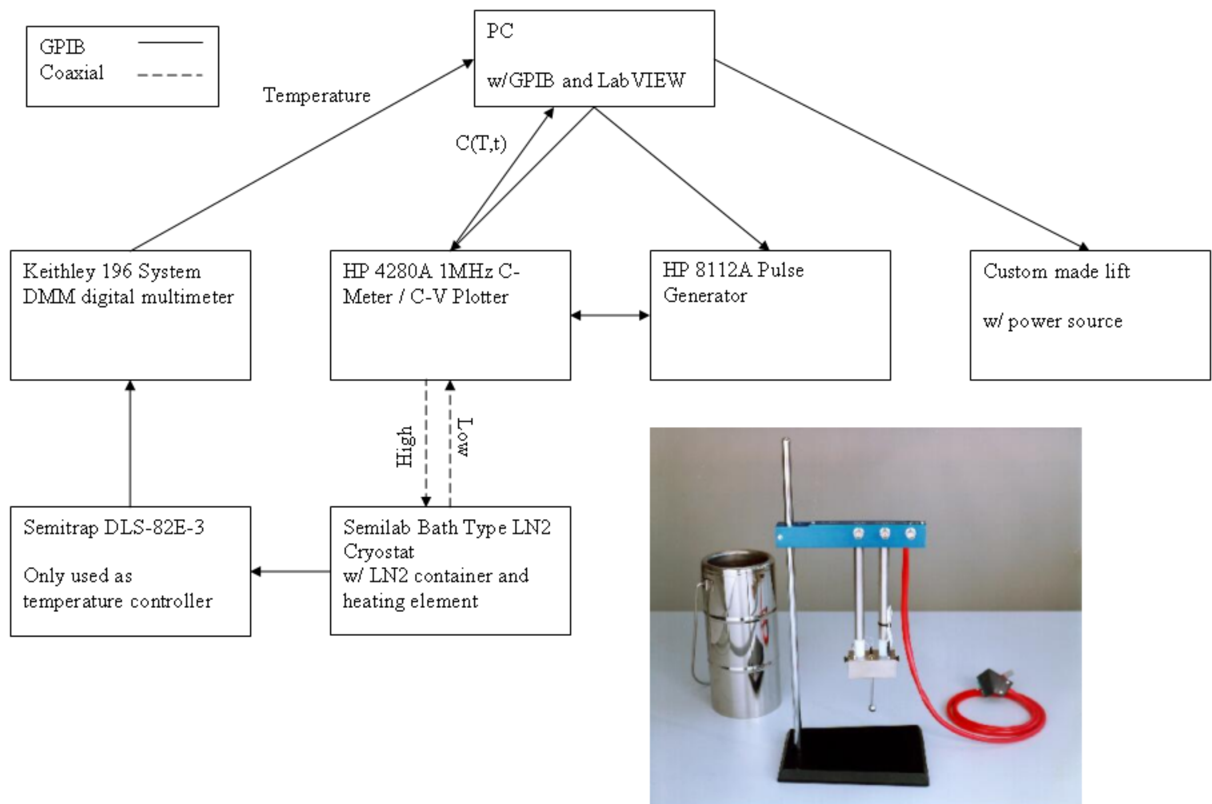

Figure 4.10: A block diagram of the DLTS setup. The bias, whether negative or positive, is applied through the wire which is labeled “High”, whereas “low” is always grounded.

4.4.2 Annealing equipment and procedures

In figure 4.11 is a photograph of the hotplate used for the annealing of samples up to 250 °C. An aluminium block was used as a thermal mass to improve the homogeneity of the temperature distribution across the plate. The sample was placed on a small piece of ceramic to avoid contamination from the possibly dirty thermal mass. The ceramic is copper patterned to allow annealing under bias, but this feature was not used in this work. The temperature of the hot plate was monitored by means of a liquid alcohol thermometer. The thermal resistor on top of the hot plate has a cavity for mounting the thermometer.

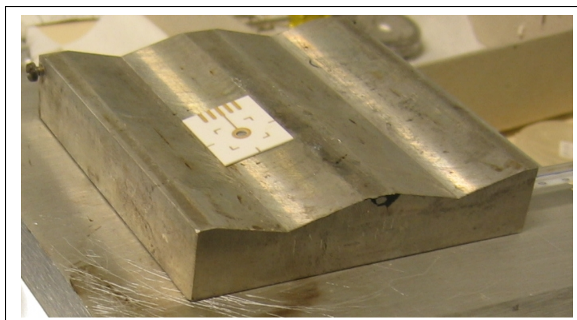

Figure 4.11: The hot plate used for annealing at temperatures up to 250 °C.

For higher temperatures than 250 °C the samples were annealed in a N_2 atmosphere in a fused silica tube furnace which is shown in figure 4.12. The sample was contained in a silica boat.

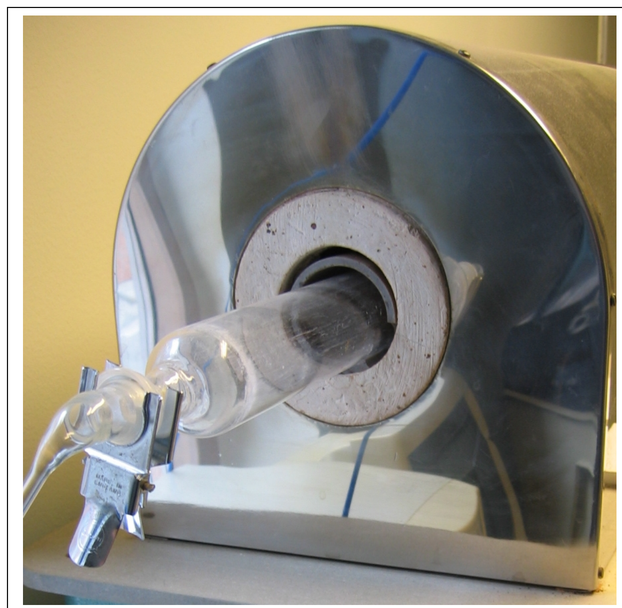

Figure 4.12: Fused silica tube furnace with N_2 supply. This was used for all annealing at higher temperatures than 250 °C.

Chapter 5

Results and discussion

"If we knew what we were doing, it would not be called research, would it?"

— *Albert Einstein*

Matlab is used for the data analysis of the measurements presented in this thesis. I have written all the Matlab–scripts and performed the analysis. The most relevant of these scripts are documented in appendix A.

5.1 Goals

As stated in the introduction, the purpose of this work have two different aspects, which are

Electrical characterization of the silicon epitaxial (EPI–Si) layer after electron irradiation, and a comparison of the behavior of the generated defects in EPI–Si with those in DOFZ– and MCz–Si.

To measure the properties of as yet unidentified defects, suggest identities and find possible relationships to impurities such as oxygen, carbon and hydrogen.

5.2 Impurity concentrations and distributions

5.2.1 Expected distributions of oxygen, carbon and hydrogen

The intuitively expected shape of the concentration vs. depth profiles for oxygen, carbon and hydrogen from the surface, through the epitaxial layer and into the Cz substrate are shown in figure 5.1. The higher levels of oxygen and carbon near the surface is due

to in–diffusion during different processing steps, such as oxide growth and etching. On the other side of the epitaxial region, the Czochralski substrate contains much higher concentrations of impurities than the epitaxial layer, so these will diffuse some distance into the epitaxial layer. The concentration of hydrogen is expected have a positive gradient towards the surface because of in–diffusion during processing, such as wet etching of SiO_2 with hydroflouric acid (HF).

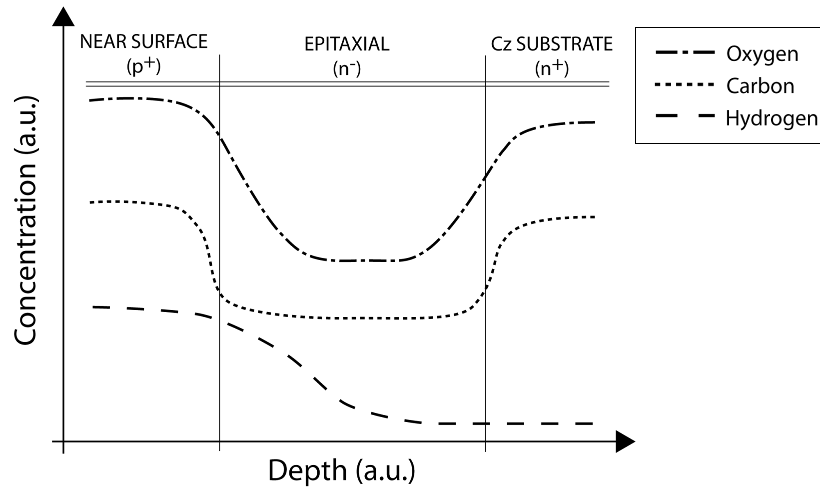

Figure 5.1: The expected shape of the concentration vs. depth profiles for oxygen, carbon and hydrogen from the surface, through the epitaxial layer and into the Cz substrate. Oxygen and carbon are the only impurities with large enough concentrations to possibly be detected by SIMS, since even phosphorous has a concentration as low as 10^{14} cm^{-3}. However, the concentrations of these impurities are shown to be below the SIMS detection limit of about 2×10^{17} cm^{-3} for oxygen and 5×10^{16} cm^{-3} for carbon in figure 5.2 except in the p^+–region close to the surface.

Hydrogen has a large diffusivity in silicon, so at room temperature all H will be trapped by some defect complex. Since the hydrogen is introduced mainly from the surface, hydrogen diffuses from the surface and towards the bulk. This is expected to result in a depth distribution of the hydrogen–containing complex which looks qualitatively like the one in figure 5.1. There may be several hydrogen related complexes, but here it will be assumed that there is only one hydrogen sink and it is labeled HZ where Z means everything in the complex which is not H. If this defect dissociates during post–irradiation annealing, then it will behave as a near–surface hydrogen source.

5.2.2 SIMS measurements

Secondary ion mass specrometry (SIMS) was performed to measure the oxygen and carbon concentrations in the samples. The result is plotted in figure 5.2. The peak near the surface for both oxygen and carbon has two distinct features as shown in 5.2(b). The first valley–like part is the partially oxidized aluminium layer which makes up the top electrode of the samples. The next peak–like part is just where the aluminium ends and the silicon starts, and shows that there is more oxygen and carbon in the p^+–region than deeper in the material. The higher [O] and [C] are most likely due to processing steps

such as oxide growth, etching and photolithography since photoresists contain substantial amounts of carbon. Another possible explanation is that gettering in the highly boron doped region makes the oxygen and carbon concentration higher there than elsewhere.

For depths larger than about 15 μm i.e. in the n^-–layer, the signals are simply the detection limit for these measurements. This means that neiter oxygen nor carbon is detected during the measurements below the aluminium layer and down to about 10-12 μm. The actual value of the depth is somewhat uncertain due to the lower erosion rate of the incident primary ions in the aluminium layer as compared to that in silicon.

It is concluded that the n^-–layer contains less than 2×10^{17} cm^{-3} oxygen and less than about 5×10^{16} cm^{-3} carbon. This is consistent with the information in figure 3.14 about the concentrations of oxygen and carbon in epitaxial layers produced by ITME, where [O] is said to be $(3-4) \times 10^{16}$ cm^{-3} and [C] is given as $\sim 1 \times 10^{16}$ cm^{-3}.

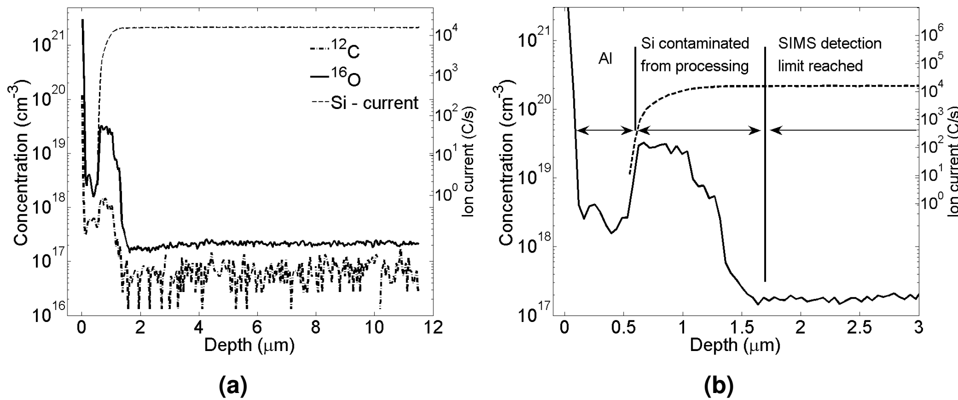

Figure 5.2: SIMS measurements of the concentration of carbon and oxygen **(a)** and a magnified view which shows the aluminium layer and the carbon– and oxygen–contaminated silicon surface region **(b)**. The measured current of sputtered silicon ions is also displayed to further show where the aluminium layer ends and the silicon epitaxial layer starts. The detection limit is 2×10^{17} cm^{-3} for oxygen and about 5×10^{16} cm^{-3} for carbon.

5.3 Isochronal annealing: Thermal stability

In figure 5.3 the DLTS spectra for the isochronal measurements are plotted for annealing temperatures from RT – 225 and 225 – 425°C. The 640 ms rate window of the lock–in type weighting function is used for all plots of DLTS spectra in this thesis unless otherwise is specified.

The annealing time was 20 min at each temperature and the annealing was done in N_2 gas for temperatures above 250°C to avoid in–diffusion of impurities and possible oxidation of the Al contacts.

The position and assignment of the peaks are well established for VO, V_2, V_2O and VOH. It is also possible to see from the measurement at 350 °C that there is a prominent level at 170 K which is labeled E(170 K). However, it is not possible to determine from the measurements in figure 5.3(b) which other minor levels are contributing to the DLTS signal between 140 – 170 K. The position of the L–center is pointed out simply because its position is in this temperature interval, but it is not possible to determine whether it is actually present in these spectra.

The concentration of VO, V_2 and V_2O is found as described in section 4.2.3.9 by using equation (4.16), and the results from the isochronal annealing is plotted in figure 5.4. Note that only non–overlapping peaks can be directly analyzed in this way. The concentration of overlapping peaks can be determined by using a fitting procedure as described and justified in the following section. The accuracy of the fitted concentrations is slightly reduced since it is determined from only one rate window, and is not the average of the concentration as determined in each invidual rate window. The concentrations of V_2 and V_2O is separated in figure 5.4. This is based on fitting each indivdual concentration so that the position of the total peak, corresponding to [V_2+ V_2O], matches the shift in position as the reaction $V_2 + O_i \rightarrow V_2O$ takes place.

As mentioned, VO, V_2, V_2O and VOH are relatively well known. However, the L–center and the peak labeled $E_c - 0.37$ eV have only recently been described by Mikelsen [27] and Bleka [4], respectively. The defect level labeled $E_c - 0.37$ eV is believed to have another level which overlaps with $V_2^{-/0}$ and $V_2O^{-/0}$. $E_c - 0.37$ eV is unstable at room temperature. To the best of the authors knowledge no articles have been published focusing on the two peaks labeled E(170 K) and E(198 K) appearing after annealing at about 325 – 375°C. E(198 K), however, is mentioned briefly as a minor defect in a number of articles, such as by Mikelsen et al. in reference [25] where it is suggested to be V_2OH.

5.3.1 Separation of overlapping peaks

Either fitting of the lock–in DLTS spectra or a weighting function with a larger resolution is required to determine the number of levels, the electrical properties and the concentration of the individual levels in the temperature region between $V_2O^{=/-}$ and $V_2O^{-/0}$. In this thesis a combination of fitting and the GS4 weighting function is used. However, the use of fitting requires some explanation and justification.

5.3.1.1 Determination of the number of overlapping levels

The isochronal measurement at 350 °C is plotted in three different versions in figure 5.5. By comparing the lock–in spectrum in 5.5(a) to the GS4 spectrum in 5.5(b) it can be seen that the levels are partly separated by applying the GS4 weighting function instead of lock–in. However, it is also clear that the GS4 spectrum is quite noisy because the GS4 spectrum has a signal to noise ratio (SNR) smaller than that of the lock–in spectrum by about a factor of 10. Therefore, the situation can be made clearer by smoothing the spectrum with a running average of neighboring data points. This is done over the two

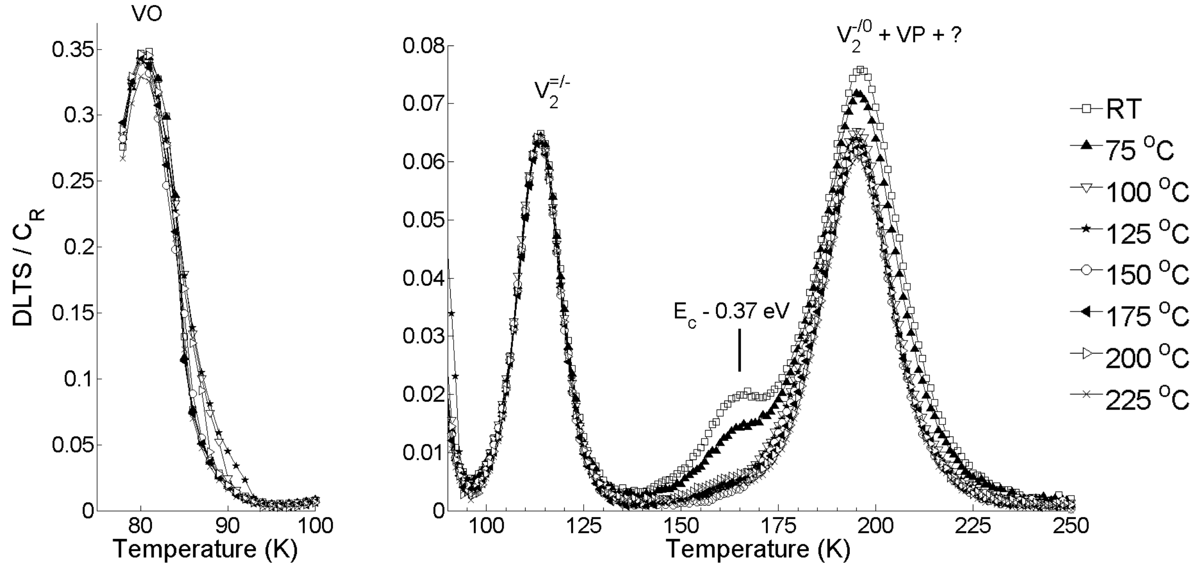

(a) Isochronal annealing from RT to 225°C.

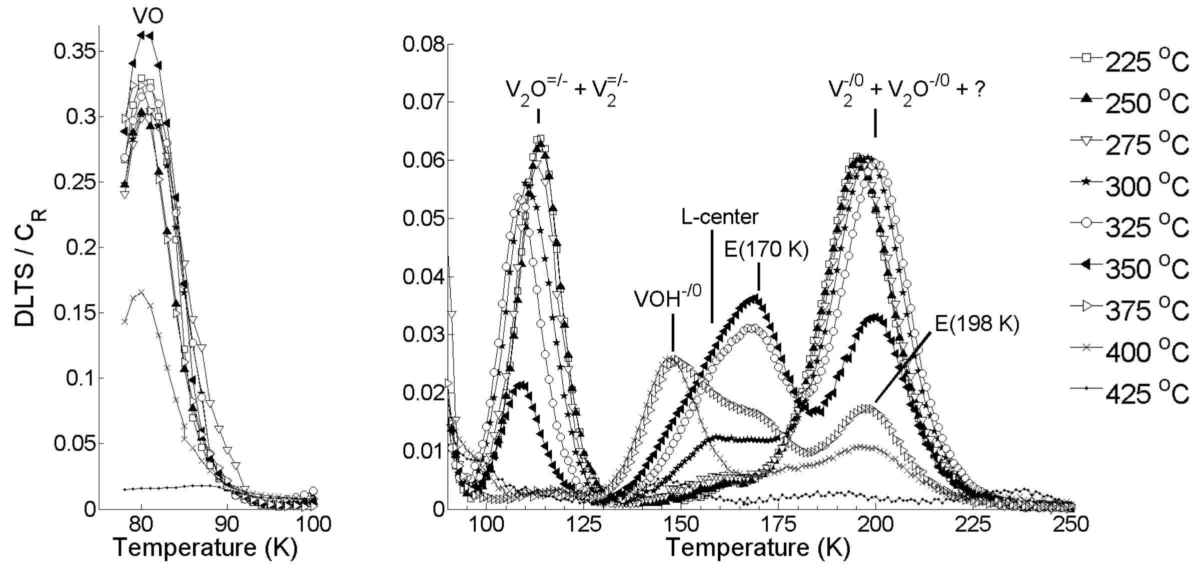

(b) Isochronal annealing from 225–425°C.

Figure 5.3: DLTS spectra obtained by isochronal annealing from RT – 225°C **(a)** and from 225 – 425°C **(b)**. The spectra are of the 640 ms rate window of the lock–in type weighting function, the annealing time was 20 min and the annealing was done in N_2 gas above 250°C. C_R is the reverse bias capacitance, so DLTS / C_R is proportional to N_t.

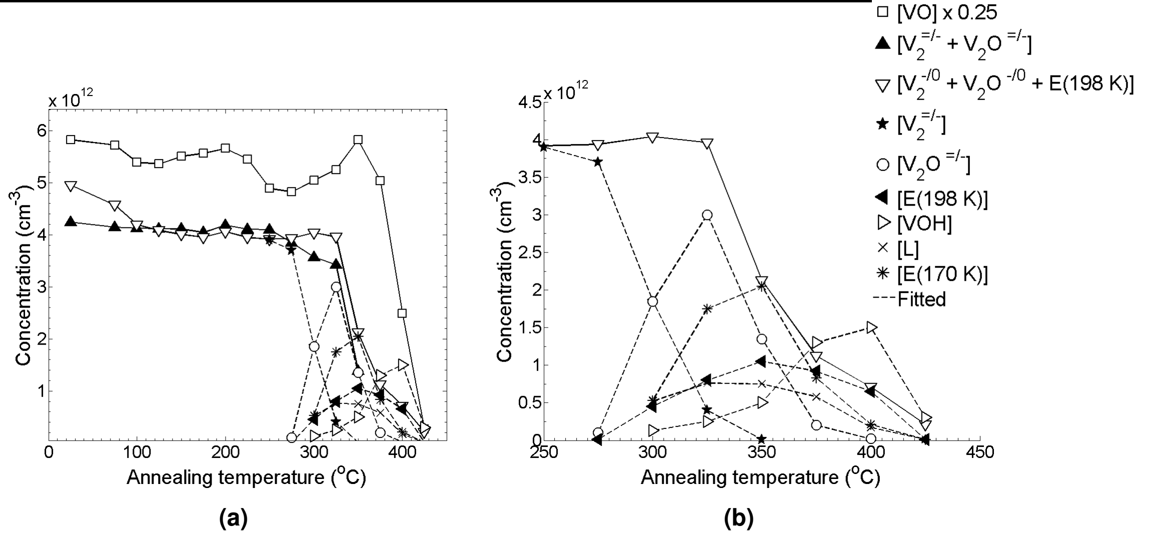

Figure 5.4: Concentration as a function of annealing temperature from the isochronal annealing experiment for all the detected levels **(a)** and a magnified view of the minor levels which are separated by fitting of the DLTS spectra **(b)**. [VO] is scaled by a factor of 0.25. The concentrations of V_2 and V_2O are separated by fitting of the individual concentrations to get the amplitude of the overall DLTS peak.

nearest neighboring points on either side of all data points in figure 5.5(c). Thus, each smoothed measurement is the average of a total of 5 unsmoothed measurements as

$$S_{smoothed}(T_i) = \sum_{j=i-2}^{i+2} S_{unsmoothed}(T_j)$$

from $i = 2 - (\text{no. points} - 2)$. The end regions of the temperature interval 77 – 300 K are averaged over fewer DLTS data points, that is 77–78 K and 299–300 K.

However, smoothing can change the shape of a spectrum, hence the comparison between the unsmoothed and the smoothed GS4 spectra is included to show that the use of smoothing in this case does not change the position of the peaks although their amplitudes are somewhat reduced.

It is clear from the GS4 spectra in figure 5.5(b) and 5.5(c) that there are three partially overlapping peaks in the temperature range 140 – 180 °C. The indicated properties of these three levels and thus the labeling as VOH, the L–center and E(170 K) is justified in the following section.

5.3.1.2 Determination of the level properties

The labeling of VOH is so far tentative, since it is not possible to do a straight forward determination of ΔH and σ_{na} by Arrhenius plotting due to the overlap with both E(170 K) and the peak at about 158 K, as shown in figure 5.5. However, there are intervals of annealing time during which VOH has a large amplitude while E(170 K) and the middle

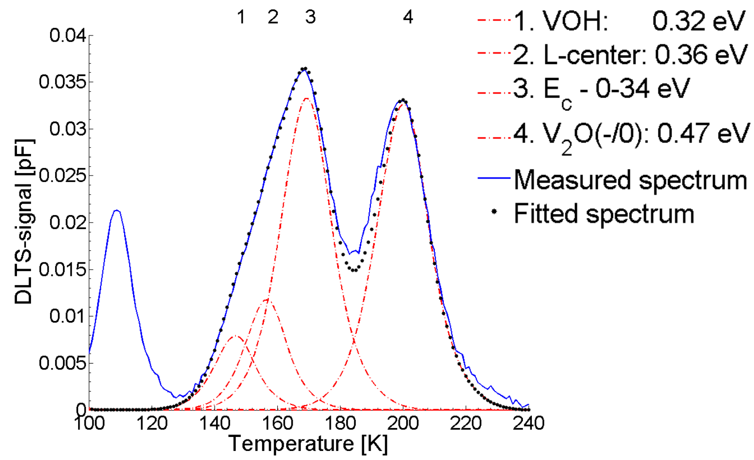

(a) Using the lock–in weighting function.

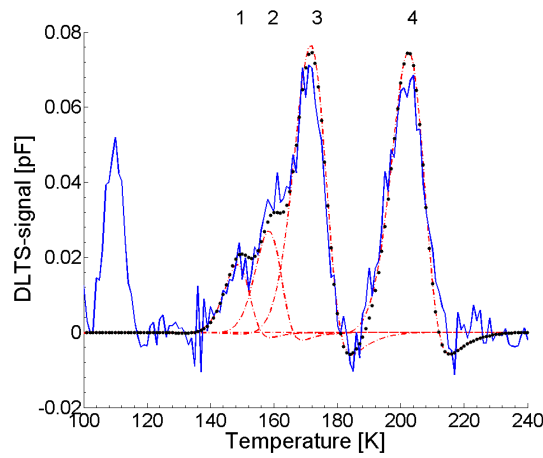

(b) Using the GS4 weighting function.

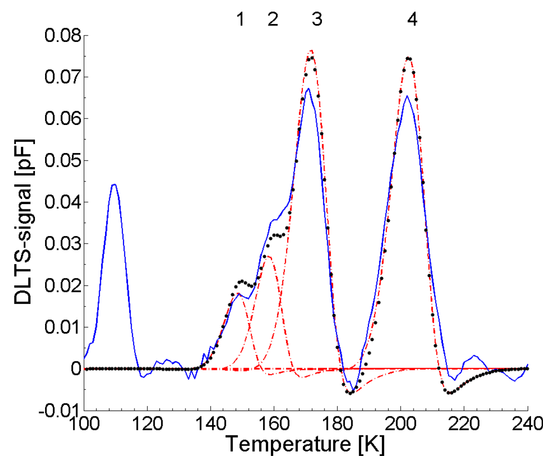

(c) Using GS4 and performing a running average with 2 neighbors on either side.

Figure 5.5: Fitting of the 350 °C measurement from figure 5.3(b) between the two V_2O peaks by using a lock–in **(a)**, GS4 **(b)** and GS4 weighting function after smoothing by doing a running average where each DLTS data point is the average of the amplitude of itself and its two nearest neighboring points on either side **(c)**.

peak have very small amplitudes. Conversely, when E(170 K) has a large amplitude, then VOH has a small amplitude.

Therefore, care is taken in the determination of ΔH and σ_{na} to only use the spectra where the peak in question is clearly larger than its neighbors, as given in table 5.1. This procedure is necessary because overlap from neighboring peaks not only adds to the amplitude of the total peak, but also shifts the position of the peak towards an overlapping peak if the degree of overlap and the amplitude of the neighboring peak is sufficiently large. This procedure is used to determined ΔH and σ_{na} with some degree of statistical accuracy.

By using equation (4.19) a synthetic fitted spectrum is created with VOH and E(170 K) in the positions determined from the Arrhenius plots. The individual amplitudes of these peaks, and thus the resulting concentration of the defect, is determined by manually fitting the synthetic spectrum to the measured spectrum. This is done so that a good fit is achieved in all the lock–in rate windows 20 – 640 ms. The lock–in weighting function is used since it is less noisy than GS4.

This is done for all four isothermal series and $\Delta H \pm \Delta(\Delta H)$ and $\sigma_{na} \pm \Delta\sigma_{na}$ are calculated based on all the measurements, where ΔH is the mean value and $\Delta(\Delta H)$ is the standard deviation and similarly for σ_{na}. The intervals of annealing time used to calculate the level properties are listed in table 5.1.

Trap label	Annealing temperature (°C)	Start time	–	End time (min)
VOH	325	900	–	7530
	338	340	–	2600
	350	210	–	1200
	360	111	–	580
E(170 K)	325	10	–	480
	338	0	–	190
	350	0	–	60
	360	0	–	46

Table 5.1: A summary of the interval of annealing times in which each respective isothermal series was used for the determination of ΔH and σ_{na} for VOH and E(170 K) by Arrhenius plots.

The values of ΔH and σ_{na} determined in this way can be compared to the values which were eventually used in the fitting for all the isothermal series. The values used in the fitting are very close to the average measured values, as can be seen in table 5.2.

Finding ΔH and σ_{na} for the middle level at 158 K between VOH and E(170 K) is now possible since there is only one set of defect parameters to vary until a good fit is achieved. It is found that $\Delta H = 0.36$ eV and $\sigma_{na} = 2.4 \times 10^{-14}$ cm^2 gives an excellent fit to the measured spectra together with the values for VOH and E(170 K) given in table 5.2. These values for ΔH and σ_{na} are in such close agreement with those previously reported for the L–center, $\Delta H = 0.36$ eV and $\sigma_{na} = 2.2 \times 10^{-14}$ cm^2, that this level is concluded to originate from the L–center [27]. This level is not investigated any further in this work, but its concentration is taken into account in the fitting procedure in order to determine the correct concentrations for VOH and E(170 K).

It is necessary to include $V_2O^{-/0}$ in the fitting since this level partially overlaps with E(170 K). When $[V_2O] = 0$, then E(198 K) was included in the fitting instead, since these levels completely overlap. The transition of the peak from $V_2O^{-/0}$ to E(198 K) consists in a shift in peak position from 200 K to 198 K.

ΔH and σ_{na} for E(198 K) are used for all annealing times after $[V_2O^{=/-}] = 0$, since after this the peak at 198 K is assumed to consists entirely of E(198 K). The concentration of E(198 K) is extracted as

$$[\text{E(198 K)}] = [V_2O^{-/0}] - [V_2O^{=/-}] \tag{5.1}$$

at each annealing step. Thus, no fitting is involved in the treatment of E(198 K) at all.

The activation enthalpies and capture cross sections listed in table 5.2 are used with no variations to fit [VOH] and [E(170 K)] at all annealing times and all four annealing temperatures in this work. Thus, only the concentrations of the defects are varied in order to achieve a good fit.

	Measured		Used in fitting	
Trap label	ΔH (eV)	σ_{na}(cm^2)	ΔH (eV)	σ_{na}(cm^2)
VOH	0.325 ± 0.009	$(7 \pm 4) \times 10^{-15}$	0.32	7.0×10^{-15}
†L–center	–	–	0.36	2.4×10^{-14}
E(170 K)	0.34 ± 0.01	$(8 \pm 6) \times 10^{-16}$	0.34	7.0×10^{-16}
$^\dagger V_2O^{-/0}$	–	–	0.47	2.6×10^{-14}
E(198 K)	0.46 ± 0.02	$(1.5 \pm 1) \times 10^{-14}$	0.46	2.0×10^{-14}

Table 5.2: The level properties used to fit all the DLTS spectra that were aquired in this work in the temperature range 140 – 180 K. $^\dagger\Delta H$ and σ_{na} used to fit the L–center and the well known level $V_2O^{-/0}$ are taken from litterature, as can be seen by comparison with table C.1 in appendix C. The small differences in σ_{na} are well within the experimental accuracy.

The measured ΔH and σ_{na} for E(170 K) and E(198 K) agree roughly with measurements of minor peaks at the same positions by Mikelsen et al. in references [24, 25]. In these references, $\Delta H = 0.31$ eV and $\sigma_{na} = 4 \times 10^{-17}$ cm^2 are obtained for E(170 K) whereas $\Delta H = 0.44$ eV and $\sigma_{na} = 7 \times 10^{-15}$ cm^2 are obtained for E(198 K). The difference between these values and the ones measured in this work are readily explained by the small concentrations of E(170 K) and E(198 K) and the corresponding reduction in measurement accuracy.

5.3.2 Comparison to previous work on DOFZ– and MCz–Si

The isochronal annealing behavior of the defect levels in EPI–Si as compared to DOFZ– and MCz–Si is shown in figure 5.6. The impurity concentrations in the various materials are compared in table 5.3. The estimation of the hydrogen content is based on the amount of VOH relative to V_2, since the concentration of V_2 depends only on the dose. Thus, V_2 is convenient to use as an impurity independent reference.

Material	Oxygen (cm^{-3})	Carbon (cm^{-3})	Hydrogen
DOFZ	$(2-3)\times10^{17}$	$(2-4)\times10^{16}$	Most
MCz	$(5-10)\times10^{17}$	$\leq 10^{16}$	Least
EPI	$\leq 2\times10^{17}$	$\leq 5\times10^{16}$	Intermediate

Table 5.3: Comparison of the impurity concentrations. The data for oxygen and carbon were introduced earlier, in table 3.4 for DOFZ and MCz, and in section 5.2.2 for EPI. Hydrogen is introduced unintentionally during processing, and is not a characteristic of any of these materials, unlike the concentrations of oxygen and carbon.

The differences in the annealing of defects in DOFZ, MCz and EPI are summarized in table 5.4, and the most significant issues from table 5.4 and figure 5.6 are discussed below.

The maximum concentration of VOH is largest in DOFZ and smallest in MCz.

The growth of VOH ceases when the concentration of H is depleted, not VO. This is evident since the concentration of VOH starts to decrease long before [VO] reaches the detection limit. This means that the maximum concentration of VOH could be used as a qualitative measure of the amount of H in the sample.

The maximum concentration of VOH is largest in DOFZ and smallest in MCz in the samples studied here and in reference [25]. This is an indication that [H] is lowest in MCz and highest in DOFZ in these samples. Another possible explanation for the lack of measured VOH is that the reaction $VO + O_i \rightarrow VO_2$ could be preferred over the reaction $VO + H \rightarrow VOH$ in MCz, since [O_i] is highest in MCz.

VO anneals out fastest in DOFZ, and slowest in EPI.

This is difficult to understand if $VO + O_i \rightarrow VO_2$ is expected to be a major process, since [O_i] is highest in MCz, not in DOFZ, and expected to be lowest in EPI. Thus, the probability of capture of VO at O_i is largest in MCz and the annealing rate for this process should be larger in MCz than in DOFZ.

However, if $VO + H \rightarrow VOH$ is considered, then this makes more sense. [H] is higher in the investigated DOFZ samples than in the MCz and EPI samples, so this accounts for the larger annealing rate in DOFZ if the creation of VOH is an important process. The combination of a low [O_i] and an intermediate [H] could make the annealing rate of VO smaller in EPI than in MCz, where [O_i] is much larger. Another possibility is that the creation of VOH is suppressed in MCz due to the large [O_i], making the creation of VO_2 preferable.

V_2O anneals out by far the fastest in DOFZ, and slowest in MCz, with EPI somewhere in between.

This could be an indication of hydrogen assisted annealing, through $V_2O + H_n \rightarrow V_2OH_n$. n implies that the hydrogen can be monoatomic, diatomic or more complex, so $n \geq 1$. This scenario explains that the annealing rate of V_2O is largest in DOFZ where [H] is expected to be highest, and smallest in MCz where [H] is expected to be lowest in these samples.

There is maximum concentration of E(170 K) in EPI and least in MCz.

This is an indication that the creation of E(170 K) during the post–irradiation annealing is suppressed in oxygen–rich materials, since [O_i] is highest in MCz and lowest in EPI. The reason could be that the precursor of E(170 K) is depleted by a reaction with O_i in oxygen–rich materials which competes with the creation of E(170 K).

On the other hand, E(170 K) could be connected to [C]. However, only upper limits for [C] is measured in both EPI and MCz, which makes a further discussion of this scenario difficult.

There is maximum concentration of E(198 K) in DOFZ and least in MCz.

This indicates that the creation of E(198 K) during the post–irradiation annealing is suppressed in hydrogen–lean materials, since $[\mathrm{VOH}]_{max}$ is highest in DOFZ and lowest in MCz. Thus, the E(198 K) defect may contain H.

5.4 Isothermal annealing: Reaction kinetics

5.4.1 Pre–annealing: Conversion of V_2 into V_2O

The V_2 centers in as–irradiated samples must be converted into V_2O through a so-called pre–annealing procedure at a certain temperature and for a certain time before the possible production of hydrogen related defects from migration or dissociation of VO and V_2O can be studied. The reactions are

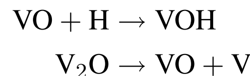

$$\mathrm{VO} + \mathrm{H} \rightarrow \mathrm{VOH}$$
$$\mathrm{V_2O} \rightarrow \mathrm{VO} + \mathrm{V}$$

The temperature must be sufficiently high to make V_2 mobile and enable the formation of V_2O, but it should be below the temperature range for the subsequent isothermal experiments to prevent that the interesting reactions happen already during the pre–annealing. The conversion from V_2 to V_2O occurs by divacancy migration and subsequent trapping by O_i,

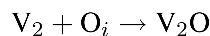

$$\mathrm{V_2} + \mathrm{O}_i \rightarrow \mathrm{V_2O}$$

as shown in reference [26].

A representative selection of the annealing steps during a pre–annealing at 275 °C is presented in figure 5.7. At 0 min, in the as–irradiated condition, the $V_2^{-/0}$ peak is significantly larger than $V_2^{=/-}$ possibly because of cluster defects which disappear rapidly at elevated temperatures [4]. The transistion from V_2 to V_2O can be seen in that $V_2^{=/-}$ shifts to lower temperatures whereas $V_2^{-/0}$ shifts to higher temperatures. The positions of both peaks seem to stabilize after about 330 – 360 min with about 90% of the original amplitude of the presumably pure $V_2^{=/-}$ peak.

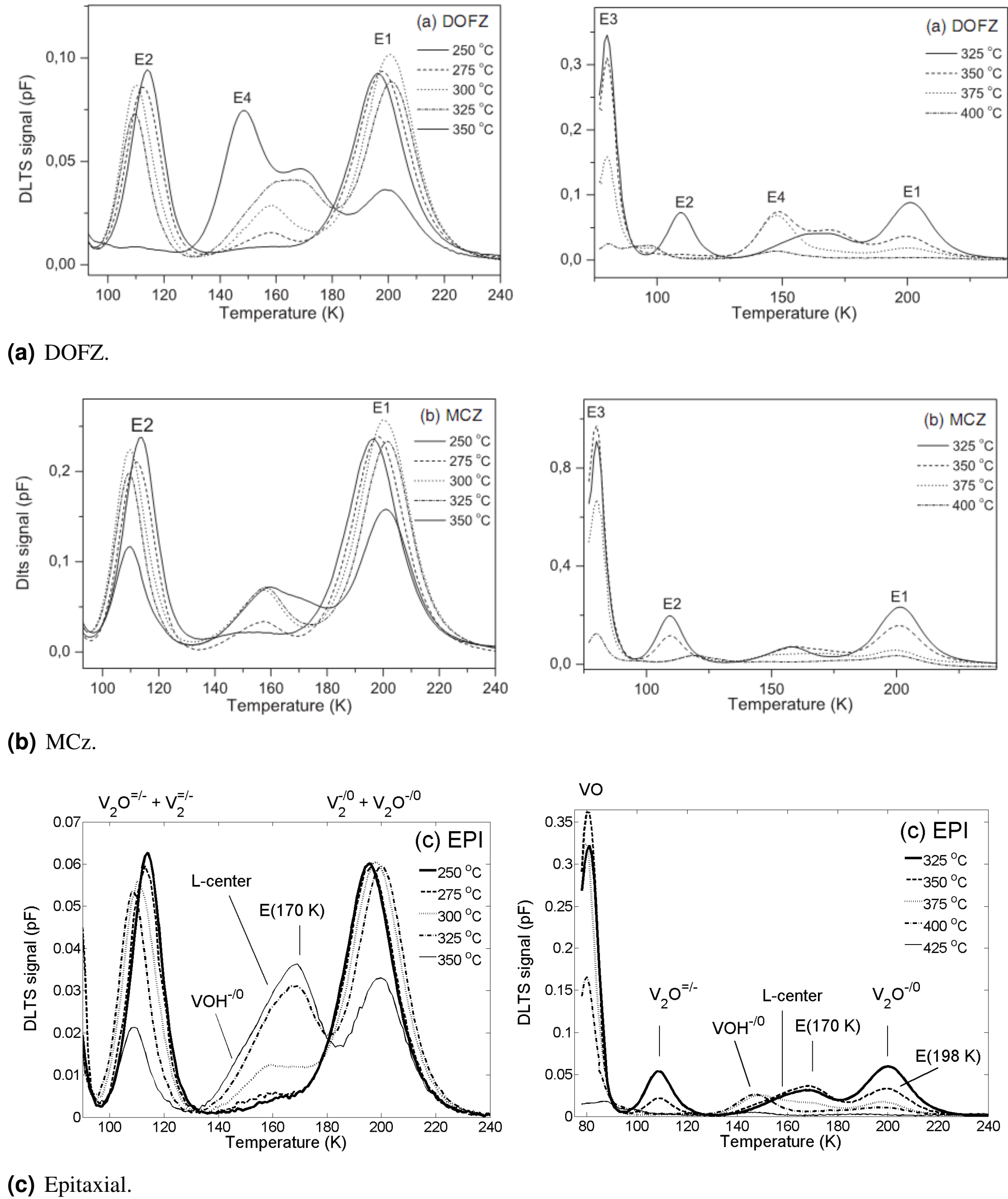

(a) DOFZ.

(b) MCz.

(c) Epitaxial.

Figure 5.6: Comparison of DOFZ– **(a)**, MCz– **(b)** and EPI–Si **(c)** during isochronal annealing in the temperatures 250 – 425 °C. The data for DOFZ– and MCz–Si are from reference [25], whereas the data for EPI–Si are from figure 5.3. E1–E4 is the labeling used by Mikelsen et al. In this work the defects will be refered to as they are labeled in **(c)**.

Defect	DOFZ	MCz	EPI
VO	– Disappears between 325 – 350 °C. – No increase before disappearing. – $[\mathrm{VO}]_{375^\circ\mathrm{C}} \sim 0.45 \times [\mathrm{VO}]_{250^\circ\mathrm{C}}$	– Disappears between 350 – 375 °C. – Increases slightly, then disappears. – $[\mathrm{VO}]_{375^\circ\mathrm{C}} \sim 0.75 \times [\mathrm{VO}]_{250^\circ\mathrm{C}}$	– Disappears between 350 – 375 °C. – Decreases, then increases before disappearing. – $[\mathrm{VO}]_{375^\circ\mathrm{C}} \sim 1.0 \times [\mathrm{VO}]_{250^\circ\mathrm{C}}$
$V_2$and V_2O	– $V_2 \rightarrow V_2O$ starts at 250 °C and is complete at 325 °C. – $[\mathrm{V_2O}]_{325^\circ\mathrm{C}} \sim 0.8 \times [\mathrm{V_2}]_{250^\circ\mathrm{C}}$ – $[\mathrm{V_2O}]_{350^\circ\mathrm{C}} \sim 0$	– $V_2 \rightarrow V_2O$ starts at 250 °C and is complete at 325 °C. – $[\mathrm{V_2O}]_{325^\circ\mathrm{C}} \sim 0.8 \times [\mathrm{V_2}]_{250^\circ\mathrm{C}}$ – $[\mathrm{V_2O}]_{350^\circ\mathrm{C}} \sim 0.5 \times [\mathrm{V_2}]_{250^\circ\mathrm{C}}$	– $V_2 \rightarrow V_2O$ starts at 250 °C and is complete at 325 °C. – $[\mathrm{V_2O}]_{325^\circ\mathrm{C}} \sim 0.8 \times [\mathrm{V_2}]_{250^\circ\mathrm{C}}$ – $[\mathrm{V_2O}]_{350^\circ\mathrm{C}} \sim 0.3 \times [\mathrm{V_2}]_{250^\circ\mathrm{C}}$
VOH	– Appears at 325 °C, all gone at 400 °C. – Reaches maximum value at 350 °C. – $[\mathrm{VOH}]_{\mathrm{max}} \sim 0.85 \times [\mathrm{V_2}]_{250^\circ\mathrm{C}}$	– No VOH detected.	– Appears at 300 °C, all gone at 425 °C. – Reaches maximum value at 400 °C. – $[\mathrm{VOH}]_{\mathrm{max}} \sim 0.4 \times [\mathrm{V_2}]_{250^\circ\mathrm{C}}$
L–center + E(170 K)	– Appears at 275 °C, all gone at 375 °C. – Reaches maximum value at 350 °C. Mostly E(170 K). – $[L + \mathrm{E(170\ K)}]_{\mathrm{max}} \sim 0.4 \times [\mathrm{V_2}]_{250^\circ\mathrm{C}}$	– Appears at 275 °C, all gone at 400 °C. – Reaches maximum value at 350 °C. Mostly L–center. – $[L + \mathrm{E(170\ K)}]_{\mathrm{max}} \sim 0.3 \times [\mathrm{V_2}]_{250^\circ\mathrm{C}}$	– Appears at 300 °C, all gone at 400 °C. – Reaches maximum value at 350 °C. Mostly E(170 K). – $[L + \mathrm{E(170\ K)}]_{\mathrm{max}} \sim 0.5 \times [\mathrm{V_2}]_{250^\circ\mathrm{C}}$
E(198 K)	– Appears at 325 °C, all gone at 400 °C. – $[\mathrm{E(198\ K)}]_{\mathrm{max}} \sim 0.45 \times [\mathrm{V_2}]_{250^\circ\mathrm{C}}$	– Appears at 325 °C, all gone at > 400 °C. – $[\mathrm{E(198\ K)}]_{\mathrm{max}} < 0.2 \times [\mathrm{V_2}]_{250^\circ\mathrm{C}}$	– Appears at 300 °C, all gone at 400 °C. – $[\mathrm{E(198\ K)}]_{\mathrm{max}} \sim 0.25 \times [\mathrm{V_2}]_{250^\circ\mathrm{C}}$

Table 5.4: A summary of the differences in the annealing of the defects in DOFZ–, MCz– and EPI–Si. VO anneals out fastest in DOFZ and slowest in EPI. V_2O also anneals out fastest in DOFZ, but slowest in MCz. There is most VOH in DOFZ, and least in MCz.

Hence, it is concluded that an annealing time of 360 min at 275 °C is sufficient to convert as much as possible of V_2 into V_2O, although about 10% is lost in other reactions or is lost by annealing of V_2O before the pre–annealing procedure is stopped.

Several highly overlapping peaks form in the temperature region between the two V_2 peaks, as was also seen in the isochronal measurements in figure 5.3(b). The concentrations of these peaks are too small and the degree of overlap is too large to identify any of them from these measurements. None the less, in figure 5.7 the positions of VOH, the L–center and the E(170 K) defect are pointed out where they appear in the isochronal annealings in figure 5.3(b). This is also done in anticipation of the isothermal annealing experiments at higher temperatures in the next section when the concentrations increase.

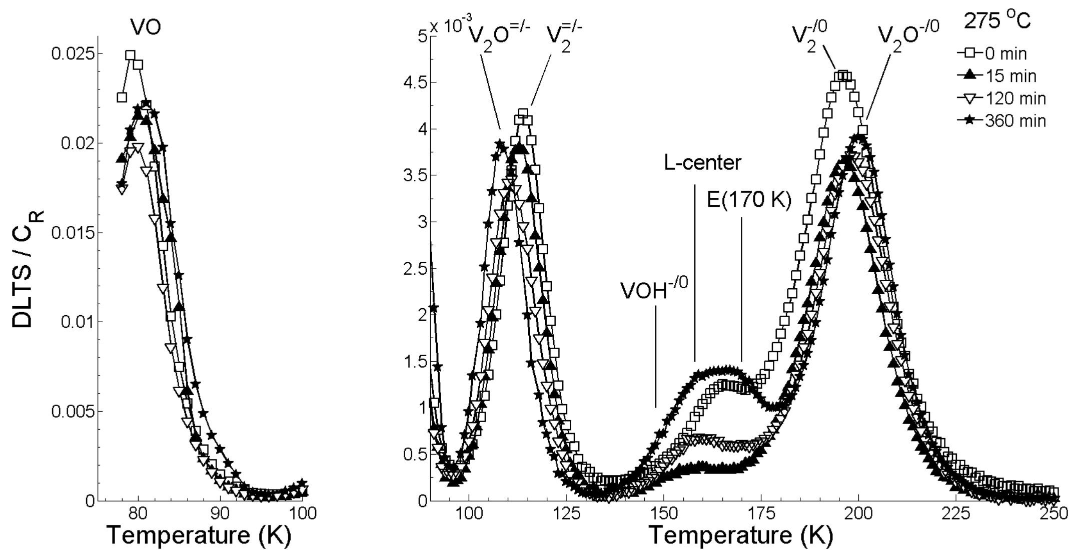

Figure 5.7: The results of the pre–annealing procedure at 275 °C which converts V_2 into V_2O. It is found that an annealing time of 360 min converts more than 90% of the V_2 to V_2O, as seen from the $V_2^{=/-}$ peak. The $V_2^{-/0}$ peak decreases more than $V_2^{=/-}$ because of the out–annealing of an overlapping cluster defect [4]. Only a selection of the measured spectra are displayed to increase the readability of the figure.

5.4.2 Isothermal annealing at 325, 338, 350 and 360 °C

Isothermal annealing was performed at 325, 338, 350 and 360 °C after pre–annealing for 360 min at 275 °C. A selection of the measured spectra are presented in figures 5.8(a) – 5.8(d). All spectra are from the 640 ms lock–in rate window.

VO initially increases slightly at all annealing temperatures, before it decreases steadily. V_2O decreases steadily through the entire annealing process until it disappears. This is consistent with the annealing behavior of VO as observed by Mikelsen in reference [25] in materials where [O] is not too high. The increase in VO was attributed to dissociation of V_2O, $V_2O \rightarrow V + VO$. This phenomenon was argued to occur only in samples where

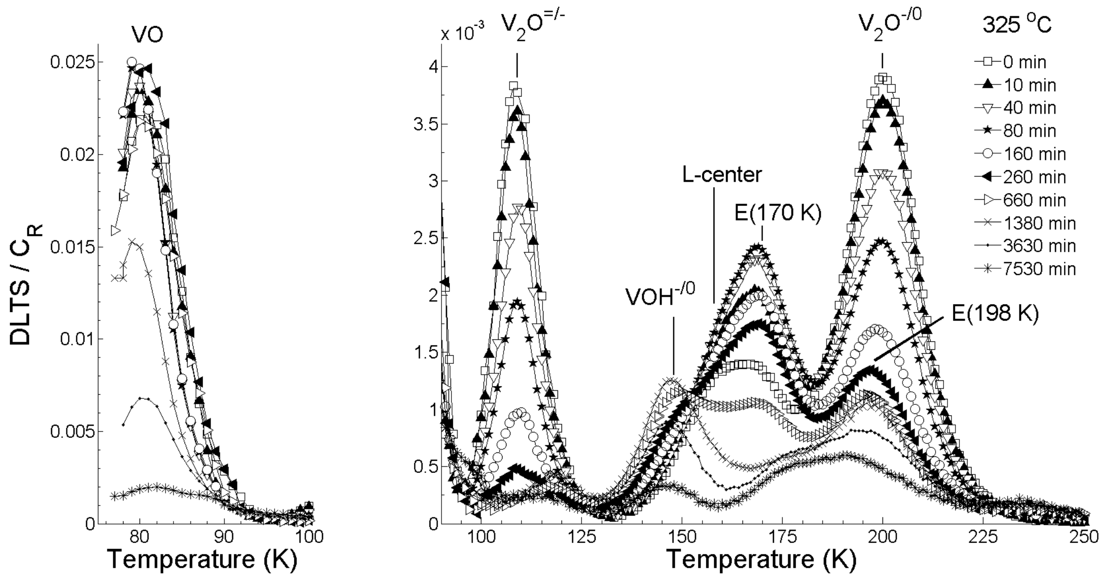

(a) Isothermal annealing at 325 °C.

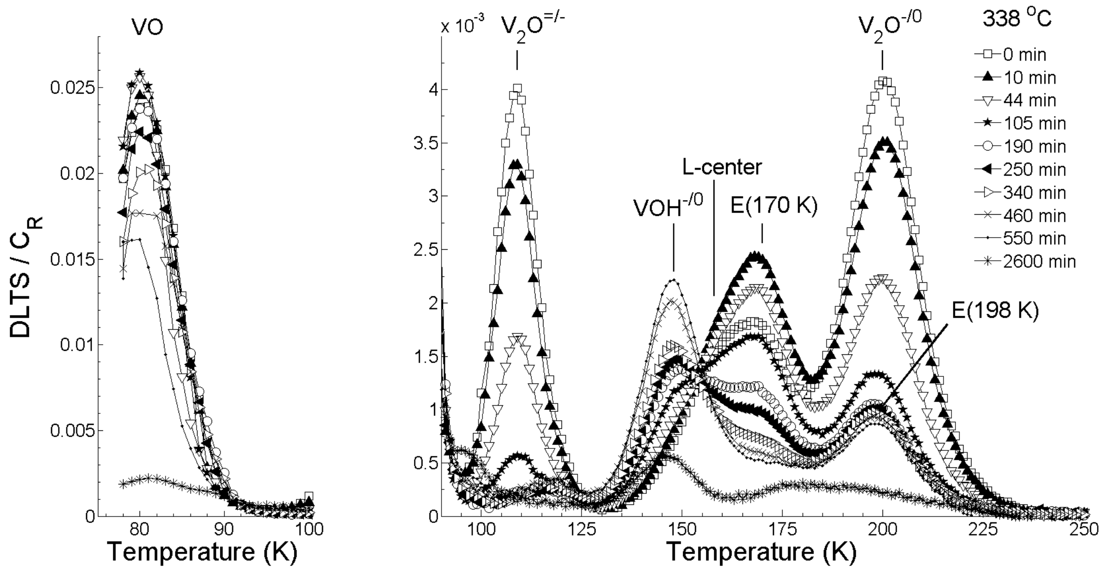

(b) Isothermal annealing at 338 °C.

Figure 5.8: A selection of the isothermal annealing steps performed at 325 °C **(a)** and 338 °C **(b)**. Notice that especially [VOH] has a much larger maximum value in the annealing at 338 °C than at 325 °C, and also that the signal amplitude between 175 – 200 K is larger for long annealing time at 325 °C.

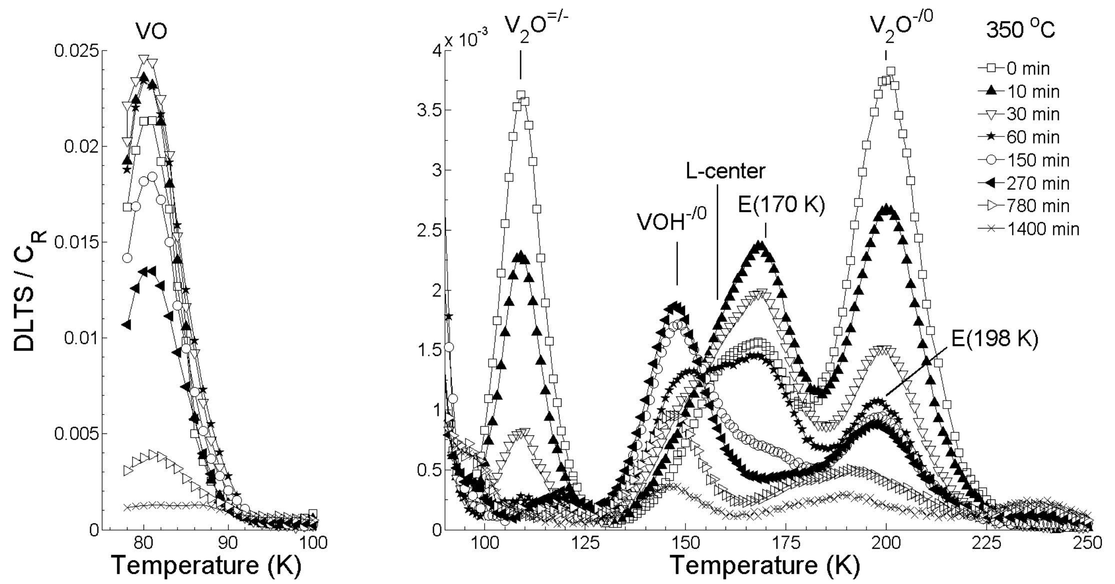

(c) Isothermal annealing at 350 °C.

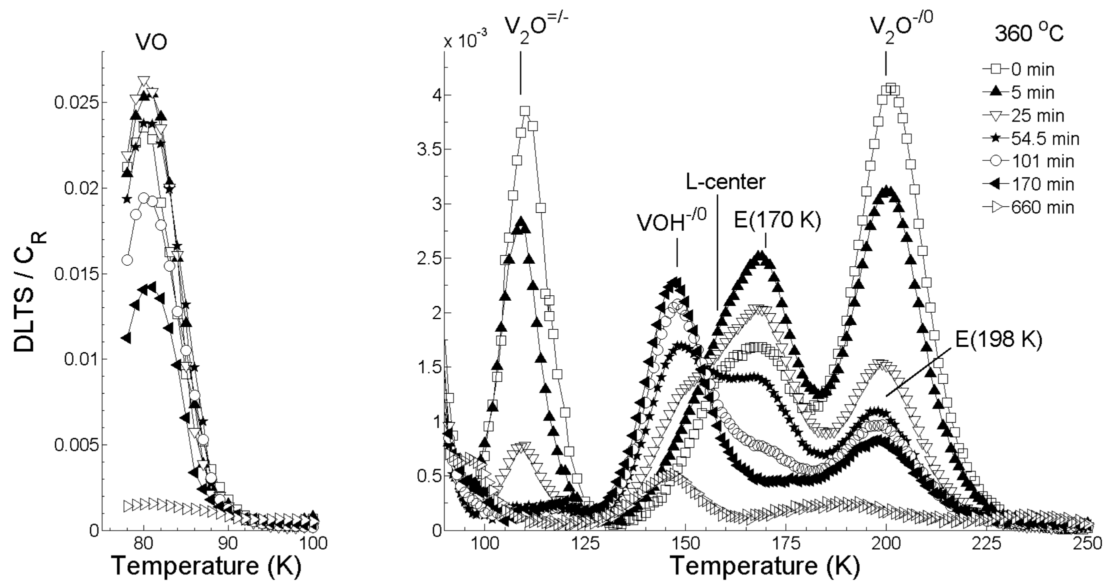

(d) Isothermal annealing at 360°C.

Figure 5.8: A selection of the isothermal annealing steps performed at 350 °C **(c)** and 360 °C **(d)**.

[O] was not too high, because a larger oxygen concentration gives a larger the probability of trapping at O_i as $VO + O_i \rightarrow VO_2$. It was found by modeling that there was no initial increase in VO if [O] was increased to above 4×10^{17} cm^{-3}.

The E(170 K) peak has a significant amplitude already after pre–annealing, so temperatures 325–360 °C are too high to study the growth of this defect. It reaches its maximum concentration after only a few minutes at all the four temperatures, and then decreases. Before it reaches its maximum it is clearly seen that this peak is too wide to originate from one level only. This is because of the contribution from the L–center. The VOH peak starts to increase while E(170 K) decreases. It is not possible to describe the evolution of the L–center since it is completely buried in E(170 K) and VOH at all times.

The V_2O peaks anneal out in an asymmetric way, where $V_2O^{-/0}$ anneals noticably slower than $V_2O^{=/-}$. This implies that there is some minor peak overlapping with $V_2O^{-/0}$. This becomes apparent when $V_2O^{=/-}$ is all gone, since the relatively minor peak labeled E(198 K) still remains at ∼198 K near the position of $V_2O^{-/0}$. The region between E(170 K) and E(198 K) is a complex mixture of minor defects for the last annealing times at 325 °C, but the DLTS signal in this region is considerably cleaner at 338, 350 and 360 °C.

The extracted concentrations of all the peaks, except the L–center, versus time are shown in figure 5.9 for the annealing at 325 °C. This is representative for all the annealing temperatures. The concentrations of VOH and E(170 K) are found by fitting of the DLTS spectra.

5.4.3 Known defects

In this section the annealing behavior of the individual defects is analysed, and each defect is put into context with other defects whenever possible.

5.4.3.1 VO

At temperatures of ∼300 °C and above it is expected that VO is lost through a combination of dissociation, and migration and subsequent reaction with either atomic oxygen or hydrogen. This results in the electrically inactive VO_2 or the electrically active VOH [24,33] through the reactions

$$VO \rightarrow V + O_i \tag{5.2}$$

$$VO + H \rightarrow VOH \tag{5.3}$$

$$VO + O_i \rightarrow VO_2 \tag{5.4}$$

However, assuming that the sample contains V_2O, a positive contribution to [VO] at about 300 °C can also come from the dissociation of V_2O as $V_2O \rightarrow V + VO$ since V_2O disappears at lower temperatures than VO. This can be the explanation for the noticeable increase in [VO] at 300 – 350 °C in figure 5.4. This is also the conclusion reached in

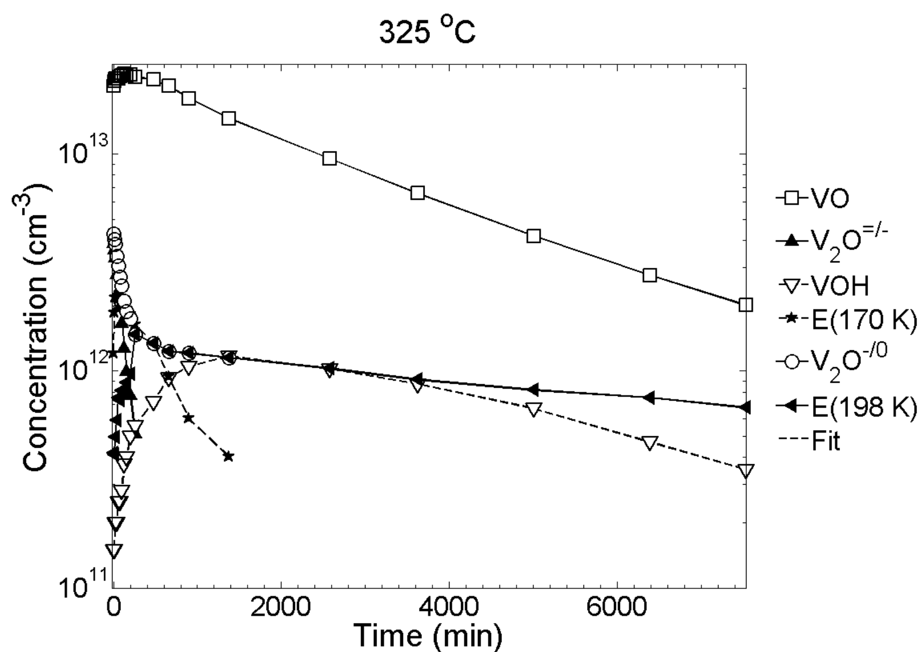

(a) The full view of all the defects.

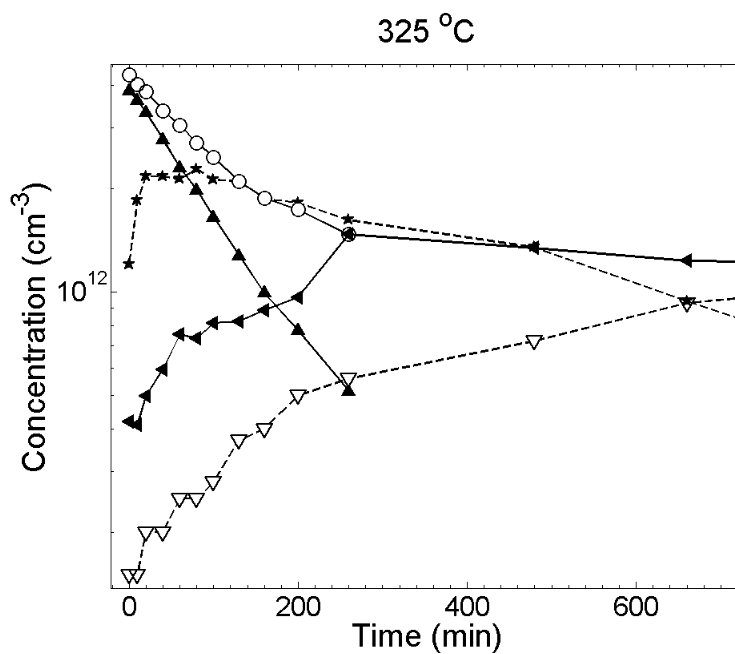

(b) A closer look at the minor defects.

Figure 5.9: Concentration plotted vs. time from the annealing at 325 °C for the entire measurement interval **(a)**, and a closer look at the minor defects except the L–center **(b)**. Notice that $[V_2O^{-/0}]$ (○) and [E(198 K)] (◀) merge when $[V_2O^{=/-}] \rightarrow 0$ (▲). Notice also the initial increase in [VO] until around 100 min. The solid and dashed lines are intended to guide the eye.

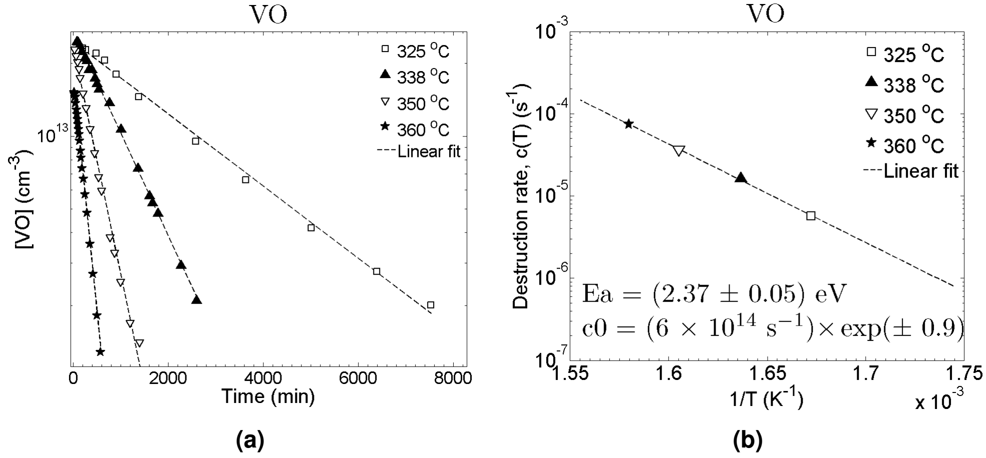

Figure 5.10: A plot of $\ln[\mathrm{VO}]$ vs. time, with a linear least squares fit **(a)**. The linear fit is near perfect, indicating first order annealing kinetics. $\ln c(T)$ is plotted vs. $1/T$ to determine the activation energy of the reaction **(b)**. The value of c_0 indicates dissociation as the main annealing mechanism.

reference [24], where dissociation is found to be the dominating annealing mechanism for V_2O in both DOFZ and MCz.

The logarithm of [VO] is plotted vs. time in figure 5.10(a) for all of the four isothermal measurement series performed in this thesis. The data are closely fitted by linear least squares over more than an order of magnitude, with the exception of the increasing part in the early stages. This indicates that the annealing of [VO] follows first order kinetics. Then

$$c(T) = c_0 \exp(-E_a/kT)$$

and the logarithm of the annealing rate, $\ln c(T)$, is plotted vs. $1/T$ in figure 5.10(b) and it is very close to linear. The activation energy and the pre–exponential factor are determined to

$$E_a = (2.37 \pm 0.05)\ \mathrm{eV}$$
$$c_0 = (6 \times 10^{14}) \times \exp(\pm 0.9)\ \mathrm{s}^{-1}$$

where the uncertainty (standard deviation) in c_0 amounts to a factor of 3 or $\frac{1}{3}$, respectively. This is considered to be rather good since pre–exponential factors are notoriously difficult to determine with good accuracy. A value of c_0 on the order of $10^{13}\ s^{-1}$ or larger is considered to be an indication of dissociation, as explained in section 3.1.5. The large value of c_0 measured here indicates that dissociation is the dominant first order process for the annealing of VO, but it is likely that there also is a contribution from the formation of VO_2 and VOH.

Svensson et al. [41] found in a Fourier transform infrared spectroscopy (FTIR) study that two different processes were causing the annealing of VO in Cz–Si with $[\mathrm{O}_i] \sim 7 \times 10^{17}\ \mathrm{cm}^{-3}$. The overall activation energy for the annealing was measured for six samples and the results for all the samples were within 2.27 ± 0.05 eV. c_0 was measured to $1.6 \times 10^{15}\ \mathrm{s}^{-1}$.

The two processes were suggested to be migration of VO and subsequent formation of VO_2 with activation energy $E_a = 2.06$ eV, and dissociation of VO with $E_a = 2.51$ eV. By comparing these measurements with the activation energy measured here, $E_a = 2.37 \pm 0.05$ eV, it seems that dissociation is even more important in this material. This is also intuitively correct, since this material has a lower oxygen concentration than that which was investigated in reference [41], so the generation of VO_2 from $VO + O_i \rightarrow VO_2$ should have a lower probability in this material. Unfortunately, electrically inactive defects such as VO_2 can not be measured by DLTS, so it is not possible to determine how this really affects the concentration of VO.

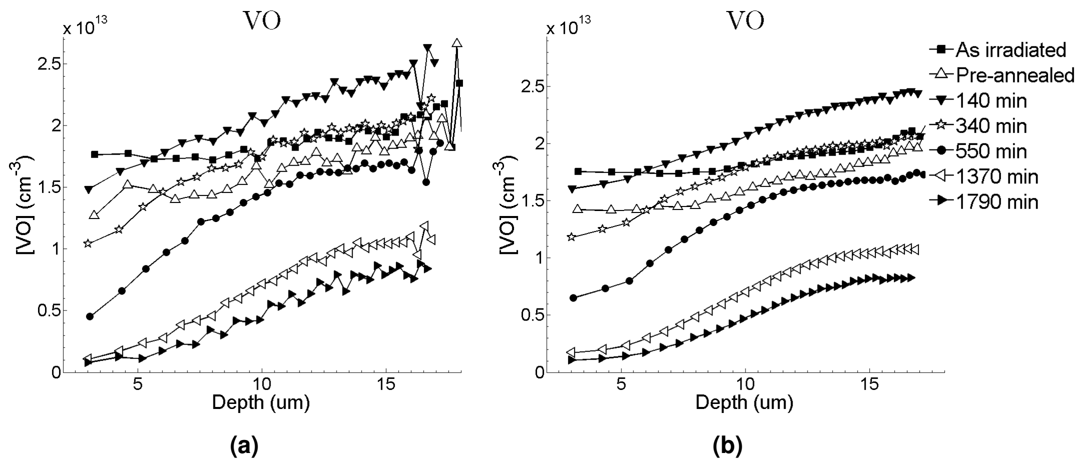

Figure 5.11: The depth profile of VO measured after isothermal annealing at 338 °C unsmoothed **(a)** and smoothed by a running average over 5 points **(b)**.

The concentration of VO as a function of depth is monitored at various stages of the isothermal annealing at 338 °C, as shown in figure 5.11. All the concentration profiling in this work is done using the 640 ms lock–in rate window, a constant reverse bias of -16 V and by varying the pulse voltage from 0 – 16 V in 0.5 V steps. The λ–effect is taken into account as explained in section 4.2.4. Otherwise the profile will be significantly distorted and may not display the real properties. Conversely, it may show false tendencies. The amount of noise makes it necessary to use a running average to increase the readability of the profiles, but the unsmoothed profiles are also presented for comparison.

The profile in the as–irradiated condition shows an almost entirely uniform concentration with a small decreasing tendency towards the surface. A uniform concentration is expected since monovacancies are created uniformly through the sample by electron radiation, and $[O_i]$ is many orders of magnitude larger. Thus, the non–uniform distribution of oxygen does not influence the resulting distribution of VO.

[VO] decreases slightly during the pre–annealing, and it also develops a slightly decreasing tendency towards the surface. Then, [VO] increases until after 140 min at 338 °C when it is close to the overall maximum concentration. At this point the profile has a very clear decreasing tendency towards the surface. [VO] increases much less near the surface than in the bulk. This may imply that some of the VO centers generated from $V_2O \rightarrow V + VO$ are lost in some reaction in the surface region. The species which reacts

with VO at the surface should have a concentration profile which increases towards the surface. It must also have a concentration which is comparable to or smaller than [VO]. Otherwise [VO] would be the limiting reactant factor and [VO] would decrease with the same rate at all depths. Hydrogen is an impurity which is expected to fulfill both of these criteria as illustrated in figure 5.1. The concentrations of oxygen and carbon are far too large to have any influence on the distribution of VO. Thus, it is likely that a fraction of VO reacts with H, according to VO + H → VOH, and this decreases [VO] near the surface.

The decreasing tendency of the profile towards the surface continues while the overall concentration of VO decreases for annealing times 140 – 1790 min over all depths. The concentration of VO decreases with about the same rate for all depths. This indicates that VO is dissociating, since the loss of VO by dissociation would not depend on the distribution of VO or any other defect. However, the same would be true for the reaction of VO with an impurity with a large concentration, such as in the creation of VO_2, so this is not a conclusive argument for dissociation as such.

To summarize, based on the measured values of E_a and c_0, it is argued that the dominant process for the annealing of VO is dissociation, in addition to the production of VOH and probably VO_2. The creation of VOH through VO + H → VOH is concluded to be a contributing process to the destruction of VO based on the decrease of the concentration profile of VO near the surface. This will be further discussed in section 5.4.3.3.

5.4.3.2 V_2 and V_2O

V_2 is created during and immediately after irradiation, either when a single incident particle creates a V_2 complex directly or when two monovacancies migrate and create a pair. During post–irradiation annealing, V_2O is created from V_2 through the reaction

$$V_2 + O_i \rightarrow V_2O \tag{5.5}$$

as explained in section 3.3.2. V_2O can dissociate into

$$V_2O \rightarrow V + VO \tag{5.6}$$

at a sufficiently high temperature.

The rate of the annealing of V_2 and the simultaneous growth of V_2O can be calculated from the pre–annealing data in figure 5.7. Table 5.5 is a comparison between the annealing rate of V_2 in materials with different oxygen concentrations. The annealing rate is taken only from references where the transition $V_2 \rightarrow V_2O$ was observed, since otherwise V_2 is annealing through some other mechanism with an annealing rate which could be completely independent of [O]. An alternative annealing process is the formation of V_2H_n instead of V_2O. As can be seen from the table, the annealing rate increases with increasing [O], although the exact form of the dependency is difficult to determine due to the large uncertainty in the measured values for [O]. Note also that $c(T)$ as measured by Mikelsen et al. is somewhat higher than the value found by Alfieri et al. in materials

Material	[O] (cm^{-3})	Reaction rate of V_2 at 250 °C (s^{-1})	Reference
DOFZ	$(2-3) \times 10^{17}$	$(1-2) \times 10^{-4}$	Mikelsen et al. [26]
DOFZ	$(2-3) \times 10^{17}$	$(3.5-5.5) \times 10^{-5}$	Alfieri et al. [2]
FZ	$(1-3) \times 10^{17}$	$(3-5) \times 10^{-5}$	Alfieri et al. [2]
EPI	$\leq 2 \times 10^{17}$	$(3-4) \times 10^{-5}$	Calculated from figure 5.7
FZ	$(1-2) \times 10^{16}$	$(4-6) \times 10^{-6}$	Alfieri et al. [2]
MCz	–	–	No references found.

Table 5.5: Comparison of the reaction rate for $V_2 + O_i \rightarrow V_2O$ as a function of oxygen concentration. The materials are sorted by oxygen concentration. The annealing rate increases with increasing [O], although it is difficult to determine the form of the dependency due to the high uncertainty in the measured oxygen concentration.

with the same reported oxygen concentration. A possible reason for this is that the concentration of hydrogen was larger in the samples studied by Mikelsen et al. , and thus the creation of V_2H_n would contribute more to the annealing of V_2.

The transformation rate of V_2 into V_2O in this EPI–Si material with [O] $\leq 2 \times 10^{17}$ cm^{-3} is comparable to that in FZ– and DOFZ–Si with [O] $\sim (1-3) \times 10^{17}$ cm^{-3}. This indicates that the oxygen concentration in this EPI–Si material is not much lower than 1×10^{17} cm^{-3}, which is the lower limit for [O] in the FZ material in table 5.5.

Whether V_2O anneals out primarily through migration and reaction with some other species, or by dissociation depends on the activation energies of these processes. The process with the smallest E_a will dominate. Mikelsen et al. concluded in reference [24] that V_2O most likely anneals out by dissociation in the DOFZ–Si studied in that article. The activation energy for this dissociation was determined to be $E_a = 2.02 \pm 0.12$ eV and the frequency factor was $c_0 = 2 \times 10^{13}$ s^{-1} with about one order of magnitude of uncertainty. Indeed, the value of c_0 suggests that dissociation of V_2O is the main annealing process.

$\ln[V_2O]$ is plotted vs. time in figure 5.12(a) for the EPI samples studied in this work. [V_2O] is based on the $V_2O^{=/-}$ peak, because the peak at the position of $V_2O^{-/0}$ contains some minor, overlapping defects since it has a larger amplitude than $V_2O^{=/-}$. The linear fit is near perfect, so the annealing of V_2O is clearly of first order with activation energy

$$E_a = (1.95 \pm 0.22) \text{ eV}$$

and pre–exponential factor

$$c_0 = 4 \times 10^{12} \times \exp(\pm 4) \text{ s}^{-1}$$

where the uncertainty of $\exp(\pm 4)$ amounts to a factor of 50 or $\frac{1}{50}$, respectively. Only three measurements of V_2O during the isothermal treatment at 350 °C were performed, and this makes the standard deviation large. This is because the annealing rate of V_2O at this temperature was larger than originally anticipated. Nonetheless, the linear fits are excellent at all the temperatures, suggesting that the measurements are actually quite close

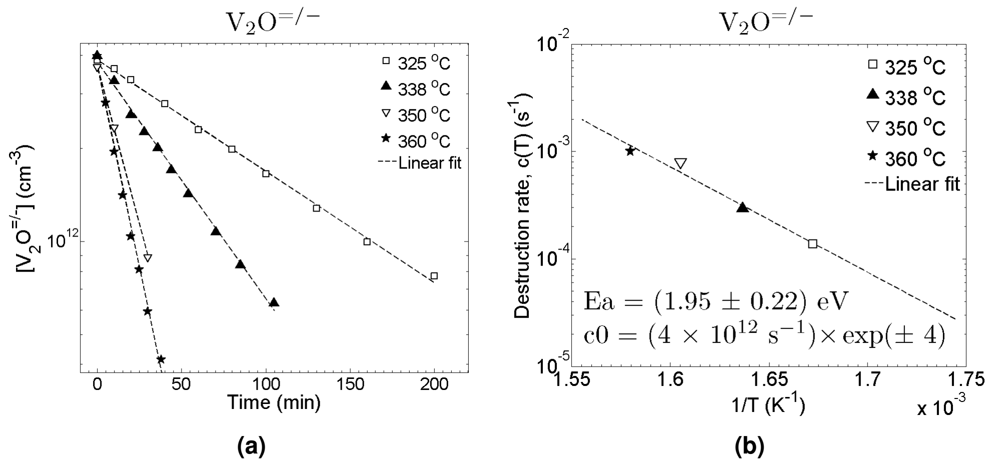

Figure 5.12: A plot of $\ln[V_2O]$ vs. time, with a linear least squares fit **(a)**. The linear fit is near perfect, indicating first order annealing kinetics. $\ln c(T)$ is plotted vs. $1/T$ to determine the activation energy of the reaction **(b)**. The large value of c_0 suggests dissociation as the main annealing mechanism. These data are from the $V_2O^{=/-}$ peak.

to the real values. The value of c_0 suggests that V_2O is mainly disappearing by dissociation. These results are in good agreement with $E_a = (2.02 \pm 0.12)$ eV and 2×10^{13} s^{-1} from reference [24].

The concentration of V_2 vs. depth is uniform in the as–irradiated condition since V_2 is created uniformly by MeV electron radiation. V_2O is created during post-irradiation annealing through $V_2 + O_i \rightarrow V_2O$, so $[V_2O]$ should also be uniform since $[O_i]$ is many orders of magnitude higher than $[V_2]$. These claims are confirmed by the profile in figure 5.13 for $[V_2^{=/-}]$ and $[V_2O^{=/-}]$, and in figure 5.14 for $[V_2^{-/0}]$ and $[V_2O^{-/0}]$. The concentrations of $V_2^{-/0}$ and $V_2O^{-/0}$ are slightly higher than that of $V_2^{=/-}$ and $V_2O^{=/-}$, because of the minor overlapping defects discussed above.

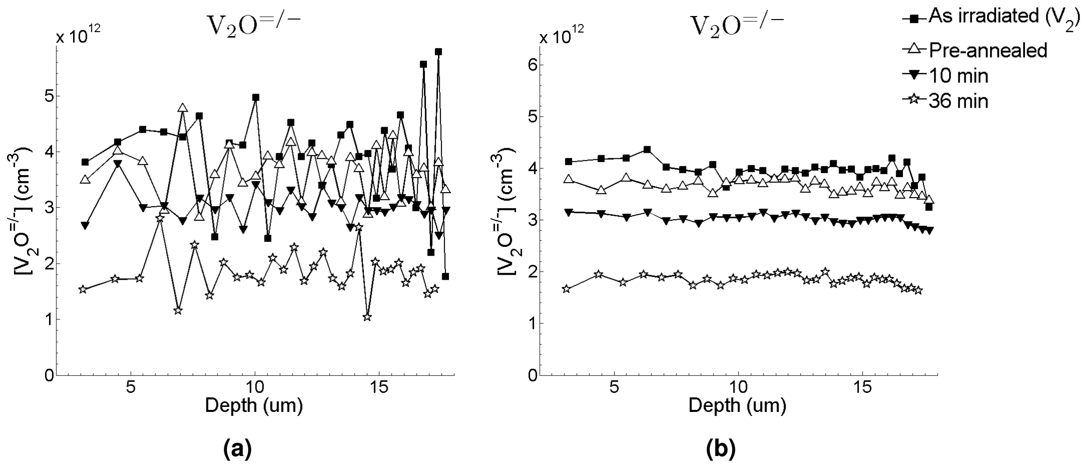

Figure 5.13: The depth profile of V_2O measured at 109 K during the isothermal annealing at 338 °C unsmoothed **(a)** and smoothed by a running average over 5 points **(b)**.

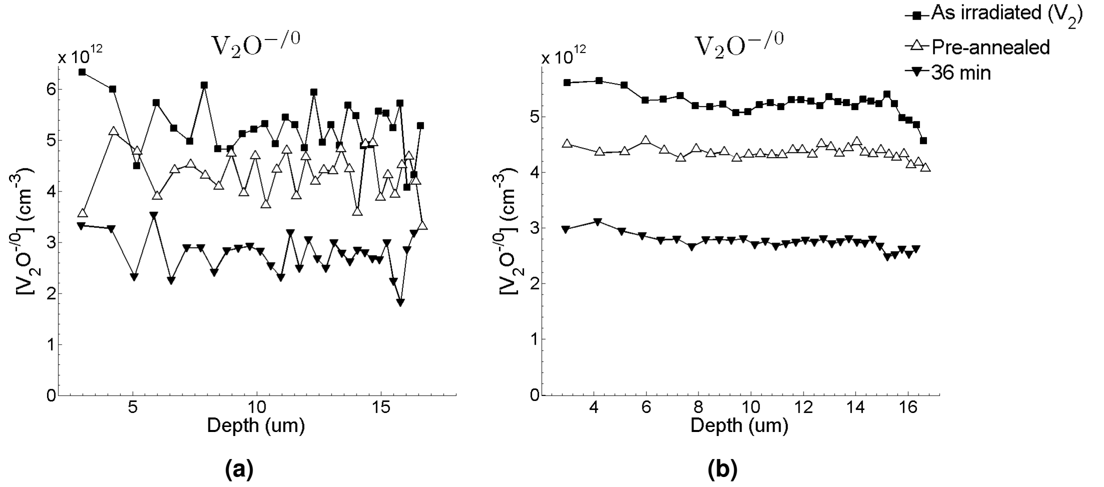

Figure 5.14: The depth profile of V_2O measured after isothermal annealing at 338 °C unsmoothed **(a)** and smoothed by a running average over 5 points **(b)**.

The uniform concentration of V_2O decreases at the same rate at all depths. The concentration profile of V_2O is essentially the same when measured at the $V_2O^{=/-}$ and the $V_2O^{-/0}$ peak, taking the overlapping peaks into account. A significant feature of the profile of V_2O is the lack of any deviations from a uniform distribution during the annealing until 36 min when V_2O disappears. This means that until this time any significant formation of V_2OH or V_2OH_2 can almost certainly be ruled out since this would show as a decrease in the V_2O profile near the surface.

The lack of any decrease in the concentration close to the surface, may not be consistent with the hypothesis in section 5.3.2 of a possible hydrogen–assisted annealing of V_2O due to a larger annealing rate in more hydrogen–rich samples. In conclusion, V_2O is believed to mainly anneal by dissociation. However, a possible connection between the decay of V_2O and the growth of E(198 K) is discussed in section 5.4.5.2.

5.4.3.3 VOH

GROWTH

VOH is traditionally [24] believed to be created by

$$\mathrm{VO} + \mathrm{H} \rightarrow \mathrm{VOH} \tag{5.7}$$

The VO in the above reaction can also come from the dissociation of V_2O,

$$\mathrm{V_2O} \rightarrow \mathrm{VO} + \mathrm{O}_i \tag{5.8}$$

That is, VOH is produced either directly by trapping of a migrating H at VO, or from dissociation of V_2O and then trapping of hydrogen at the released VO.

The change in VOH concentration goes as

$$\frac{d[\mathrm{VOH}]}{dt} = 4\pi R(D_H + D_{VO})[\mathrm{H}][\mathrm{VO}] \approx 4\pi R D_H[\mathrm{H}][\mathrm{VO}]$$

where $D_H = c_0 \exp(-E_a/kT)$. This reaction must be driven by the release of H from the surface, or in other words the dissociation of HZ which follows

$$\frac{d[\text{HZ}]}{dt} = -c_{diss}[\text{HZ}]$$

The solution for [HZ] is

$$[\text{HZ}] = [\text{HZ}]_{t=0} \exp(-c_{diss}\, t)$$

Then the concentration of free hydrogen changes as

$$\frac{d[\text{H}]}{dt} = c_{diss}[\text{HZ}] - 4\pi R D_H [\text{H}][\text{VO}]$$

when hydrogen is assumed to mainly be consumed by the creation of VOH at these annealing temperatures. Since H has a large diffusion coefficient, D_H, in silicon, it is reasonable to expect that H migrates very rapidly to and reacts with VO. Thus, $d[\text{H}]/dt \approx 0$ and

$$c_{diss}[\text{HZ}] \approx 4\pi R D_H [\text{H}][\text{VO}]$$

Hence, the generation rate of VOH is approximately equal to the dissociation rate of HZ, since

$$\frac{d[\text{VOH}]}{dt} = 4\pi R D_H [\text{H}][\text{VO}] \approx c_{diss}[\text{HZ}]$$

The solution is found by inserting for [HZ] and integrating, so the concentration of VOH follows

$$[\text{VOH}] = [\text{VOH}]_{max} - a_0 \exp(-c_{diss}\, t)$$

where a_0 and c_{diss} are constants to be determined in a linear least squares fit of $\ln\big([\text{VOH}]_{max} - [\text{VOH}]\big)$ versus time. Hence, a plot of this quantity is linear as a function of time and c_{diss} is the slope, since

$$\ln\big\{[\text{VOH}]_{max} - [\text{VOH}]\big\} = \ln a_0 - c_{diss}\, t$$

where $c_{diss}(T) = c_0 \exp(-E_a/kT)$.

$\ln\big([\text{VOH}]_{max} - [\text{VOH}]\big)$ is plotted vs. time in figure 5.15. The linear least squares fits describe the experimental data very well for 350 and 360 °C, and slightly less well for 325 and 338 °C. The activation energy for the growth of VOH is found to be

$$E_a = (2.12 \pm 0.20)\ \text{eV}$$

and the pre–exponential factor is

$$c_0 = (3 \times 10^{13}\ \text{s}^{-1}) \times \exp(\pm 4)$$

The uncertainty $\exp(\pm 4)$ translates into a factor of about 50 or $\frac{1}{50}$, respectively. This value for c_0 strongly supports the claim that the measured growth rate of VOH is effectively the dissociation rate of HZ due to the rapid migration of H.

DECAY

$\ln[\text{VOH}]$ is plotted vs. time in figure 5.16 for the decay of VOH. Just as for the growth, the linear least squares fit of the experimental data is very good for 350 and 360 °C, but

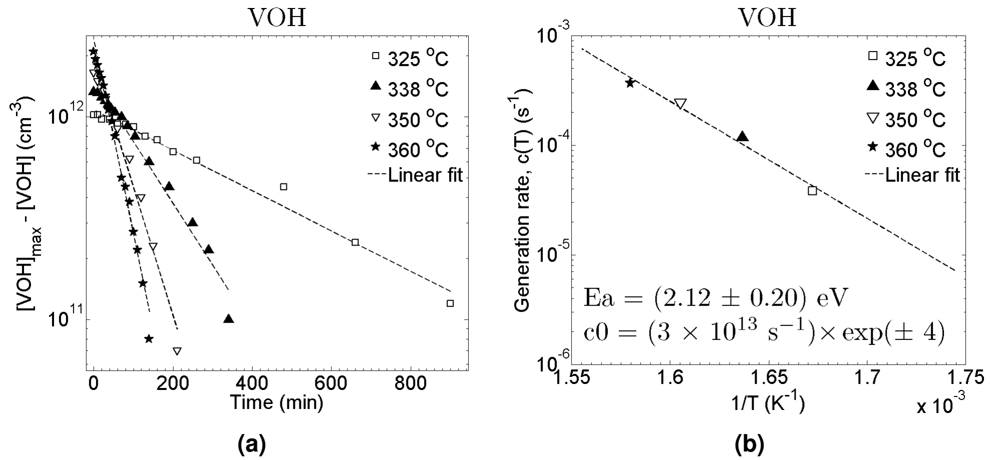

Figure 5.15: A plot of $\ln\left\{[\text{VOH}]_{max} - [\text{VOH}]\right\}$ vs. time for the growth of VOH, with a linear least squares fit **(a)**. The linear fit is best at 350 and 360 °C. $\ln c_{diss}$ is plotted vs. $1/T$ to determine the activation energy of the reaction **(b)**.

rather poor for 325 and 338 °C. The activation energy for the decay of VOH is determined to be

$$E_a = (2.51 \pm 0.20) \text{ eV}$$

and the pre–exponential factor is

$$c_0 = (5 \times 10^{15} \text{ s}^{-1}) \times \exp(\pm 4)$$

with the same uncertainty as the measurements for the growth of VOH.

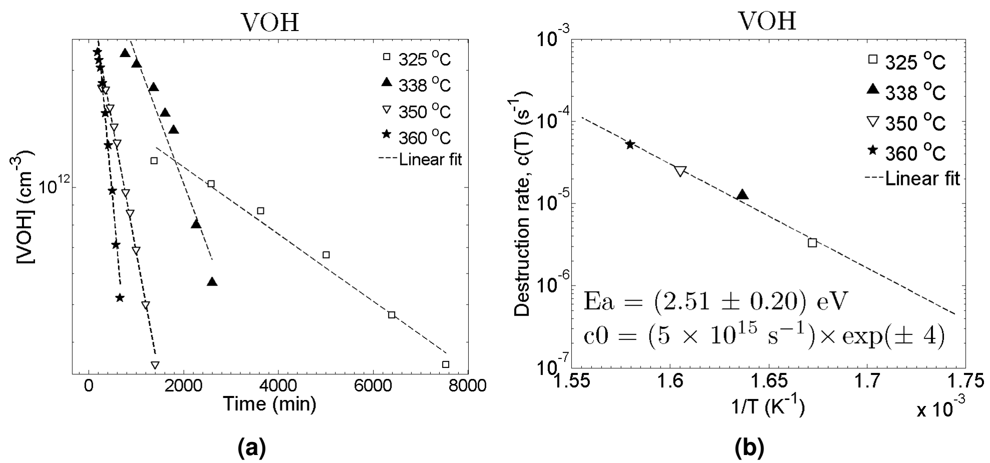

Figure 5.16: A plot of $\ln[\text{VOH}]$ vs. time for the decay of VOH, with a linear least squares fit **(a)**. The linear fit is best at 350 and 360 °C, but overall it indicates first order kinetics. $\ln c(T)$ is plotted vs. $1/T$ to determine the activation energy of the reaction **(b)**.

The concentration of VOH as a function of depth is shown in figure 5.17. The VOH profile could only be measured after about 140 min when [VOH] was so high that the overlap with the L–center and E(170 K) was negligible. The profile at 140 min has a

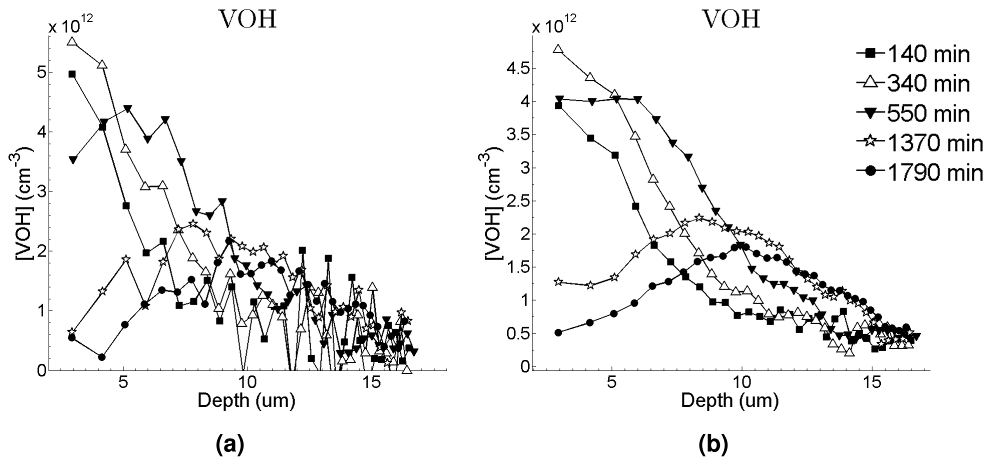

Figure 5.17: The depth profile of VOH measured after isothermal annealing at 338 °C unsmoothed **(a)** and smoothed by a running average over 5 points **(b)**.

diffusion–like shape with a sharp drop in concentration from the surface and towards the bulk. The concentration increases at the surface between 140 – 340 min, whereas the concentration in the bulk remains low. From 340 – 550 min the concentration decreases slightly near the surface, while it still increases between the surface and the bulk. The concentration remains very low in the bulk. The overall concentration is at the maximum at 550 min. From 550 – 1790 min the surface concentration drops to be comparable to the concentration in the bulk. The profile now has a gaussian–like bell shape with a maximum at $\sim$10 μm, which is approximately in the middle of the measured depth range.

[VOH] is changing mostly at the surface, both during growth and decay. This may indicate the involvement of hydrogen in the decay, and the process VOH + H $\rightarrow$ VOH_2 is proposed. This would explain that the concentration decreases faster in the surface region, and also that no electrically active defects are created during the decay of VOH. VOH_2 is thought to be electrically inactive since it has no dangling bonds [32]. This is the same conclusion as Pellegrino et al. made for the loss of VO through the production of VOH and VOH_2 in reference [33]. The production of VOH can continue until the supply of VO or H, from HZ, is depleted. At this time VOH will start to disappear and possibly be converted into the electrically inactive VOH_2 as suggested.

The profiling does not exclude that dissociation also takes place, but the fact that no other electrically active defects appear during the decay of VOH supports the suggested formation of VOH_2. It is impossible to determine the individual contributions from dissocation and the presumed formation VOH_2 without separate measurements of VOH_2 by some non–electrical method. An alternative annealing mechanism for VOH is the previously mentioned annealing mechanism for VO where VOH dissociates as VOH $\rightarrow$ VO + H and the released VO is trapped at O_i and forms VO_2. Thus, VO is lost to VO_2 and the amount of VO left to reform VOH through VO + O_i $\rightarrow$ VOH decreases.

In the modeling in the next section the initial concentrations of HZ and O_i are used as free

parameters to acquire a good fit to the experimental data. It is shown that

$$[\text{O}_i]_{t=0} \approx [\text{O}_i] \approx 1 \times 10^{17}\ \text{cm}^{-3}$$
$$[\text{HZ}]_{t=0} \approx 1 \times 10^{13}\ \text{cm}^{-3}$$

give a close match. This is a reasonable value for $[\text{O}_i]$ since the upper limit was determined by SIMS to be $\lesssim 2\times10^{17}$ cm^{-3}. The maximum concentration of VOH is measured to $[\text{VOH}]_{max} \approx 2 \times 10^{12}$ cm^{-3} at all the annealing temperatures. This is quite close to $[\text{HZ}]_{t=0} = 10^{13}$ cm^{-3} considering the rather large uncertainty in this value and accounting for the generation of VOH_2 through $\text{VOH} + \text{H} \rightarrow \text{VOH}_2$ occuring simultaneously as the generation of VOH.

Thus, it is claimed that VOH is formed through $\text{VO} + \text{H} \rightarrow \text{VOH}$ with the same growth rate as the annealing rate of HZ, and that it decays mainly due to $\text{VOH} + \text{H} \rightarrow \text{VOH}_2$.

5.4.4 Modeling of reactions

The reactions in (5.9) – (5.17) must be solved simultaneously to model the annealing processes for VO, V_2O and VOH. HZ is included as the assumed hydrogen source which releases H by dissociating. These reactions translate into the system of coupled, first order, linear differential equations listed in table 5.6. The equations are solved in Matlab for the temperatures 325 – 360 °C using the parameters listed in table 5.7. The results from the modeling are shown in figure 5.18.

$$\text{V} + \text{O}_i \rightarrow \text{VO} \quad (5.9)$$

$$\text{VO} \rightarrow \text{V} + \text{O}_i \quad (5.10)$$

$$\text{V}_2\text{O} \rightarrow \text{VO} + \text{V} \quad (5.11)$$

$$\text{VO} + \text{O}_i \rightarrow \text{VO}_2 \quad (5.12)$$

$$\text{VO} + \text{H} \rightarrow \text{VOH} \quad (5.13)$$

$$\text{VOH} \rightarrow \text{VO} + \text{H} \quad (5.14)$$

$$\text{VOH} + \text{H} \rightarrow \text{VOH}_2 \quad (5.15)$$

$$\text{HZ} \rightarrow \text{H} + \text{Z} \quad (5.16)$$

$$\text{Z} + \text{H} \rightarrow \text{HZ} \quad (5.17)$$

The results from the model match the measured concentrations at all temperatures closely, although the fit is slightly better at the intermediate temperatures 338 and 350 °C than at 325 and 360 °C. O_i is assumed to be immobile compared to H, V and VO. Svensson et al. calculated the diffusion coefficient for O_i to $D_{O_i} = 5.0 \times 10^{-22}$ cm^2/s at 350 °C, which is 6 orders of magnitude smaller than D_{VO} at the same temperature [41].

The growth of VOH is thought to be activated by the dissociation of the assumed hydrogen trap HZ. $[\text{O}_i]_{t=0}$ and $[\text{HZ}]_{t=0}$ are treated as free parameters. It is found that the model

agrees well with the measurements when $[\mathrm{O}_i]_{t=0} \approx 10^{17}$ cm^{-3} with about 15% variation and $[\mathrm{HZ}]_{t=0} \approx 10^{13}$ cm^{-3} with about 55% variation between the four samples. This relatively low concentration of hydrogen could explain the low maximum concentration of VOH and the high temperature when VOH is detected in the isochronal measurements. In this study VOH anneals in at 375 °C in the isochronal measurements in figure 5.3, compared to 250–300 °C in reference [33] where the hydrogen trap is assumed to have an initial concentration of $\sim 10^{14}$ cm^{-3} in the p^+ region.

This model assumes that the defects are uniformly distributed. To account for non–uniform distributions, each differential equation in table 5.6 must include a term for changes in the depth distribution, and initial depth profiles must be supplied for each species. In this case, the equation for e.g. HZ is

$$\frac{\partial[\mathrm{HZ}(x,t)]}{\partial t} = -C_{HZ}[\mathrm{HZ}] + 4\pi R D_H[\mathrm{H}][\mathrm{Z}] + D_{HZ}\frac{\partial[\mathrm{HZ}(x,t)]}{\partial x^2}$$

where the first two terms account for the loss and gain of HZ through diffusion–limited reactions, and the second term is the law of diffusion which accounts for the change in the depth distribution of HZ. An example of a model which takes this into account is in Pellegrino et al. [33]. Clearly, this is most important for defect species with a large diffusion coefficient, such as H, or a highly non–uniform profile, such as HZ and VOH.

5.4.5 Unidentified levels

Two unidentified peaks appear in the DLTS spectra from the isothermal measurements shown in figure 5.8. These peaks are labeled E(170 K) and E(198 K) and they are investigated more closely in this section.

5.4.5.1 E(170 K)

The electrical properties of E(170 K) are determined as

$$\Delta H = (0.34 \pm 0.01)\ \text{eV}$$

for the enthalpy and

$$\sigma_{na} = (8 \pm 6) \times 10^{-16}\ \text{cm}^2$$

for the apparent capture cross section, as explained in section 5.3.1. Specifically, $\Delta H = 0.34$ eV and $\sigma_{na} = 7 \times 10^{-16}$ cm^2 give a perfect fit to all measurements. The concentration is found by fitting of the DLTS spectra. The peak appears at ∼325 °C in the isochronal annealing in figure 5.3. At 350 °C the E(170 K) peak reaches a maximum amplitude which is about 60% of the initial amplitude of $\mathrm{V}_2^{=/-}$, and then it disappears at 375–400 °C.

The growth of E(170 K) can not be studied in the temperature range 325 – 360 °C due to the very rapid increase of the peak at these temperatures. The decay of the peak is studied from the annealing time when [E(170 K)] is at the maximum and until the concentration

Defect	Equation
VO	$\frac{d[\text{VO}]}{dt} = C_{V_2O}[\text{V}_2\text{O}] - C_{VO}[\text{VO}] + 4\pi R\Big\{D_V[\text{V}][\text{O}_i] - D_{VO}[\text{VO}][\text{O}_i] - D_H[\text{H}][\text{VO}]\Big\}$
V_2O	$\frac{d[\text{V}_2\text{O}]}{dt} = -C_{V_2O}[\text{V}_2\text{O}]$
V	$\frac{d[\text{V}]}{dt} = C_{V_2O}[\text{V}_2\text{O}] + C_{VO}[\text{VO}] - 4\pi R D_V[\text{V}][\text{O}_i]$
VOH	$\frac{d[\text{VOH}]}{dt} = -C_{VOH}[\text{VOH}] + 4\pi R\Big\{D_H[\text{H}][\text{VO}] - D_H[\text{H}][\text{VOH}]\Big\}$
H	$\frac{d[\text{H}]}{dt} = C_{HZ}[\text{HZ}] - 4\pi R\Big\{D_H[\text{H}][\text{Z}] + D_H[\text{H}][\text{VO}] + D_H[\text{H}][\text{VOH}]\Big\}$
HZ	$\frac{d[\text{HZ}]}{dt} = -C_{HZ}[\text{HZ}] + 4\pi R D_H[\text{H}][\text{Z}]$
Z	$\frac{d[\text{Z}]}{dt} = C_{HZ}[\text{HZ}] - 4\pi R D_H[\text{H}][\text{Z}]$

Table 5.6: The differential equations corresponding to the reactions (5.9) – (5.17). This model is based on the model in reference [24], but the number of equations is reduced to include only those processes that are strictly needed to obtain a good match with the measured data for VO, V_2O and VOH. It is not necessary to keep track of the concentrations of O_i, VO_2 and VOH_2.

Parameter	Value	Comment
R	5 Å	Used the same R for all reactions.
C_{VO}	$(6 \times 10^{14}) \times \exp(-2.37/kT)$ s^{-1}	Measured, see figure 5.10.
C_{V_2O}	$(3 \times 10^{12}) \times \exp(-1.94/kT)$ s^{-1}	Within uncertainty of measured value in figure 5.12.
C_{HZ}	$(3 \times 10^{12}) \times \exp(-2.11/kT)$ s^{-1}	Assumed to be identical to the measured growth rate of VOH in figure 5.15 within uncertainty.
C_{VOH}	$(9 \times 10^{15}) \times \exp(-2.50/kT)$ s^{-1}	Within uncertainty of measured value in figure 5.16.
D_{VO}	$23.1 \times \exp(-2.06/kT)$ cm^2/s	Taken from reference [41].
D_V	$(10^6 \times D_{VO})$ cm^2/s	Simply assumed to be large.
D_H	$(5 \times 10^{-3}) \times \exp(-0.8/kT)$ cm^2/s	Taken from reference [33].
D_{O_i}	0	Assumed to be immobile.
$[VO]_{t=0}$	$\sim 2 \times 10^{13}$ cm^{-3}	Measured at $t = 0$, varies ∼40% between the samples.
$[V_2O]_{t=0}$	$\sim 3.5 \times 10^{12}$ cm^{-3}	Measured at $t = 0$, varies ∼10% between the samples.
$[VOH]_{t=0}$	0	
$[V]_{t=0}$	0	
$[H]_{t=0}$	0	
$[O_i]_{t=0}$	$\sim 1 \times 10^{17}$ cm^{-3}	Free parameter. Varies about 15% between the samples.
$[HZ]_{t=0}$	$\sim 1 \times 10^{13}$ cm^{-3}	Free parameter. Varies about 55% between the samples.

Table 5.7: The parameters used in the model in table 5.6. The initial values of $[O_i]$ and [HZ] are the only free parameters which are varied to obtain the best possible fit, as shown in figure 5.18.

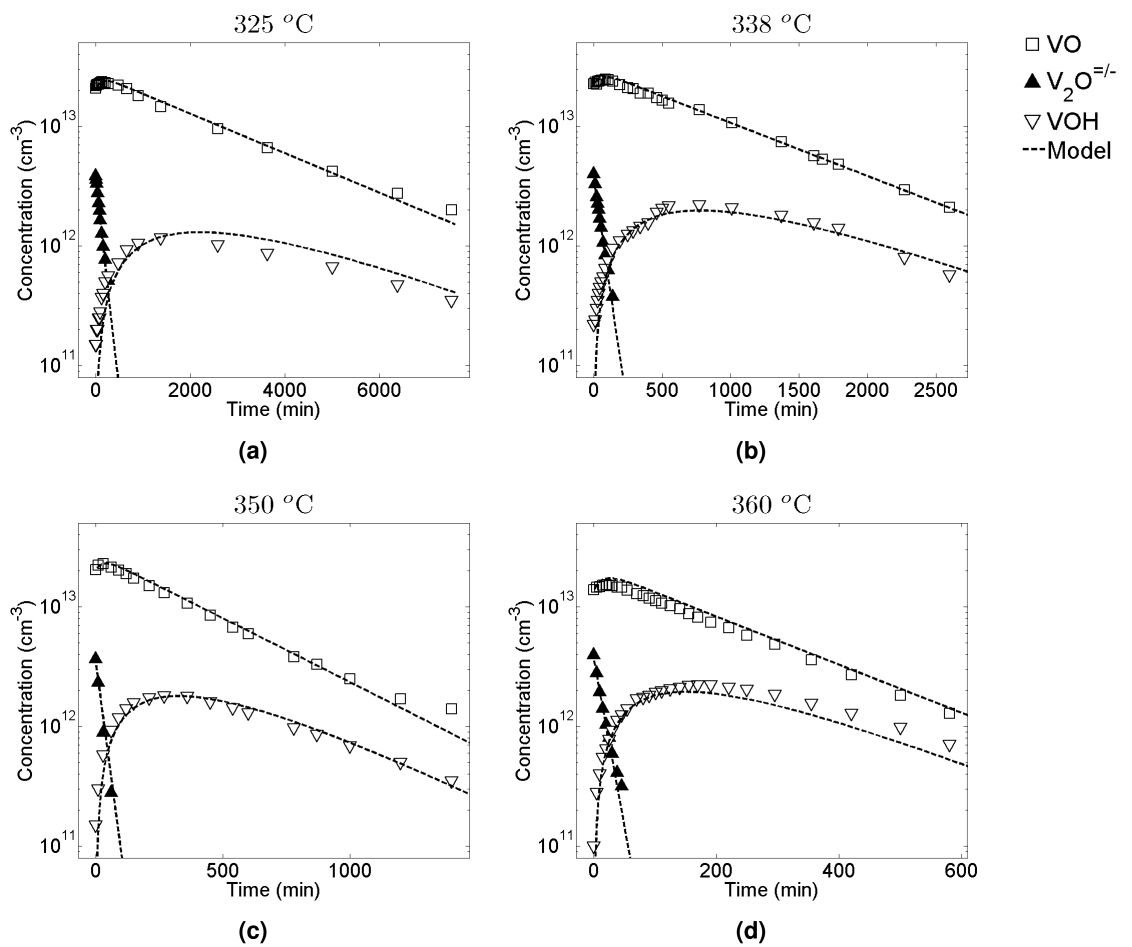

Figure 5.18: Modeling of the major known defects VO, V_2O and VOH at 325 °C **(a)**, 338 °C **(b)**, 350 °C **(c)** and 360 °C **(d)**.

reaches the detection limit of a few times 10^{11} cm^{-3}. The result is shown in figure 5.19(a). The logarithm of the concentration is relatively well fitted by linear least squares at all four temperatures. This means that E(170 K) anneals out by first order kinetics. The activation energy is found to be

$$E_a = (2.16 \pm 0.08)\ \text{eV}$$

and the pre–exponential factor is

$$c_0 = (4 \times 10^{13}\ \text{s}^{-1}) \times \exp(\pm 1)$$

with a rather small uncertainty for both quantities.

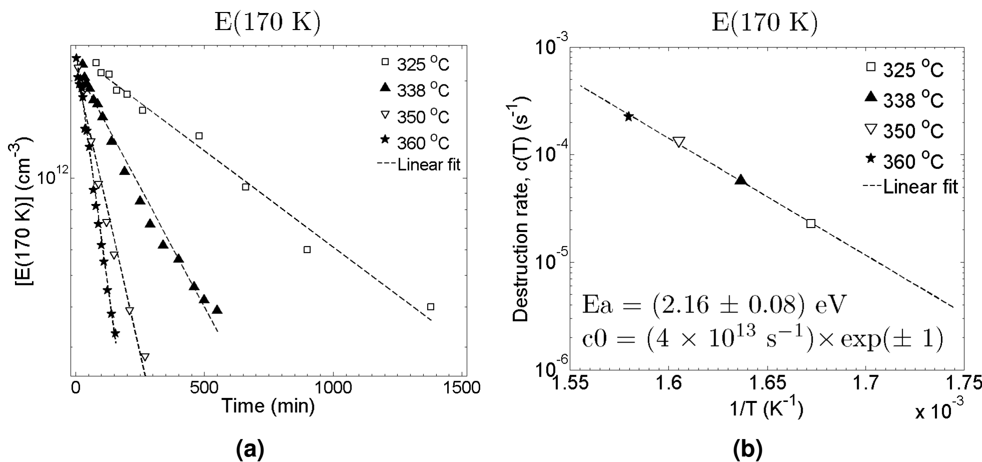

Figure 5.19: A plot of $\ln$[E(170 K)] vs. time for the decay of E(170 K), with a linear least squares fit **(a)**. The linear fit is decent at all four temperatures, and it indicates first order kinetics. $\ln c(T)$ is plotted vs. $1/T$ to determine the activation energy of the reaction **(b)**.

The concentration profile of E(170 K) is shown in figure 5.20. The unsmoothed profiles are very noisy despite being the average of 70–100 scans. The smoothed profiles show that the distribution remains uniform through the entire annealing process, from pre–annealed to 340 min. After this the concentration is too low to be measured properly. The uniformity of [E(170 K)] is significant since it virtually excludes any direct involvement of hydrogen both in the growth and decay of this defect. If E(170 K) reacts with hydrogen during growth or decay, then a similar profile as that of VOH in figure 5.17 is expected. In contrast, the profile of E(170 K) is relatively flat, much like the profiles of VO (initially), V_2 and V_2O.

The loss of E(170 K) is proportional to the growth of VOH, as shown in figure 5.21. The growth of VOH is calculated as

$$\text{Growth [VOH]} = \text{[VOH]} - \text{[VOH]}(t = 0)$$

and the loss of E(170 K) is

$$\text{Loss [E(170 K)]} = \text{[E(170 K)]}(t_{max}) - \text{[E(170 K)]}$$

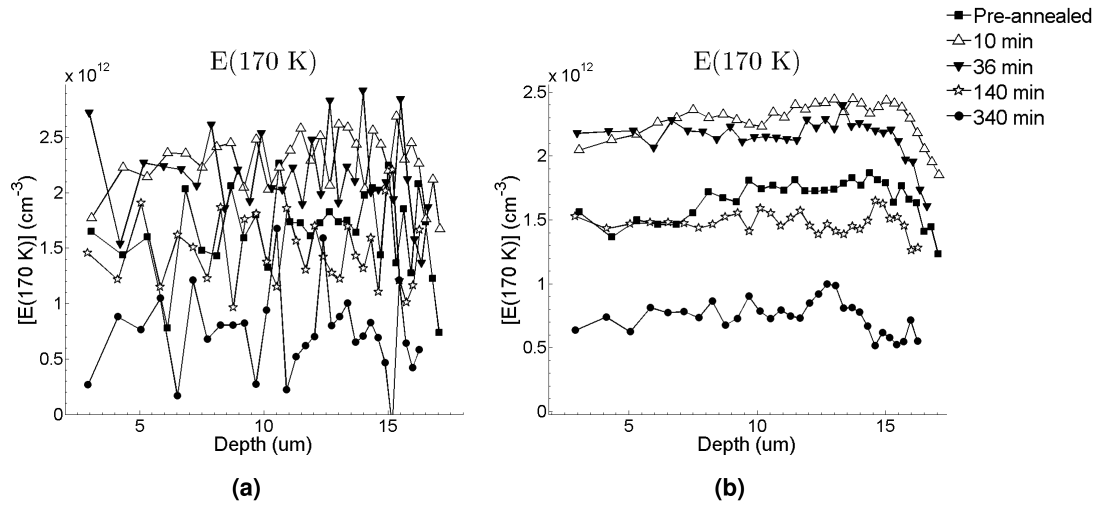

Figure 5.20: The depth profile of E(170 K) measured after isothermal annealing at 338 °C unsmoothed **(a)** and smoothed by a running average over 5 points **(b)**.

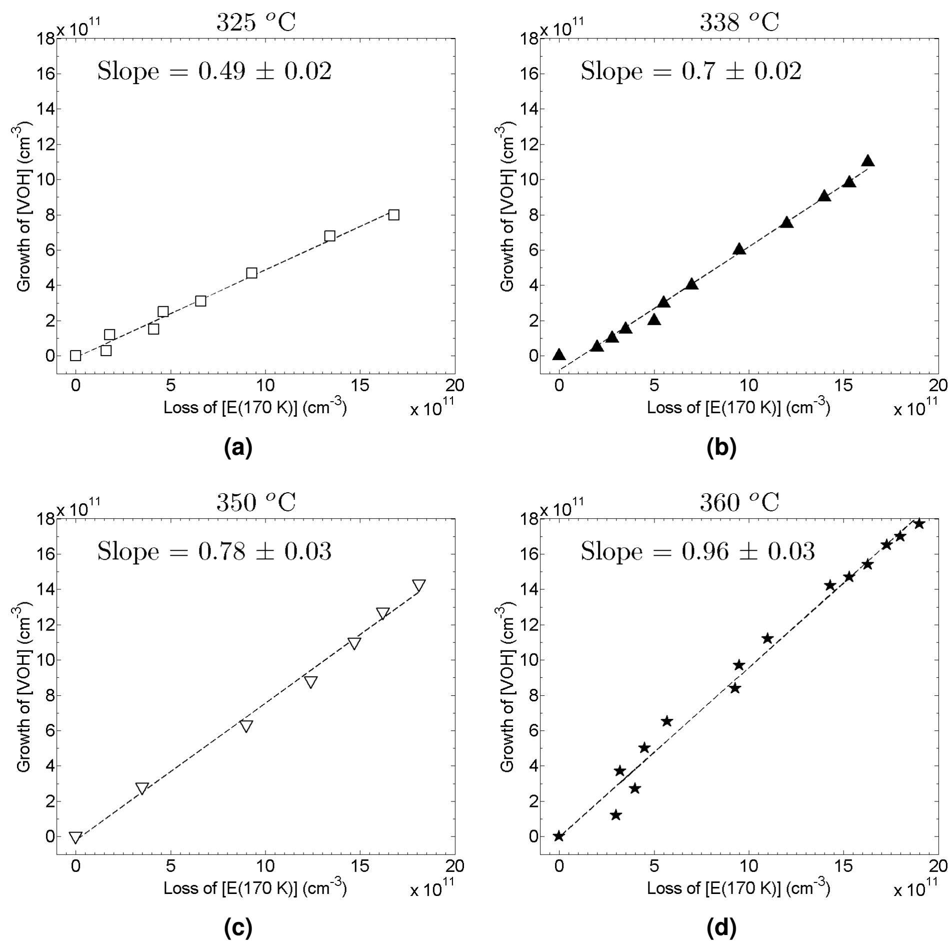

Figure 5.21: The growth of VOH plotted as a function of the decay of E(170 K).

where t_{max} is the time when the E(170 K) peak has the maximum amplitude before decreasing.

Note that VOH reaches its maximum concentration and starts to decrease just when the concentration of E(170 K) becomes too low to be measured, as can be seen in figure 5.9. The maximum concentration of E(170 K) is always larger than that of VOH for all temperatures 325 – 360 °C, and the ratio approaches unity at 360 °C.

These facts suggest that E(170 K) is involved in a reaction where VOH is created until E(170 K) is depleted. However, it was previously concluded that VOH is created by VO + H → VOH. In addition, the profile of E(170 K) indicates that there is no interaction with H during the entire annealing. This is regarded as a strong indication that VOH is not created in a reaction with E(170 K), but rather from VO as concluded in section 5.4.3.3.

Another explanation to the proportionality between the annealing rates of the growth of VOH and the decay of E(170 K)is that the processes are unrelated, but that they are both activated by the release of H from HZ. By assumption, H is released when HZ dissociates, e.g.

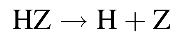

$$\text{HZ} \rightarrow \text{H} + \text{Z}$$

where Z contains everything which is not H in HZ. HZ may dissociate into a larger number of elements, but only Z is assumed here for simplicity. The released H can now react with VO to create VOH. Further, it is suggested that Z reacts with E(170 K) and that the reaction product is electrically inactive, in the following way

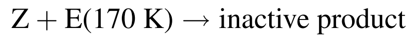

$$\text{Z} + \text{E(170 K)} \rightarrow \text{inactive product}$$

Hence, if Z has a large diffusivity in silicon, then the measured decay rate of E(170 K) is not the rate of the above reaction but rather the dissociation rate of HZ in the same way as for the growth rate of VOH as explained in section 5.4.3.3. This is because Z very rapidly migrates to and reacts with E(170 K), so

$$\frac{d[\text{Z}]}{dt} = c_{diss}[\text{HZ}] - 4\pi R D_Z [\text{Z}][\text{E(170 K)}] \approx 0$$

assuming $D_Z \gg D_{E(170\ K)}$. Then [E(170 K)] changes according to

$$\frac{d[\text{E(170 K)}]}{dt} = -4\pi R D_Z [\text{Z}][\text{E(170 K)}] \approx -c_{diss}[\text{HZ}] = \frac{d[\text{HZ}]}{dt}$$

In other words there is a one–to–one correspondance between the change in the overall concentrations of E(170 K) and HZ if this model is correct, although the depth profile of E(170 K) is uniform while HZ is expected to mainly be located at the surface.

The fact that the slope of the proportionality is less than unity at temperatures below 360 °C means that either the reaction

$$\text{VO} + \text{H} \rightarrow \text{VOH}$$

or

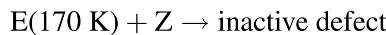

$$\text{E(170 K)} + \text{Z} \rightarrow \text{inactive defect}$$

is ineffective at lower temperatures than about 360 °C. The maximum concentration of E(170 K) is the same at all the annealing temperatures, whereas $[\text{VOH}]_{max}$ increases from about 50% to about 95% of $[\text{E(170 K)}]_{max}$ at 325 and 360 °C, respectively. This indicates that the generation rate of VOH relative to the destruction rate of E(170 K) is limited by the diffusion of H to react with the uniformly distributed VO, and that this limitation effectively disappears at temperatures higher than about 360 °C.

The suggested scenario explains the proportionality between the loss of E(170 K) and the growth of VOH, and the fact that E(170 K) can not be directly involved in a reaction with VOH because of the uniform depth profile. ΔH and σ_{na} for the growth of VOH and the decay of E(170 K) are equal within the experimental accuracy, which is a natural consequence of the suggested model. Possible candidates for Z are C_i, V and I_{Si}, since it must have a large diffusivity in silicon. H and O_i can be excluded for the same reason.

Simple dissociation of E(170 K) is an alternative explanation since c_0 is on the order of 10^{13} s^{-1}, but this does not explain the proportionality between [E(170 K)] and [VOH] which would then be a rather large coincidence. Hence, E(170 K) is claimed to disappear through a reaction with the non–hydrogen containing part of the dissociating HZ complex.

5.4.5.2 E(198 K)

ΔH and σ_{na} for E(198 K) are measured at all annealing times after $[V_2O^{=/-}] = 0$, as explained in section 5.3.1.2. The peak at 198 K is assumed to consist of only E(198 K) after this time. The activation enthalpy and apparent capture cross section is determined to

$$\Delta H = (0.46 \pm 0.02)\ \text{eV} \tag{5.18}$$

$$\sigma_{na} = (1.6 \pm 1.3) \times 10^{-14}\ \text{cm}^2 \tag{5.19}$$

Specifically, the values $\Delta H = 0.46$ eV and $\sigma_{na} = 2 \times 10^{-14}$ cm^2 are found to give a good fit to all measurements.

The growth of E(198 K) is calculated from the measured concentrations of $V_2O^{=/-}$ and $V_2O^{-/0}$ as

$$[\text{E(198 K)}] = [V_2O^{-/0}] - [V_2O^{=/-}] \tag{5.20}$$

from $t = 0$ and until $[V_2O^{=/-}]$ reaches the detection limit. After this point the peak at the position of $V_2O^{-/0}$ is assumed to consist of only E(198 K). Thus, the decay of E(198 K) is measured directly.

GROWTH

There is a slight discontinuity in [E(198 K)] at the measurement where $[V_2O^{=/-}]$ reaches the detection limit, as can be seen in figure 5.9. The reason is that V_2O has not yet annealed out completely, so the assumption that the peak at 198 K is pure E(198 K) is not fully valid for this measurement. Thus, the extracted [E(198 K)] becomes unreasonably

high at this annealing time and therefore this data point is neglected at each of the temperatures 325 – 360 °C.

The logarithm of [E(198 K)]$_{max}$ − [E(198 K)] is plotted in figure 5.22(a). The linear fit is far from perfect due to the noise in the measurements, but there is a rough agreement to

$$[\text{E(198 K)}] = [\text{E(198 K)}]_{max} - a_0 e^{-c(T)t}$$

or after rearranging

$$\ln\Big\{[\text{E(198 K)}]_{max} - [\text{E(198 K)}]\Big\} = \ln a_0 - c(T)t$$

There was unfortunately only made 4 measurements of V_2O yielding 3 values for the above expression during the annealing at 350 °C, because the annealing rate was larger than originally expected at this temperature, as previously mentioned.

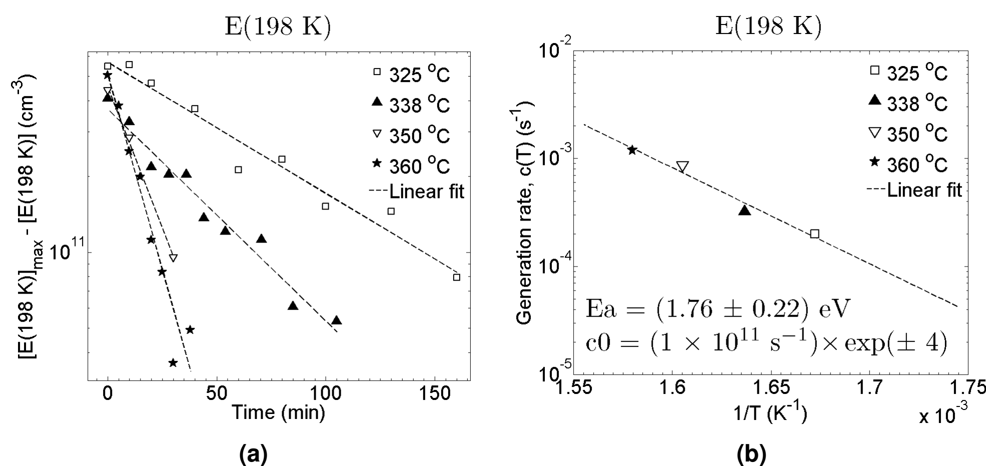

Figure 5.22: A semilogarithmic plot of [E(198 K)]$_{max}$ − [E(198 K)] vs. time for the growth of E(198 K), with a linear least squares fit **(a)**. The linear fit agrees roughly with the measurements at all four temperatures. $\ln c(T)$ is plotted vs. $1/T$ to determine the activation energy of the reaction **(b)**.

The activation energy for the growth is

$$E_a = (1.76 \pm 0.22)\text{ eV}$$

and the pre–exponential factor is

$$c_0 = (1 \times 10^{11}\text{ s}^{-1}) \times \exp(\pm 4)$$

where $\exp(\pm 4)$ translates into a factor of approximately 50 or $\frac{1}{50}$, respectively.

From figure 5.9 it can be seen that E(198 K) grows as V_2O anneals out, since the difference between [$V_2O^{=/-}$] and [$V_2O^{-/0}$] increases during the annealing. [E(198 K)] is at a maximum exactly when the peak at $V_2O^{=/-}$ completely disappears. This may suggest that V_2O is involved in the creation of E(198 K). Another possibility is that the processes are unrelated, and that both are activated by some other event, such as the release

of H. However, there are no indications that V_2O reacts with H, on the contrary V_2O is concluded to dissociate in section 5.4.3.2.

The change in concentration of V_2O and E(198 K) are shown to be proportional in figure 5.23 for 325 – 360 °C with an average slope of 0.14 ± 0.03. The plotted concentrations are from the pre–annealing and until the $V_2O^{=/-}$ peak disappears. The growth of E(198 K) is calculated as

$$\text{Growth [E(198 K)]} = \text{[E(198 K)]} - \text{[E(198 K)]}_{t=0}$$

and the loss of V_2O is

$$\text{Loss } [V_2O] = [V_2O]_{t=0} - [V_2O]$$

calculated from $t = 0$, and until V_2O disappears below the detection limit and E(198 K) is at a maximum (occurs at the same time).

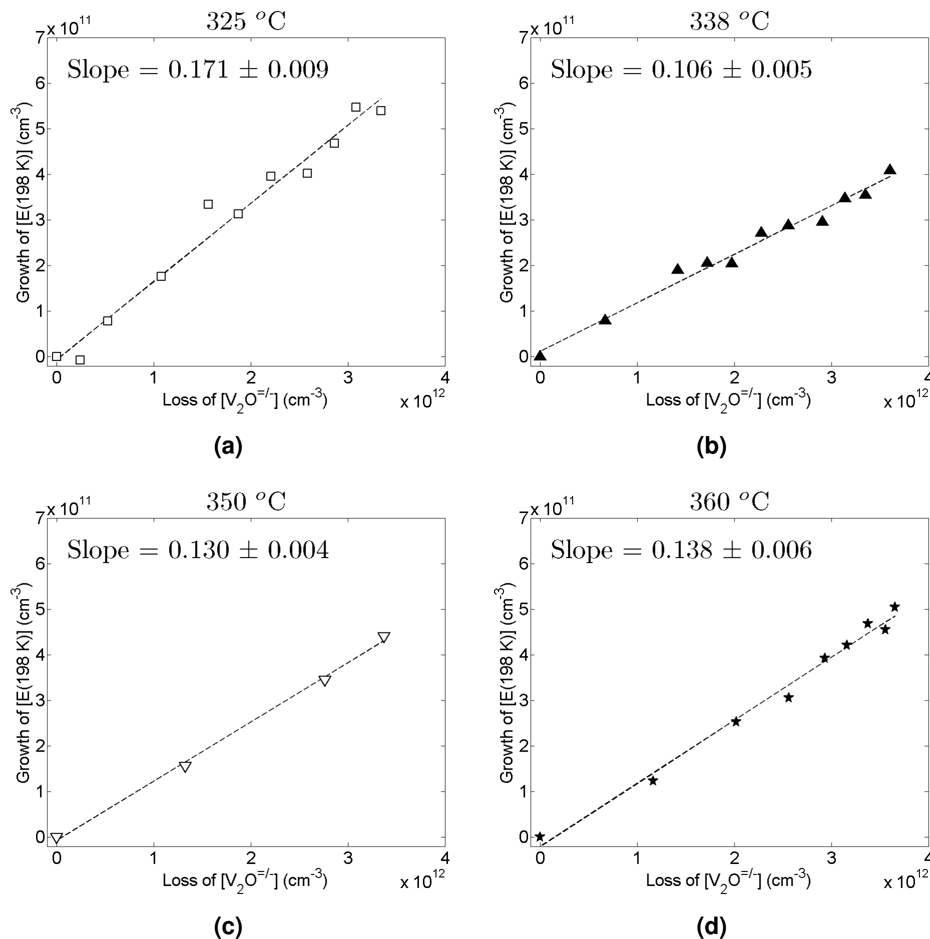

Figure 5.23: The growth of E(198 K) plotted as a function of the decay of V_2O. The data for V_2O is from the $V_2O^{=/-}$ peak. The average slope is 0.14 ± 0.03.

A possible explanation is that one of the released complexes from the dissociation of V_2O forms E(198 K) through a reaction with some other defect or impurity. V_2O is shown to

dissociate mainly by $V_2O \rightarrow VO + V$ in section 5.4.3.2, but a fraction may also dissociate as $V_2O \rightarrow V_2 + O_i$.

In the first case, E(198 K) could be formed in a reaction involving the released V from the dissociation of V_2O and also the dissociation of VO, as

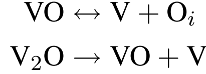

$$VO \leftrightarrow V + O_i$$
$$V_2O \rightarrow VO + V$$

where $\leftrightarrow$ means that VO may also reform after the dissociation. Reformation of V_2O is shown to be insignificant in the model in section 5.4.4. Furher, V may react with some defect Y to form E(198 K) in the reaction

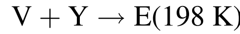

$$V + Y \rightarrow E(198\ K)$$

The fact that there is a small concentration of E(198 K) already at $t = 0$ after the pre–annealing, could be explained by a limited dissociation of V_2, V_2O or other vacancy–containing defects prior to the start of the annealing. Some restrictions can be put on the possible identity of Y. Y must have only one acceptor level and this must overlap with $V_2^{-/0}$ and $V_2O^{-/0}$. It may also have a higher concentration near the surface as shown in the depth profile in the following section, however this is not conclusive. H is a possible candidate since VH is claimed to overlap with $V_2^{-/0}$ [32], but no information was found on the thermal stability of VH. Other possible candidates for Y are the V_nO_2 complexes, where $n \geq 2$. However, VO_2 can most likely be excluded, since that would identify E(198 K) as V_2O_2 which is known to have both a single and a double acceptor level similar to V_2O, according to density functional calculations by Coutinho et al. in reference [14].

In the second case, E(198 K) could be formed in a reaction involving V_2 from the fraction of V_2O which dissociates through $V_2O \rightarrow V_2 + O_i$, so E(198 K) is generated by

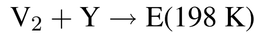

$$V_2 + Y \rightarrow E(198\ K)$$

Again, the small concentration of E(198 K) which is present already at $t = 0$ after the pre–annealing, could be explained by a limited reaction involving a fraction of V_2 which escapes the transformation into V_2O, or simply from dissocation of V_2O centers prior to the start of the annealing. If this is the case, then Y may be H, since V_2H is believed to have an acceptor level which overlaps with $V_2O^{-/0}$, according to Coutinho et al. in reference [15].

The two suggested scenarios for the generation of E(198 K) from released complexes during the dissociation of V_2O, may explain the linear relationship between the loss of V_2O and the growth of E(198 K), as well as the fact that the growth of [E(198 K)] ceases when V_2O disappears. The linear relationship in figure 5.22 requires either a large concentration of Y, or that either Y, Vor V_2 has a large diffusivity, which does not hold in the case of V_2. In the latter case the measured growth rate of E(198 K) should be equal to the dissociation rate of V_2O. Unfortunately, the uncertainty in the extracted E_a and c_0 are too large to determine if this is the case, but based on the mean values this seems unlikely. Thus, a

large concentration of Y relative to the released V or V_2 is the most likely explanation for the linearity of the logarithm of $[E(198\ K)]_{max} - [E(198\ K)]$.

DECAY

The decay of E(198 K) is first order as shown in figure 5.24. The extracted activation energy is

$$E_a = (2.65 \pm 0.34)\ \text{eV}$$

and the pre–exponential factor is

$$c_0 = (5 \times 10^{16}\ \text{s}^{-1}) \times \exp(\pm 6)$$

The linear fit in figure 5.24(a) is not very good for 325 and 338 °C, hence the large uncertainties in E_a and c_0. The value of c_0 may indicate that E(198 K) anneals by dissociation.

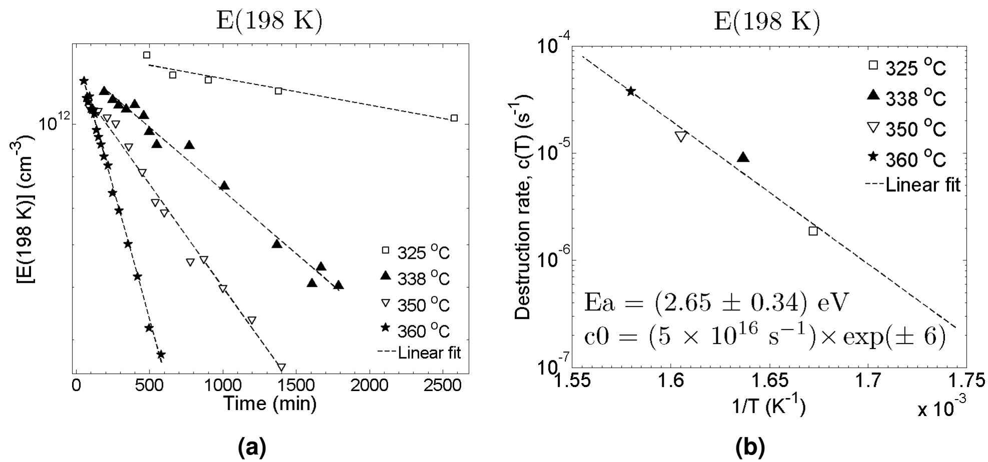

Figure 5.24: A semilogarithmic plot of [E(198 K)] vs. time for the decay of E(198 K), with a linear least squares fit **(a)**. The linear fit agrees reasonably well with the measurements at all four temperatures, indicating first order annealing. $\ln c(T)$ is plotted vs. $1/T$ to determine the activation energy of the reaction **(b)**.

The profile of E(198 K) can only be measured for the decay, because during the growth the E(198 K) peak is completely overshadowed by $V_2O^{-/0}$. The concentration depth profiles measured during the decay are displayed in figure 5.25. The distribution of E(198 K) at the maximum after annealing for 140 min at 338 °C has a decreasing tendency from the surface towards the bulk. This is similar to VOH, but not to the same extent. This may indicate that E(198 K) contains a defect or an impurity with a diffusion–like concentration profile, but this is not conclusive because of the relatively small difference between surface and bulk concentration as compared to VOH. However, during the decay of E(198 K) from 140 – 1790 min [E(198 K)] clearly decreases much faster at the surface than in the bulk at around 12 μm.

This is a strong indication that E(198 K) is not dissociating, but rather reacting with a species with a large concentration at the surface. Possible candidates for this species are H, C_i or even O_i. O_i is expected to have a limited mobility at temperatures above 300 °C, since

$$D_{Oi} = 0.17 \times \exp(-2.54/kT)\ \text{cm}^2\text{s}^{-1}$$

according to Åberg et al. in reference [1]. All of these defects have increasing concentrations towards the surface, as explained in section 5.2.1.

The fact that E(198 K) seems to be suppressed in hydrogen–lean samples, as indicated in section 5.3.2, tentatively supports that E(198 K) contains hydrogen, as is vaguely indicated by the depth profile.

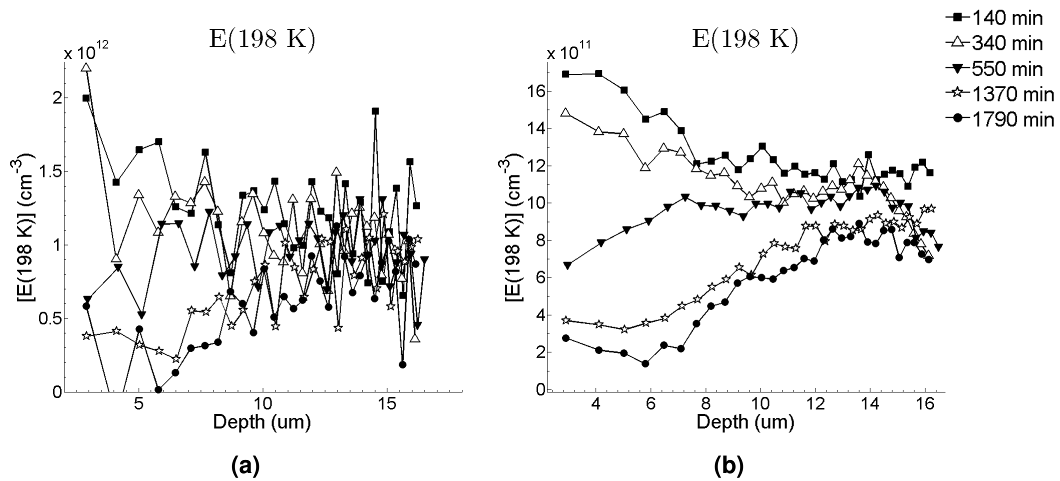

Figure 5.25: The depth profile of E(198 K) measured after isothermal annealing at 338 °C unsmoothed **(a)** and smoothed by a running average over 5 points **(b)**.

Chapter 6

Summary

6.1 Conclusions

The concentrations of oxygen and carbon in the n–type epitaxial layer is determined by SIMS measurements to $[\mathrm{O}_i] \leq 2 \times 10^{17}$ cm^{-3} and $[C] \leq 5 \times 10^{16}$ cm^{-3}, respectively.

The annealing processes of the previously known defects VO, V_2O and VOH and two unidentified levels, labeled E(170 K) with $E_c - E_t = 0.34 \pm 0.01$ and E(198 K) with $E_c - E_t = 0.46 \pm 0.02$, are studied by DLTS during isochronal and isothermal annealing at 325 – 360 °C. A fitting procedure is used to succesfully separate the partially overlapping levels of VOH and E(170 K), by comparing measurements to synthesized DLTS spectra from both lock–in and GS4 type weighting functions.

The isochronal measurements show that the annealing rate of VO and V_2O is higher in samples with the most hydrogen (the DOFZ samples in reference [25]) and lowest in samples with the least hydrogen (the MCz samples in reference [25]), with the annealing rate in the PI samples studied in this thesis somewhere between. This may be due to hydrogen assisted annealing of VO and V_2O. In addition, the E(170 K) defect appears most prominently in the EPI samples, which may indicate that it is suppressed in more oxygen–rich materials. The E(198 K) defect appears to be suppressed in hydrogen–lean samples.

The data from the pre–annealing procedure used to transform V_2 into V_2O shows that the transformation rate is slightly lower than in DOFZ with a slightly higher oxygen concentration, as found in reference [25]. This supports that the transformation rate increases with increasing oxygen concentration, as concluded in reference [2].

In the EPI samples studied in this work, it is concluded that VO anneals mainly by dissociation with $E_a = 2.37 \pm 0.05$ eV and 6×10^{14} s^{-1}, but a fraction disappears through the production of VOH (determined from the depth profile) and likely VO_2. V_2O is also concluded to mainly dissociate with $E_a = 1.95 \pm 0.22$ eV and 4×10^{12} s^{-1}. These results agree well with the results of Mikelsen et al. in [24].

The extracted growth rate of VOH is $(3 \times 10^{13}) \times \exp(-(2.12 \pm 0.20)/kT)$ s^{-1}, where the pre–exponential factor is of the same order of magnitude as expected from a dissociation process. Hence, it is argued that the observed growth rate is actually very close to

the dissociation rate of the postulated near–surface hydrogen source, HZ. H is released through HZ $\rightarrow$ H + Z, and H can very rapidly migrate to and react with VO to form VOH due to its very high diffusivity. VOH is concluded to disappear mainly through the formation of the inactive VOH_2 defect, based on the decrease of the depth profile of VOH near the surface. A small model adapted from reference [24] reproduces the results from the isothermal annealing for VO, V_2O and VOH very well.

The annealing rate of E(170 K) is $(4 \times 10^{13}) \times \exp(-(2.16 \pm 0.08)/kT)$ s^{-1}, which is essentially identical to the growth rate of VOH. The growth of VOH is also shown to be proportional to the loss of E(170 K), and the proportionality factor approaches unity at 360 °C. The suggested explanation is that HZ dissociates, H reacts with VO to form VOH and Z reacts with E(170 K) which consequently disappears with the same rate as HZ and the growth rate of VOH. This explanation requires that Z has a high diffusivity in silicon, which means that for example V, I_{Si} and C_i are potential candidates for the identity of Z.

The growth of E(198 K) is shown to be proportional to the loss of V_2O with an average ratio 0.14 ± 0.03. This is tentatively explained by a reaction between either V or V_2 from the dissociation of V_2O and some unidentified defect Y. The depth profile of E(198 K) is inconclusive about whether there is an increase towards the surface, but it clearly shows that the subsequent loss of E(198 K) occurs much more rapidly at the surface than in the bulk.

6.2 Suggestions for future work

The transformation rate for the reaction from V_2 to V_2O has only been measured over a relatively narrow interval of oxygen concentrations, about 10^{16} – $(5 - 10) \times 10^{17}$ cm^{-3}, as indicated in table 5.5. Measurements of this transformation rate should also be done for materials with lower (if possible) and higher oxygen concentrations to better determine the dependence on the oxygen content.

The model in section 5.4.4 reproduces the measured data very well. However, this model does not take non–uniform depth distributions into account, which may be quite important for the kinetics. Thus, the model should be expanded to also take into account the initial depth distribution of defects (from measurements or assumptions), particularly for highly mobile defects or highly non–uniform distributions such as H, HZ and VOH.

The measurements in this work was performed on EPI material which was only irradiated with one dose, 10^{14} cm^{-2}. Irradiations with other doses should be performed to determine if the kinetics suggested here holds also at higher and lower concentrations of VO, V_2O and VOH (with hydrogenation to increase the concentration of hydrogen). In particular, it would be highly interesting if more information could be extracted about the correlation between HZ, VOH and E(170 K). Measurements on samples with different impurity contents, in particular oxygen and carbon, might reveal information about the identity of E(170 K). Isothermal annealings at lower temperatures should be done to study the growth of E(170 K).

Also, if E(170 K) is measured with a method which can measure also electrically inactive defects, then perhaps HZ can also be found from the correlation with E(170 K).

Appendix A

Documentation of Matlab-scripts

A.1 Analysis of DLTS-spectra

The Matlab code below calculates the energy and sigma after the peak temperatures have been selected. Peak temperatures are stored in the matrix T before this code. The results of running the code are shown in figure A.1. “kb” is the Boltzmann constant, “h” is the Planck constant and “m_eff_e” is the effective mass for electrons in silicon.

The code below is run by another script. This script imports DLTS data from the datafiles, plots it and allows the user to pick the peak temperature from the plot by using the Matlab function “ginput”. The peak temperature is passed on to the code below.

```
% - Calculate energies and capture cross section.
% ------------------------------------------------
energies = zeros( length(T(:,1)), 1 );
sigma = zeros( length(T(:,1)), 1 );

sigma_pre   = 2*sqrt(3) * kb^2 * m_eff_e * (2*pi/h^2)^1.5;

% Loop through peaks.
figure_large;
for k = 1:length(T(:,1))
    x = 1./T(k,:);
    y = (er(win_start:win_stop)./T(k,:).^2);

    arrhenius_lsq(k,:) = polyfit( x, log(y), 1 );
    y_lsq = polyval( arrhenius_lsq(k,:), x );

    energies(k) = abs( arrhenius_lsq(k,1) ) * kb_eV;
    sigma(k) = exp(arrhenius_lsq(k,2)) / sigma_pre;
end
```

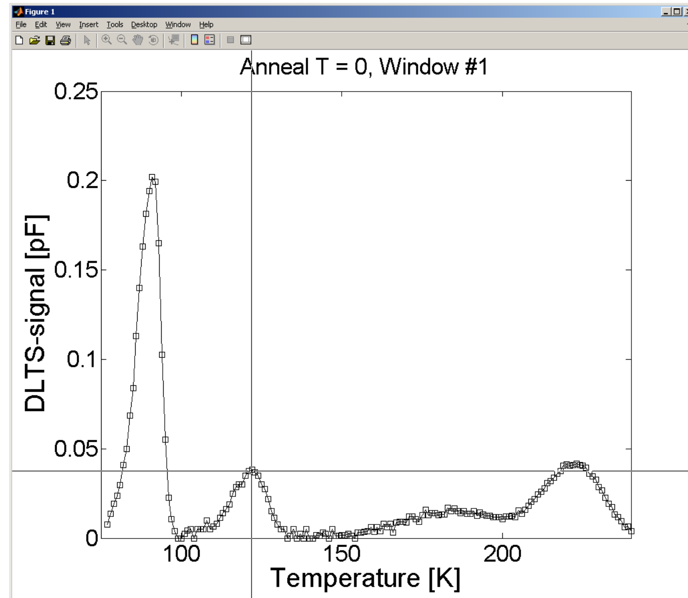

(a)

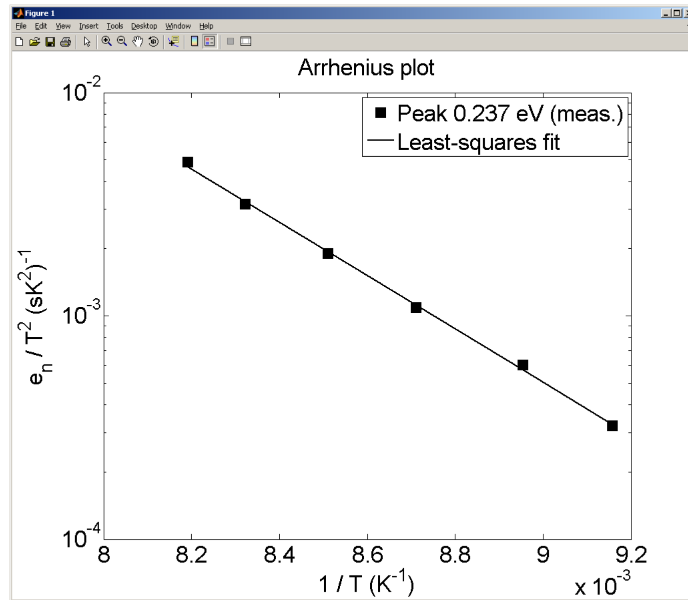

(b)

Figure A.1: Selecting peak temperature by using the mouse cursor crosshair. The amplitude is found by the Matlab script when the peak temperature is selected **(a)**. The Arrhenius plot which is generated after the peak temperature is selected for lock–in rate windows 1–6 **(b)**. This example is for the $V_2^{=/-}$ peak.

A.2 Fitting/synthesis of DLTS-spectra

The creation of a synthetic DLTS spectrum was done according to equation (4.19). Defects were given a concentration, σ_{na} and ΔH . Then the DLTS spectrum was calculated for each of them and these spectra were added to give the total spectrum.

A screenshot of the user interface of the program is shown in figure A.2 and a fitted lock–in DLTS spectrum as exported by the program is in figure A.3. Notice that the program labels peaks which are recognized, such as VOH and the L–center.

FEATURES

- Fitting of DLTS spectra in
  - Lock–in
  - GS4
- The fitted level parameters and the resulting spectrum can be exported to Matlab files for future use.
- Smoothing by a "simple running average" over a specified number of data points, can be useful for noisy data.
- A Matlab figure of the result can be created.

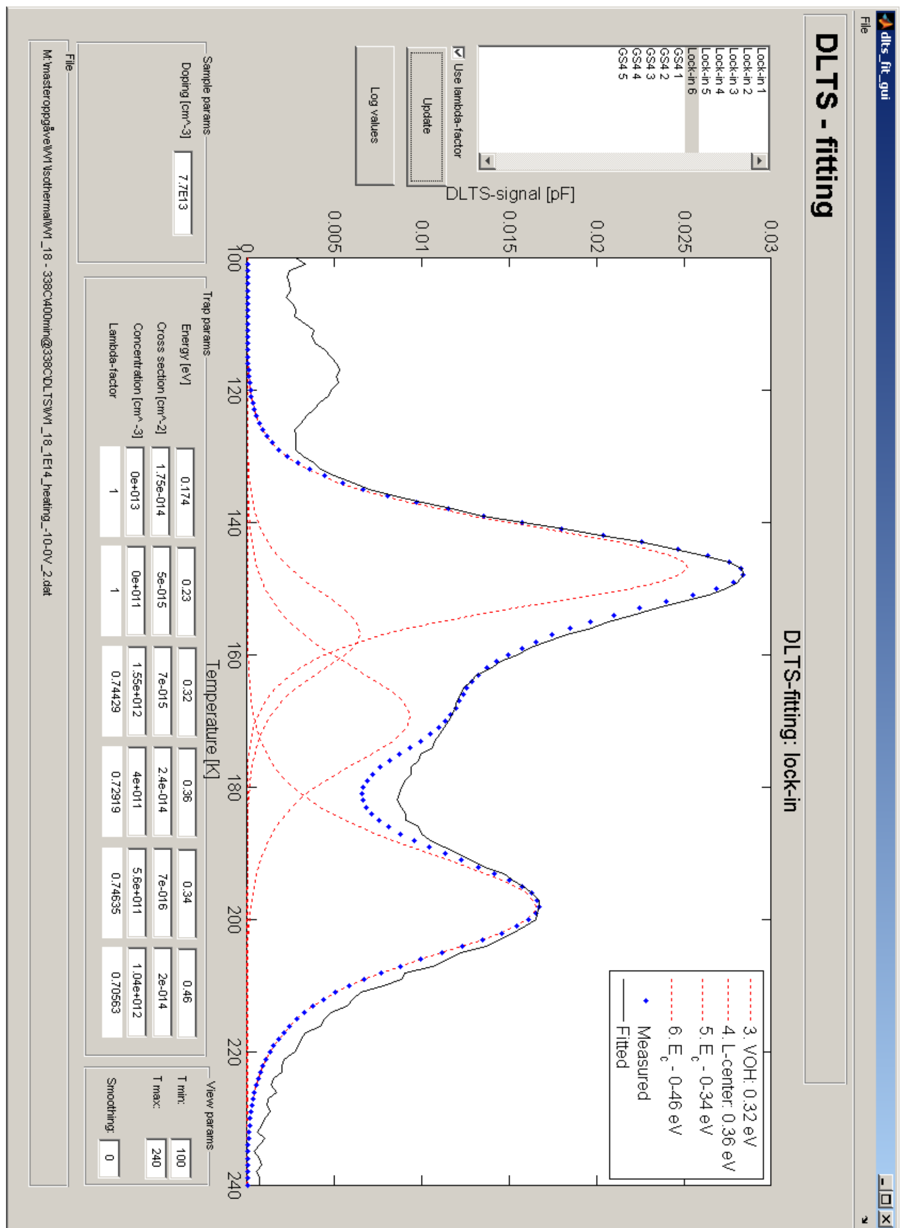

Figure A.2: A screenshot of the user interface of the DLTS fitting program in Matlab.

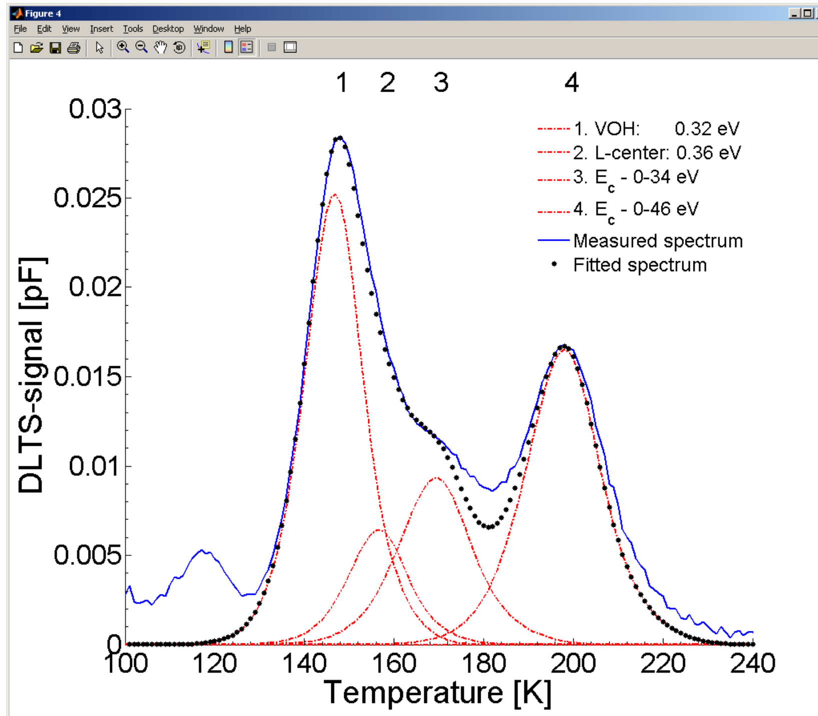

Figure A.3: A Matlab figure as exported by the fitting program.

A.3 Simulation of defect reactions

Matlab has a family of functions for solving sets of ordinary differential equations. "ode15s" was used in this thesis. The function is called as

```
1  % Solve diff.equations.
   [T, N] = ode15s(          @reactions_small_model, ...
3                            [0, end_time(j)]*60, ...
                             N_0*1E6 );
```

The first argument, "@reactions_small_model", is the handle name of the function containing the set of differential equations to be solved. The second argument, [0, end_time(j)]*60, is a vector of the start and end time for the solution. The simulations were perfomed with seconds as the time unit, hence the multiplication by 60 to convert the original limits from minutes to seconds. The last argument, N_0*1E6, is a vector with the initial concentrations of the defects, given in cm^{-3} and converted to m^{-3} to have everything in Si units.

The returned variables from "ode15s" is the modeled concentration, N, and the solution times, T. The set of differential equations is specified in a separate function, as shown in the source code below.

```
   function dN = reactions_small_model( t, N )
2
   % Load physical constants, e.g. kb, h, etc.
4  constants;
```

```
6  % Temperature.
   global temp_global;
8  T = temp_global;        % K

10 % Capture radius.
   R        = 5E-10;     % m
12 alpha    = 4*pi*R;    % m

14 % Diffusion constants.
   global D_VO;
16 global D_Oi;
   global D_V;
18 global D_H;

20 % Dissociation rates.
   global C_VO;
22 global C_V2O;
   global C_HX;
24 global C_VOH;

26 % Equations.
   % ----------------
28 % N(1): V2O
   % N(2): VO
30 % N(3): VO2
   % N(4): Oi
32 % N(5): V
   % N(6): VOH
34 % N(7): H
   % N(8): VOH2
36 % N(9): HX
   % N(10): X
38
   % Indices.
40 V2O      = 1;
   VO       = 2;
42 VO2      = 3;
   Oi       = 4;
44 V        = 5;
   VOH      = 6;
46 H        = 7;
   VOH2     = 8;
48 HX       = 9;
   X        = 10;
50
   % Minimal model.
52 % ------------------
   dN = zeros( X, 1 );
54
   dN(V2O)      =    - C_V2O * N(V2O);
56
   dN(VO)       =    C_V2O * N(V2O) - C_VO * N(VO) + ...
```

```
58                      alpha * ( - D_H * N(H) * N(VO) ...
                        - D_VO * N(VO) * N(Oi) + D_V * N(V) * N(Oi) );
60
   dN(V)        =       C_V2O * N(V2O) + C_VO * N(VO) - ...
62                      alpha * ( D_V * N(V) * N(Oi) );

64 dN(VOH)      =       - C_VOH * N(VOH) + alpha * ( D_H * N(H) * N(VO) ...
                        - D_H * N(H) * N(VOH) );
66
   dN(H)        =       C_HX * N(HX) - alpha * (D_H * N(H) * N(VO) + ...
68                      D_H * N(H) * N(X) + D_H * N(H) * N(VOH) );

70 dN(VOH2)     =       alpha * D_H * N(H) * N(VOH);

72 dN(HX)       =       - C_HX * N(HX) + alpha * D_H * N(H) * N(X);

74 dN(X)        =       C_HX * N(HX) - alpha * D_H * N(H) * N(X);
```

Appendix B

Integration of the Poisson equation

This section follows the derivation of the voltage across a depletion region with electrically active defects as presented in Blood & Orton [6].

The space charge density when there is only one donor–like level participating in capture and emission processes is

$$\rho(x,t) = q\left[N^{+}_{eff} + (N_t - n_t(t))\right] \qquad \begin{array}{l} n_t(t=0) = N_t \\ n_t(t=\infty) = 0 \end{array}$$

N^{+}_{eff} takes into account the effective doping $N_d - N_a$ and any other levels that are not emitting electrons, but which could be in a non–neutral charge state.

A time–dependent space charge density, $\rho(x,t)$, will result in a time–dependency of the electric field, $\varepsilon(x,t)$, and of the total potential over the junction, $V = V(t)$. In solving the Poisson equation for the potential as a function of position one must then assume a time–dependency also, $\psi = \psi(x,t)$, so

$$\frac{\partial^2\psi}{\partial x^2} = -\frac{\rho(x,t)}{\epsilon_{Si}\epsilon_0}$$

This can be integrated, renaming the spatial variable to z and keeping t constant, as

$$\begin{aligned} \int_{-\infty}^{y}\left(\frac{\partial^2\psi}{\partial z^2}\right)_t dz &= \left(\frac{\partial\psi(z=y,t)}{\partial z}\right) - \left(\frac{\partial\psi(z=-\infty,t)}{\partial z}\right) \\ &= -\frac{1}{\epsilon_{Si}\epsilon_0}\int_{-\infty}^{y}\rho(z,t)dz \end{aligned} \tag{B.1}$$

The last term in the middle expression vanishes because $\varepsilon(z,t) = -\frac{\partial\psi(z,t)}{\partial z} = 0$ outside the depletion region.

Integrating again over $z = -\infty$ to $z = x$ yields $\psi(x,t)$ as

$$\begin{aligned} \int_{-\infty}^{x}\left(\frac{\partial\psi(z=y,t)}{\partial z}\right)_t dy &= \psi(x,t) - \psi(-\infty,t) \\ &= -\frac{1}{\epsilon_{Si}\epsilon_0}\int_{-\infty}^{x}\left[\int_{-\infty}^{y}\rho(z,t)dz\right]dz \end{aligned} \tag{B.2}$$

Through integration by parts of the right hand side,

$$\int uv'dy = uv - \int u'vdy$$

choosing $u(y) = \int_{-\infty}^{y} \rho(z,t)dz$ and $v(y) = y$ this yields after some manipulation

$$\psi(x,t) - \psi(-\infty,t) = -\frac{1}{\epsilon_{Si}\epsilon_0}\left[y\int_{-\infty}^{y}\rho(z,t)dz\right]_{y=-\infty}^{y=x} - \int_{-\infty}^{x} z\rho(z,t)dz \quad \text{(B.3)}$$

By integrating to $x = \infty$ the first term disappears because $\rho(x,t) = 0$ for $x < -x_p$ and $x > x_n$. Also

$$\int_{-x_p}^{x_n} \rho(x,t)dz = 0$$

because of charge equality. The total potential over the junction is

$$V(t) = \psi(\infty,t) - \psi(-\infty,t) = \frac{1}{\epsilon_{Si}\epsilon_0}\int_{-x_p}^{x_n} z\rho(z,t)dz \quad \text{(B.4)}$$

The integration limits can be chosen as $\int_0^{x_d}$ for a p^+-n^-junction since $x_n \gg x_p$.

Uniform distributions of N_{eff}^+, N_t and n_t are now assumed within each of the three different regions defined in table 4.2. This means that the contributions from these to the space charge density in each region will be

$$N^+(x) = \begin{cases} N^+ & \text{for} \quad 0 < x < x_d(t) \\ 0 & \text{else} \end{cases}$$

$$N_t(x) = \begin{cases} N_t & \text{for} \quad 0 < x < x_d(t) - \lambda \\ 0 & \text{else} \end{cases}$$

$$n_t(t,x) = \begin{cases} n_t(t) & \text{for} \quad x_p - \lambda < x < x_d(t) - \lambda \\ 0 & \text{else} \end{cases}$$

Therefore the total potential can be written

$$\begin{aligned} V(t) &= \frac{q}{\epsilon_{Si}\epsilon_0}\int_0^{x_d(t)}\left[N_{eff}^+ + (N_t - n_t(t))\right]xdx \\ &= \frac{q}{\epsilon_{Si}\epsilon_0}\left[N^+\int_0^{x_d(t)} xdx + N_t\int_0^{x_d(t)-\lambda} xdx - n_t(t)\int_{x_p-\lambda}^{x_d(t)-\lambda} xdx\right] \\ &= \frac{q}{2\epsilon_{Si}\epsilon_0}\left\{N^+x_d^2(t) + N_t(x_d(t)-\lambda)^2 - n_t(t)\left[(x_d(t)-\lambda)^2 - (x_p-\lambda)^2\right]\right\} \end{aligned} \quad \text{(B.5)}$$

As the traps emit their electrons under reverse bias the voltage over the junction will try to change to accomodate the increase in space charge density. However, in a constant–voltage DLTS system the instrumentation will keep the reverse bias constant during the emission. Differentiating the above expression for $V(t)$ and equating to zero yields

$$\left[N^+x_d + (N_t - n_t)(x_d - \lambda)\right]\frac{dx_d}{dt} = \frac{1}{2}\left[(x_d(t)-\lambda)^2 - (x_p(t)-\lambda)^2\right]\frac{dn_t}{dt} \quad \text{(B.6)}$$

In these calculations the assumption has been made that λ is only a function of temperature, it does not vary with voltage. In the so–called dilute limit the following is valid

$$N^+ \approx N_d \gg Na, N_t, n_t$$

Then the left hand side in the above equation greatly simplifies to

$$\begin{aligned} N_d x_d \frac{dx_d}{dt} &= \frac{1}{2}\left[(x_d(t)-\lambda)^2 - (x_p-\lambda)^2\right]\frac{dn_t}{dt} \\ \frac{dx_d/dt}{x_d} &= -\frac{dC_{rb}/dt}{C_{rb}} = \frac{1}{2}\frac{\left[(x_d(t)-\lambda)^2-(x_p-\lambda)^2\right]}{x_d^2}\frac{1}{N_d}\frac{dn_t}{dt} \end{aligned} \tag{B.7}$$

$C_{rb}(t) = \epsilon_{Si}\epsilon_0 A/x_d(t)$ is used and the change in reverse bias capacitance during the emission process is assumed to be small so C_{rb} is approximately constant. Integrating from $t = \infty$ to t and using equation (3.29) and that $n_t(\infty) = 0$ yields

$$\Delta C(T,t) = -\Delta C_0 e^{-e_n(T)t} \tag{B.8}$$

The maximum amplitude of the transient is

$$\Delta C_0 = \frac{1}{2}\frac{(x_d(t)-\lambda)^2-(x_p-\lambda)^2}{x_d^2}\frac{N_t}{N_d}C_{rb} \tag{B.9}$$

Equation (B.8) is a good approximation when the depletion approximation can be assumed, when the trap concentration is within the dilute limit and for uniform N_d and N_t. It applies for constant reverse bias

$$\frac{dV_{rb}}{dt} = 0$$

If $x_d \gg \lambda, x_p$ then equation (4.12) further simplifies to

$$\Delta C_0 = \frac{N_t}{2N_d}C_{rb}$$

Otherwise the factor

$$\alpha \equiv \frac{(x_d-\lambda)^2-(x_p-\lambda)^2}{x_d^2}$$

can be expressed in terms of the reverse and pulse bias capacitances as

$$\alpha(T) = \frac{(x_d-\lambda(T))^2-(x_p-\lambda(T))^2}{x_d^2} = 1-\left(\frac{C_{rb}}{C_p}\right)^2 - \frac{2C_{rb}}{\epsilon_{Si}\epsilon_0 A}\left(1-\frac{C_{rb}}{C_p}\right)\lambda(T) \tag{B.10}$$

Appendix C

Properties of some electrically active defects in electron irradiated Si

Assignment	$E_c - E_t$ (eV)	$\sigma_{n,p}$(cm^2)	T$^\dagger_{in}$ (°C)	T$^\dagger_{out}$ (°C)	E$_{diss}$ (eV)	E$_{mig}$ (eV)	Reference
$VO^{-/0}$	0.18	–	< RT	275–350	2.51	1.8	[12, 33, 41]
$V_2^{-/0}$	0.43	4×10^{-15}	< RT	250	1.6	1.3	[10, 30, 31, 40]
$V_2^{=/-}$	0.23	2.5×10^{-15}	< RT	250	1.6	1.3	[10, 30, 31, 40]
$V_2O^{-/0}$	0.47	2×10^{-14}	220	250	2.02	–	[24, 30]
$V_2O^{=/-}$	0.23	4.7×10^{-15}	220	325	2.02	–	[24, 30]
$VOH^{-/0}$	0.32	3×10^{-15}	275	325	–	–	[23, 31, 33, 39]
$C_i^{-/0}$	0.11	6×10^{-15}	–	30–70	–	0.74	[29]
*$C_iC_s^{-/0}$ A	OVERLAPS W/ $VO^{-/0}$		–	∼RT	–	–	[29]
*$C_iC_s^{-/0}$ B	0.11	–	–	∼RT	–	–	[29]
$VP^{-/0}$	OVERLAPS W/ $V_2^{-/0}$		–	150	–	0.95	[29, 44]
$VH^{-/0}$	0.443	–	–	–	–	–	[22, 32]
$V_2H^{-/0}$	0.43	–	–	–	–	–	[22, 32, 39]
$V_2H_2^{-/0}$	0.2	–	–	–	–	–	[15, 31]
V_2OH	0.44	7×10^{-15}	–	–	–	–	[24, 25]
$V_2O_2^{-/0}$	OVERLAPS W/ $V_2^{-/0}$		∼300	∼400	–	–	[14, 21]

Table C.1: A list of some acceptor levels and their properties in irradiated Si with references. *Has two different physical configurations. The so–called A configuration completely overlaps with VO, but starts to anneal out already at room temperature. †Depends on the concentration of impurities like oxygen and hydrogen, i.e. whether or not the annealing is impurity assisted. The stated electrical properties of V_2H, V_2H_2 and V_2OH should be considered tentative as suggested in the references.

Structure	$E_t - E_v$ (eV)	$\sigma_{n,p}$(cm^2)	T$_{in}$ (°C)	T$_{out}$ (°C)	E$_{diss}$ (eV)	E$_{mig}$ (eV)	Reference
$^{\ddagger}V_2^{0/+}$	0.19	$\sim 10^{-16}$	< RT	250	1.6	1.3	[10, 42]
$^{\ddagger}V_2O^{0/+}$	0.24	$\sim 10^{-14}$	220	325	2.02	–	[42]
$VOH^{0/+}$	0.28	–	275	325	1.6	1.3	[15]

Table C.2: A list of some donor levels and their properties in irradiated Si with references. ‡Properties which are not considered to be specific to the charge state of a defect, such as annealing temperatures and reaction energies, have been filled in from table C.1 if not mentioned specifically in the litterature for the donor level.

References

[1] D. Åberg, B. G. Svensson, T. Hallberg, and J. L. Lindström. Kinetic study of oxygen dimer and thermal donor formation in silicon. *Phys. Rev. B*, 58(19):12944–12951, Nov 1998.

[2] G. Alfieri, E. V. Monakhov, B. S. Avset, and B. G. Svensson. Evidence for identification of the divacancy–oxygen center in si. *Physical Review B*, 68(233202), 2003.

[3] Neil W. Ashcroft and N. David Mermin. *Solid State Physics*, page 569. Thomson Learning, Inc., 1976.

[4] J. H. Bleka, E. V. Monakhov, B. S. Avset, and B. G. Svensson. Dlts study of room–temperature defect annealing in high–purity n–type Si. *ECS Transactions*, 3(4):387–393, 2006.

[5] P. Blood and J.W. Orton. *The Electrical Characterization of Semiconductors: Majority Carriers and Electron States*, chapter 7, pages 336–398. Volume 14 of *Techniques of Physics* [6], 1991.

[6] P. Blood and J.W. Orton. *The Electrical Characterization of Semiconductors: Majority Carriers and Electron States*, volume 14 of *Techniques of Physics*. Philips Research Laboratories, 1991.

[7] J. Bourgoin and M. Lannoo. *Point Defects in Semiconductors II*. Springer-Verlag, 1983.

[8] Stephen A. Campbell. *The Science and Engineering of Microelectronic Fabrication*. Oxford University Press, 2nd edition, 2001.

[9] CERN/LHCC 2000–009. *3RD RD48 STATUS REPORT*, December 1999.

[10] J. W. Corbett and G. D. Watkins. Silicon divacancy and its direct production by electron irradiation. *Physical Review Letters*, 7(8):A543–A555, October 1961.

[11] J. W. Corbett and G. D. Watkins. Production of divacancies and vacancies by electron irradiation of silicon. *Physical Review*, 138(2A):A555–A560, April 1965.

[12] J. W. Corbett, G. D. Watkins, R. M. Chrenko, and R. S. McDonald. Defects in irradiated silicon: II. infrared absorption of the Si–A center. *Physical Review*, 121(4):1015–1022, February 1961.

[13] James W. Corbett. Solid state physics – advances in research and applications. In Frederick Seitz and David Turnbull, editors, *Electron radiation damage in semiconductors and metals*, chapter 7. Academic Press, 1966.

[14] J. Coutinho, R. Jones, S. Öberg, and P. R. Briddon. The formation, dissociation and electrical activity of divacancy–oxygen complexes in Si. *Physica B*, 340–342.

[15] J. Coutinho, V. J. B. Torres, R. Jones, S. Öberg, and P. R. Briddon. Electronic structure of divacancy–hydrogen complexes in silicon. *Journal of physics: Condensed Matter*, 15(39):S2809–S2814, 2003.

[16] G. Dearnaley, J. H. Freeman, R. S. Nelson, and J. Stephen. *Ion Implantation*, volume 8 of *Defects in Crystalline Solids*. North-Holland Publishing Company, 1973.

[17] J. D. Holbech, B. Bech Nielsen, R. Jones, P. Sitch, and S. Öberg. H_2^* defect in crystalline silicon. *Physics Review B*, 71(6):875–878, Aug 1993.

[18] Charles Kittel. *Introduction to solid state physics*. John Wiley & Sons, Inc., 8th edition, 2005.

[19] G. Kramberger, D. Contarato, E. Fretwurst, F. Hönniger, G. Lindström, I. Pintilie, R. Röder, A. Schramm, and J. Stahl. Superior radiation tolerance of thin epitaxial silicon detectors. *Nuclear Instruments and Methods in Physics Research A*, 515(3):665–670, December 2003.

[20] Sorina Lazanu and Ionel Lazanu. Modelling spatial distribution of defects and estimation of electrical degradation of silicon detectors in radiation fields at high luminosity, 2006.

[21] Young-Hoon Lee and James W. Corbett. EPR studies of defects in electron–irradiated silicon: A triplet state of vacancy–oxygen complexes. *Phys. Rev. B*, 13(6):2653–2666, Mar 1976.

[22] P. Lévêque, A. Hallén, B. G. Svensson, J. Wong-Leung, C. Jagadish, and V. Privitera. Indetification of hydrogen–related defects in proton implanted float–zone silicon. *The European Physical Journal Applied Physics*, 23:5–9, 2002.

[23] P. Lévêque, P. Pellegrino, A. Hallén, B. G. Svensson, and V. Privitera. Hydrogen–related defect centers in float–zone and epitaxial n–type proton implanted silicon. *Nuclear Instruments and Methods in Physics Research B*, 174:297–303, 2001.

[24] M. Mikelsen, J. H. Bleka, J. S. Christensen, E. V. Monakhov, and B. G. Svensson. Annealing of the divacancy–oxygen and vacancy–oxygen complexes in silicon. *Physical Review B*, 75(155202), 2007.

[25] M. Mikelsen, E. V. Monakhov, G. Alfieri, B. S. Avset, J. Härkonen, and B. G. Svensson. Annealing of defects in irradiated silicon detector materials with high oxygen content. *Journal of physics: Condensed Matter*, 17:S2247–S2253, 2005.

[26] M. Mikelsen, E. V. Monakhov, G. Alfieri, B. S. Avset, and B. G. Svensson. Kinetics of divacancy annealing and divacancy–oxygen formation in oxygen–enriched high–purity silicon. *Physical Review B*, 72(195207), 2005.

[27] M. Mikelsen, E. V. Monakhov, B. S. Avset, and B. G. Svensson. On the formation of the L–centre in silicon during heat treatment in the temperature range 205–285 °C. *Physica Scripta*, T127:1–4, 2006.

[28] Mads Mikelsen. *Thermal evolution of irradiation–induced defects in Silicon and Silicon Carbide*. PhD thesis, University of Oslo, 2007.

[29] Michael Moll. *Radiation Damage in Silicon Particle Detectors*. PhD thesis, University of Hamburg, 1999.

[30] E. V. Monakhov, B. S. Avset, A. Hallén, and B. G. Svensson. Formation of a double acceptor center during divacancy annealing in low–doped high-purity oxygenated Si. *Physical Review B*, 65(233207), June 2002.

[31] E. V. Monakhov, A. Ulyashin, G. Alfieri, A. Yu. Kuznetsov, B. S. Avset, and B. G. Svensson. Divacancy annealing in Si: Influence of hydrogen. *Physical Review B*, 69(153202), 2004.

[32] K. Bonde Nielsen, L. Dobaczewski, K. Goscinski, R. Bendesen, Ole Andersen, and B. Bech Nielsen. Deep levels of vacancy–hydrogen centers in silicon studied by laplace DLTS. *Physica B*, 273–274:167–170, 1999.

[33] P. Pellegrino, P. Lévêque, J. Lalita, A. Hallén, C. Jagadish, and B. G. Svensson. Annealing kinetics of vacancy–related defects in low–dose mev self–ion–implanted n–type silicon. *Physical Review B*, 64(195211), 2001.

[34] M. Pesola, J. von Boehm, T. Mattila, and R. M. Nieminen. Computational study of interstitial oxygen and vacancy–oxygen complexes in silicon. *Phys. Rev. B*, 60(16):11449–11463, Oct 1999.

[35] I. Pintilie, E. Fretwurst, G. Lindström, and J. Stahl. Close to midgap trapping level in ^{60}Co gamma irradiated silicon detectors. *Applied physics letters*, 81(1):165–167, May 2002.

[36] I. Pintilie, E. Fretwurst, G. Lindström, and J. Stahl. Second–order generation of point defects in gamma–irradiated float–zone silicon, an explanation for "type inversion". *Applied physics letters*, 82(13):2169–2171, March 2003.

[37] Stephen D. Senturia. *Microsystem Design*. Springer Science+Business Media Inc., 2000.

[38] Ben G. Streetman and Sanjay Banerjee. *Solid State Electronic Devices*. Prentice Hall International, Inc., 5th edition, 2000.

[39] B. G. Svensson, A. Hallén, and B. U. R. Sundqvist. Hydrogen–related electron traps in proton-bombarded float zone Si. volume B4, pages 285–289, October 1989.

[40] B. G. Svensson, K. Johnsson, DX. Xu, J. H. Svensson, and J. L. Lindström. Annealing of divacancy–related infrared absorption bands in boron–doped silicon. *Radiation Effects and Defects in Solids*, 111:439–448, December 1989.

[41] B. G. Svensson and J. L. Lindström. Kinetic study of the 830– and 889–cm^{-1} infrared bands during annealing of irradiated silicon. *Physical Review B*, 34(12):8709–8717, December 1986.

[42] M. A. Trauwaert, J. Vanhellemont, H. E. Maes, A. M. van Bavel, G. Langouche, and P. Clauws. Low–temperature anneal of the divacancy in p–type silicon: A transformation from V_2 to V_xO_y complexes? *Journal of Applied Physics*, 66(3056), 1995.

[43] T. R. Waite. Theoretical treatment of the kinetics of diffusion–limited reactions. *Physical Review*, 107(2):463–470, July 1957.

[44] G. D. Watkins and J. W. Corbett. Defects in irradiated silicon: Electron spin resonance and electron–nuclear double resonance of the Si–E center. *Physical Review*, 134(5A):A1359–1377, June 1964.